**Distribution Agreement**

In presenting this thesis or dissertation as a partial fulfillment of the requirements for an advanced degree from Emory University, I hereby grant to Emory University and its agents the non-exclusive license to archive, make accessible, and display my thesis or dissertation in whole or in part in all forms of media, now or hereafter known, including display on the world wide web. I understand that I may select some access restrictions as part of the online submission of this thesis or dissertation. I retain all ownership rights to the copyright of the thesis or dissertation. I also retain the right to use in future works (such as articles or books) all or part of this thesis or dissertation.

_____ _____

Boyi Yang Date

Numerical Modeling of Blood Flow Problems in Coronary Arteries:
Patient-specific Processing, from Stented Geometries to Fluid Dynamics

By

Boyi Yang
Doctor of Philosophy

Mathematics and Computer Science

_____
Alessandro Veneziani, Ph.D.
Advisor

_____
James Nagy, Ph.D.
Committee Member

_____
James Lu, Ph.D.
Committee Member

Accepted:

_____
Lisa A. Tedesco, Ph.D.
Deans of the James T. Laney School of Graduate Studies

_____
Date

# Numerical Modeling of Blood Flow Problems in Coronary Arteries: Patient-specific Processing, from Stented Geometries to Fluid Dynamics

By

Boyi Yang
M.S., Emory University, 2013
B.S., University of Texas at Austin, 2010
B.A., University of Texas at Austin, 2010

Advisor: Alessandro Veneziani

An abstract of
A dissertation submitted to the Faculty of the
James T. Laney School of Graduate Studies of Emory University
in partial fulfillment of the requirement for the degree of
Doctor of Philosophy
in Mathematics and Computer Science
2015

## Abstract

Numerical Modeling of Blood Flow Problems in Coronary Arteries:
Patient-specific Processing, from Stented Geometries to Fluid Dynamics
By Boyi Yang

Coronary stents expand the vessel to alleviate blockage, and they have been used for decades to save lives from coronary heart disease. Technological development has driven the evolution of stenting from bare or drug-coated metallic stents to the newly invented bioresorbable vascular stent (BVS). Rather than leaving a permanent metallic structure in the vessel, a BVS can dissolve in the body after opening the blocked artery, restoring the diseased coronary artery to its natural state. The BVS compensates for its decreased radial strength by having thicker struts that could cause disturbed blood flow, resulting in delayed healing and other devastating complications. Computational fluid dynamics (CFD) simulations had been used to analyze the potential risk of the BVS, but those simulations were conducted on either arbitrary geometry or partially patient-specific geometry with overly smoothed or virtually deployed stents [1]. In this thesis, we present a novel methodology to reconstruct true patient-specific CFD simulations: the geometry of a deployed stent inside a living patient is reconstructed from optical coherence tomography (OCT) images; the shape and the curvature of the stented vessel are obtained from angiography; and a real pulsatile flow rate profile can also be prescribed as inflow condition, when it is available. With patient-specific geometry, the CFD results reflect the true hemodynamics after stent deployment and describe the wall shear stress (WSS) and other quantities. We also aim to make the reconstruction and simulation process automatic, so that a large number of patients can be processed in a short time in order to draw statistically convincing conclusions. In fact, the entire process of the computational patient-specific analysis is expected to become a routine in clinical trials and activities (Computer Aided Clinical Trials, CACT). This has created significant challenges in many components of the methodological approach, ranging from image analysis, image processing, computational geometry to fluid dynamics. Our work witnesses the different challenges of this multi-component procedure. We hope the patient-specific reconstruction and simulation study can further the understanding of the BVS, improve its design, and ultimately expedite the tedious validation process so that it can soon become a soldier for us in the battle against coronary heart disease.

# Numerical Modeling of Blood Flow Problems in Coronary Arteries: Patient-specific Processing, from Stented Geometries to Fluid Dynamics

By

Boyi Yang
MS, Emory University 2013
BS, University of Texas at Austin 2010
BA, University of Texas at Austin 2010

Advisor: Alessandro Veneziani

A dissertation submitted to the Faculty of the
James T. Laney School of Graduate Studies of Emory University
in partial fulfillment of the requirement for the degree of
Doctor of Philosophy
in Mathematics and Computer Science
2015

**Acknowledgments**

First and foremost, I express my deepest gratitude to my advisor, Professor **Alessandro Veneziani**. He truly cares about me and his other students. I could not have asked for a better PhD advisor.

I also would like to thank the other members of my dissertation committee, Prof. James Nagy and Prof. Lu, for their guidance, encouragement and support. In addition, I express my deep gratitude to Dr. Gaetano Esposito, Dr. Marina Piccinelli, and Dr. Tiziano Passerini. Dr. Esposito made significant contributions to the improvement of the stent reconstitution program, Dr. Piccinelli made the vessel lumen reconstruction possible, and Dr. Passerini taught me the basics of how to execute a simulation on LifeV. All three have given me so much guidance that I cannot thank them enough.

My sincere appreciation goes to Dr. Habib Samady, who brought together a diverse group of physicians, engineers and mathematicians to study coronary stents. He believed in my ability and provided continuous support. I also thank Dr. Bill Gogas. During our three-year collaboration in researching bioresorbable stents, I learned much from him about interventional cardiology and we forged a good friendship.

I had the pleasure of co-advising three undergraduate honors students, Tianli Han, Shanon Buckley, and Ye Yuan. I appreciate their contributions to our research and I especially thank Tianli for his work in automatic stent strut detection.

I deeply appreciate the education and financial support I received from Emory Department of Mathematics and Computer Science, and I give special thanks to three professors: Prof. Raman Parimala, Prof. Michele Benzi, and Prof. Shanshuang Yang. They taught me the foundation of graduate-level mathematics and they supported me throughout my PhD study. I would also like to sincerely thank Terry Ingram, my degree coordinator, and Edgar Leon, the server and network manager. Terry and Edgar work diligently helping graduate students like me on a regular basis so that we can focus on our studies and research.

I thank all my family and friends. My thanks also go to my good friends Huanhuan Yang and her husband Zhengyao Wu. We have worked side by side through graduate school and have built a life-lasting friendship. I thank Dr. Francisco Vidal, who was my host father when I first came to the United

States as a high school exchange student. I would not be where I am today without him.

Last but not least, I would like to thank my parents, Peilu Yang and Qun Gu. I owe my parents too much. I am so lucky to be their son.

*To Qun and Peilu*

# Contents

# List of Figures

# Chapter 1

# Introduction

Heart disease is the number one cause of death in the United States, killing nearly 611,015 people in 2013, which is 4 times higher than the number of deaths caused by all types of accidents (unintentional injuries) combined [13]. Coronary heart disease is the most common type of heart disease and claims 380,000 lives annually. Coronary stents are effective medical devices in treating coronary heart disease and often the only way to save patients' lives. After deployment, a stent expands the plaque to the vessel wall and reopens the blocked artery. Epidemiology indicates that the need for coronary stents will undoubtedly increase [14], but holding the artery open is no longer the bar that is set for stenting. With the objective to create methods and devices that will restore the vessel function to as normal as possible, biomedical technology has driven the evolution of the stent system from bare-metal stents, to drug-eluting stents, and, more recently, to bioresorbable stents. Nonetheless, there is still considerable risk of stent failure. For instance, the newly invented bioresorbable stents pose higher risk of restenosis, the recurrence of abnormal narrowing of an artery after stent deployment, than occurs with bare-metal stents, and they are not yet approved by the US Food and Drug Administration despite their arguably innovative features. Mathematics and engineering play critical roles for the advancement of stenting technology. To gain true insight into the stent environment, the structure, hemodynamics, and biomechanics of the stents in real patients' arteries should be simulated, and stenting failures should be quantitatively analyzed. Reliable quantitative analyses need to be performed in real patients' morphologies because such morphologies have a major impact on the hemodynamics and eventually on the final outcome of the therapy. Therefore, we need accurate methods of

image processing and geometry reconstruction to feed the CFD simulations. In this thesis, we presented our contributions to the advancement of stenting technology: a novel methodology that reconstructs the deployed stent inside a living patient and subsequently simulates the blood flow in order to obtain critical data such as wall shear stress (WSS), which has a strong relationship with plaque progression. Current complications involving stenting are not close to satisfactory. We want a stent in a patient artery to work as dependably as a toaster does in a kitchen. The goal can be reached only through interdisciplinary studies, such as the one we conducted, which incorporate mathematics, computer science, and bioengineering into the clinical research in coronary stenting.

## 1.1 Coronary heart disease

Coronary heart disease threaten people's health. The World Health Organization estimated that 7.4 million people died from this disease globally in 2012 [15]. To put this number in perspective, that is 16 times Atlanta's entire population in the same year [16].

Coronary heart disease is caused by atherosclerosis in the coronary arteries. Atherosclerosis refers to the buildup of a waxy substance called plaque on the artery walls (see Figure 1.1). The plaque narrows the coronary artery; the buildup process occurs over many years. The plaque can also harden or rupture. When plaque ruptures, blood clots can form on its surface, leading to thrombosis, a condition in which large blood clots mostly or completely block blood flow through a coronary artery [2].

A life style with healthy diet and abundant exercise certainly reduces the rate of coronary heart disease. People's awareness of coronary heart disease is on the rise. More efforts have been made to prevent this disease. But does that mean that we will see a decline in the use of coronary stents in the near future and thus we can slow down our research on stenting technology? The answer is no. While coronary heart disease is usually diagnosed in older patients, the condition that leads to the disease, atherosclerosis, starts as early as the teenage years and is almost inevitable. Even if people in their 50s were to obey every instruction given by their cardiologists and dietitians, they would already have had 30 years of plaque build-up in their coronary arteries, and there would still be a very high chance they would develop coronary heart disease in their 70s.

Studies of soldiers killed in the wars in Korea and Vietnam provided an opportunity to define the prevalence of coronary atherosclerosis in young people. In 1953, Enos et al. described coronary lesions discovered at autopsy in 300 male soldiers (mean age, 22 years) killed in the Korean War. Gross evidence of coronary disease was present in 77% of the 300 decedents: 35% with vessel tissue thickening, 26% with a coronary artery narrowed by 10% to 49%, and 15% with a coronary blockage of 50% or more [17]. In 1971, McNamara et al. reported evidence of coronary atherosclerosis in 45% of 105 Vietnam War combat deaths (mean age, 22 years), with 5% having severe coronary disease [18]. In their concise descriptive narratives, these studies provided unequivocal evidence of the silent burden of coronary atherosclerosis in young and apparently healthy adults and also explained the steady rate of coronary heart disease diagnoses despite people's rising awareness of the disease [19]. Stents play a critical role in the treatment of coronary heart disease since inserting a stent is usually the last resort to reopen the blocked or severely narrowed coronary artery, through which the oxygen-rich blood flows to the patient's entire body. A small percentage of stent failure could mean millions of lives are being lost to coronary heart disease; on the other hand, a small improvement in stent technology could lead to the survival of countless more patients.

## 1.2 The evolution of stenting treatment

The evolution of stenting treatment started from the invention of balloon angioplasty. During this procedure, a specially designed catheter with a small balloon tip is guided to the point of narrowing in the artery. Once in place, the balloon is inflated to compress plaque against the artery wall and stretch the artery open. Balloon angioplasty was first performed in 1977 by Andreas R. Gruentzig [3], who joined Emory University Hospital in 1980.

Balloon angioplasty changed the landscape of coronary artery disease treatment, but the technique had several detrimental drawbacks, including vessel recoil or closure [3]. A question emerged: would balloon angioplasty be more effective if the balloon pushed a mesh structure into the vessel wall to provide more permanent support inside the coronary artery after the catheter was withdrawn? Soon technological advancement prompted the realization of this idea: a metal mesh that we now call a stent was first implanted in a human in 1986 [20]. The first type of stent was later referred to as a bare-

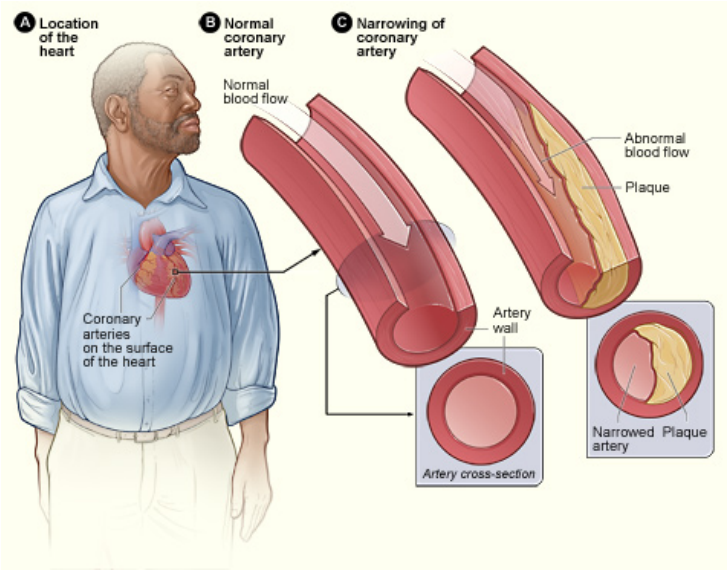


Figure 1.1: A: The location of the heart in the body. B: A normal coronary artery with normal blood flow. The inset image shows a cross-section of a normal coronary artery. C: A coronary artery narrowed by plaque. The buildup of plaque limits the flow of oxygen-rich blood through the artery. The inset image shows a cross-section of the plaque-narrowed artery [2].

metal (BME) stent, since it was made entirely of metal. The BMS soon replaced balloon angioplasty as the preferred method to open blocked coronary arteries, since the BMS had shown superior angiographic and clinical outcomes [4] [20]. Restenosis rates with bare-metal stents were reported to be between 16% and 44%, with higher rates of stenosis attributed to several risk factors - in particular, long lesions and small vessel calibers [4].

To prevent neointimal tissue growth and reduce restenosis, the drug-eluting stent (DES) was invented around 2001. DES's are coated with medication that is slowly eluted to the vessel to help keep the blockage from recurring. In general, DES's are preferred over BMS's for most people. By using DES's, restenosis rates were reduced to 0% in highly selective lesions and up to 16% in a broader range of patients and clinical subsets [21]. The impressive clinical results led the US Food and Drug Administration (FDA) to approve clinical use of DES in 2003. However, after the coating is dissolved, the remaining permanent metallic platform can cause several complications such as endothelial dysfunction and local hypersensitivity reactions, increasing the risk of thrombosis and restenosis [4].

Since the permanent metallic structure that remains in the vessel wall is the major factor in sustained inflammation, persistent vessel dysfunction, and even restenosis, a new concept became appealing: a bioresorbable vascular stent (BVS) made of a totally degradable polymer platform with a drug coating. Such type of stent should provide firm support inside the vessel in 6 months after implantation. The stent can be fully dissolved in 3 years, leading to long-term restoration of vessel anatomy, physiology, and functionality [4]. In particular, the BVS produced by Abbott Vascular have been developed and tested in first-in-man (FIM) studies that show encouraging imaging and clinical results up to 3-years follow-up thus far. These endeavors have led the gradual maturation of a novel field in interventional cardiovascular medicine, that of vascular restoration therapy. Bioresorbable stents are the newest breakthrough in the evolution of stenting technology, and the outcomes of ongoing clinical trials are eagerly anticipated to determine if these novel stents will further improve clinical outcomes [4].

## 1.3 Bioresorbable vascular stent (BVS)

Among a small family of bioresorbable stents, the Abbott ABSORB (Abbott Vascular, Santa Clara, CA) is the leading model, as it is the only BVS

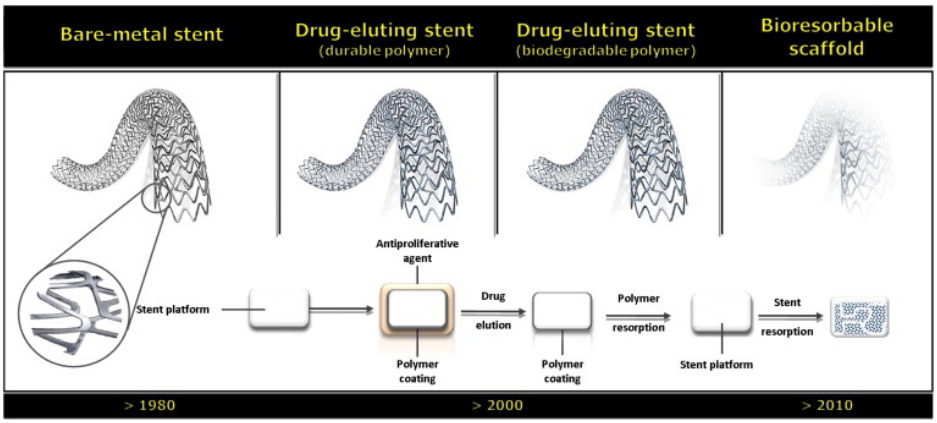


Figure 1.2: Stent platform components and evolving innovations [3].

approved for clinical use in Europe and is likely to be the first BVS approved by the US FDA (see Figure 1.3). The reconstruction and simulation process presented in Chapters 3 - 7 are based entirely on this stent model. It is necessary to describe the properties of this innovative product and evaluate them from a clinical point of view.

The ABSORB BVS has a polymer backbone made of semicrystalline poly-l-lactide (PLLA) and a polymer coating of lower crystallinity made of poly-d-l-lactic acid, which controls the release of the drug agent that prevents plaque regrowth. The first-generation ABSORB BVS 1.0 device had circumferential sinusoidal hoops (referred to as "rings") linked either directly or by straight polymeric bridges (referred to as "beams") with a strut thickness of 156 $\mu m$ (including the polymer–drug coating). After the stenting procedure, lumen loss, defined as the reduction of the space for the blood flow, was measured, and the results were better than those for a BMS but slightly worse than those for a DES. Insights from the ABSORB cohort trial suggested that the BVS is more conformable than metal stents, resulting in less vascular straightening and greater retention of the original angulation and curvature of the vessel. But the first generation suffered from the loss of radial support during the resorption. Soon, the second-generation BVS, the ABSORB BVS 1.1, was developed. The ABSORB BVS 1.1 device was constructed from the same polymer (PLLA) as was the previous generation except for a different drug-release process that increased the duration of mechanical support and stent resorption. Strut thickness remained the same, but the backbone structure was redesigned to allow for more uniform vessel support.

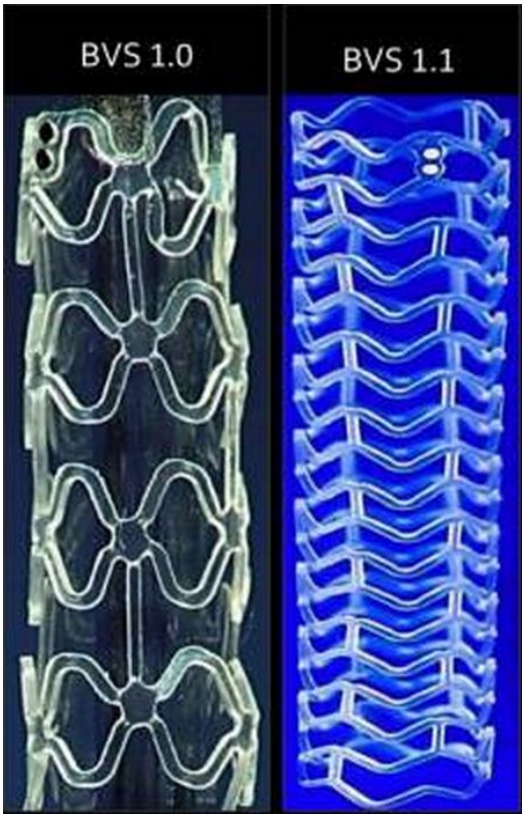


Figure 1.3: Abbott ABSORB BVS 1.0 (Left) and ABSORB BVS 1.1 (Right) [4].

The clinical potential of the ABSORB BVS is largely attributed to its ability to assist vessel restoration, which is true recovery of the coronary artery from coronary heart disease instead of a permanently stented vessel segment.

1) Restoration of vessel anatomy: The BVS may provide a more compliant platform to diminish the extent of disturbed flow patterns over the stented segments. The WSS oscillation, responsible for early or late vascular responses, is expected to disappear following scaffold resorption.

2) Restoration of vessel physiology: The liberation of the treated segment from a permanent metal structure may facilitate restoration of vessel pulsatility and motion as soon as the stent has been completely absorbed [22] [23].

3) Restoration of a low thrombogenic milieu: The risk of late or very late stent thrombosis may be reduced as the foreign material (platform + coating) is replaced by connective tissue and covered with matured endothelium.

4) Reduced in-stent neoatherosclerosis (atherosclerosis after stenting): The combination of complete stent resorption and regenerated intact endothelium with restored vessel motion may potentially reduce the risk of in-stent neoatherosclerosis.

There are limitations to BVS technology, including larger strut thickness that causes blood flow recirculation and impairs endothelialization [24], less deliverability, and the need for aggressive lesion preparation. Large studies with patient-specific computational fluid dynamics (CFD) and mechanical simulations are awaited to determine if the theoretical benefits outweigh these limitations and translate into improved clinical outcomes [3].

## 1.4 Medical imaging technology

The reconstructed stent and lumen geometry are patient-specific since they are based on the medical images of real patients after stent development. The two types of imaging technology we use are optical coherence tomography (OCT), which renders vessel cross sections, and angiography, which provides the curvature of the stented vessel.

### 1.4.1 Optical coherence tomography (OCT)

OCT is a catheter-based invasive imaging system. Using light rather than ultrasound, OCT produces high-resolution, in vivo images of coronary arteries and deployed stents [25]. The introduction of OCT into interventional cardiology was received with great expectation. Its light-based imaging modality offers 10 times higher resolution and 40 times faster imaging acquisition than that of intravascular ultrasound (IVUS), an older imaging technology. Semi-automated imaging analyses of OCT systems permit accurate measurements of luminal architecture and provide insights regarding stent apposition, overlap, and neointimal thickening [26]. OCT is particularly suitable for BVS, because BVS are made of translucent polymer with a different light refractive index from that of the vessel wall [27]. Therefore, OCT has been increasingly used in BVS studies and clinical trials to assess the rate of absorption accurately and to inspect the response of vessel walls [28]. Our methods for stent strut detection and lumen extraction from OCT are presented in Chapter 4 and Chapter 7, respectively.

### 1.4.2 Angiography

Angiography is a medical imaging technique used to visualize the lumen of blood vessels and other organs in the body, with particular interest in the arteries and the heart chambers. It is the conventional method for assessing arterial morphology, and it has been for decades the gold standard for the investigation of coronary artery disease. Angiography provides a detailed map of the arterial lumen in which atherosclerosis lesions are identified as local narrowing. Coronary angiography depicts the arterial lumen in 2D; however, biplane angiography enables us to extract the lumen centerline in 3D [29]. When biplane angiography images are taken while the catheter is in the artery, we can use the catheter path as the lumen centerline. The catheter path can be extracted from a set of imaging data points on the catheter trajectory.

Figure 1.4 shows a set of biplane angiography A and B. A set of points are chosen from the trajectory in image A denoted as $P_{A,i}$ and image B denoted as $P_{B,j}$:

$$P_{A,i} = \begin{bmatrix} x_i \\ y_i \\ z_i \end{bmatrix}, \; P_{B,j} = \begin{bmatrix} x_j \\ y_j \\ z_j \end{bmatrix} \tag{1.1}$$

Then the points are interpolated by B-splines, which are quite effective in noise suppression [30]:

$$C_A(u) = \sum_{i=1}^{n} N_i(u) P_{A,i}, \; 0 \leq u \leq 1 \tag{1.2}$$

$$C_B(s) = \sum_{j=i}^{n} N_j(s) P_{B,j}, \; 0 \leq s \leq 1 \tag{1.3}$$

where $N_i(u)$ and $N_j(s)$ are the third-degree B-spline basis function defined by uniform non-periodic knot vectors $u$ and $s$. Then the two B-spline curves $C_A$ and $C_B$ are swept normal to their X-ray angiography plane, forming two surfaces. The intersection of the two surfaces is a 3D curve, which represents the reconstructed catheter path [5] [29] [31] (see Figure 1.4). If the angiography presents clear catheter trajectories and over 100 more data points can be taken for matrices $P_{A,i}$ an $P_{B,j}$, then natural cubic splines could also suffice for the interpolation.

### 1.4.3 Thesis outline

In this thesis, we thoroughly describe the pipeline of the geometry reconstruction and simulation of a stented coronary artery. First, we investigate the background of patient-specific stent reconstruction and blood flow simulations. Many works in this area have inspired us, but we believe - as mentioned above - that the true patient-specific simulations rely heavily on an accurate reconstruction of the stent inside a patient's vessel.

The most distinct feature of our simulations is the separate stent geometry reconstruction, the methodology of which is revealed as the essence of this thesis. As the final goal, we have in mind the development of tools to assist systematically clinical trials (Computer Aided Clinical Trials - CACT). The first step of the stent reconstruction is the detection of stent strut points. The stent reconstruction is based on the strut points automatically detected from OCT images of real patients, the details of which are described in Chapter 4. Patient-specific stent reconstruction could be manually performed upon

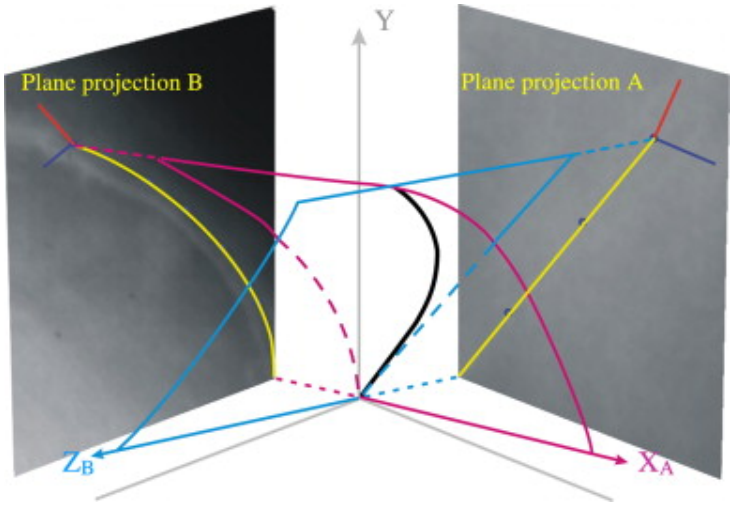


Figure 1.4: 3D catheter path reconstruction. The 3D catheter path is the intersection of the two surfaces which are derived from the extrusion of the path projections A and B [5].

the detected strut points by using computer-aided design (CAD) software, but the large number of the reconstructions requires us to come up with a semi-automatic stent reconstruction program. The first step toward stent reconstruction is the automatic strut detection from OCT images, which is described is Chapter 4. The rest of stent reconstruction, from creating the stent wire-frame to adding stent volume, is described in Chapter 5. This thesis also describes a method for constructing the stented lumen that is compatible with the stent geometry in terms of CFD domain creation. We are able to extract from the angiography the curvature of the stented vessel from the angiography, which is applied to both the stent and lumen. Then we present the results of CFD simulation along with analysis of important quantities, such as the WSS, and their clinical implications.

In total we have successfully used the stent and lumen reconstruction on three patients: Case 1 (20135-089-RFO-1), Case 2 (27716-012-RCA-1), Case 3 (27299-024-LCX-3). At the time we worked on Case 1, the automatic stent strut detection from OCT had not been developed, thus the struts were detected manually. For Case 2 and 3, the stent struts were detected automatically using the method described in Chapter 4. All three cases have geometry fully reconstructed with curvatures obtained from their corresponding angiography. As of CFD, we present simulations results of Case

1, 2 and 3 with patient-specific curvatures, and Case 2 without curvature in Chapter 7. The simulations have been fully visualized and analyzed for future publications.

The stent reconstruction method, with modification, can be extended to metallic stents. For either BVS or metallic stents, the constructed patient-specific stent geometries are not limited to CFD simulations. They could also be used for structural analysis and drug assimilation simulations. Last but not least, we point out some possible future directions of this research.

# Chapter 2

# Background

## 2.1 Comparison to related work

The investigation of the relationship between hemodynamics conditions and atherosclerosis dates back to 30 years ago. In 1985, D. Ku and D. Giddens et al. discovered a positive correlation between low and osculating WSS and plaque location [32]. At the time, OCT and angiography were not available to access the plaque location and reconstruct the vessel geometry, so D. Ku and D. Giddens et al. used human postmortem carotid specimens to locate and measure plaque. Then they pumped a mixture of water and glycerin adjusted to blood viscosity into a glass model of carotid based on human carotid measurement. The velocity of the fluid was measured with a laser Doppler anemometer system at several locations in the glass carotid model. The study revealed that low mean shear stress and marked oscillations in the direction of WSS may be critical factors in the development and localization of atherosclerotic plaques [32].

With the advancement in imaging technology and computing power, in the last two decades, numerical models, instead of physical glass or plastic models, have become well recognized and widely adopted tools to investigate stenting procedures [33]. But early numerical studies only involved simplified cases and idealized stented arteries [33]. One study in 2006 suspected that local hemodynamics conditions might influence neointimal proliferation following conventional stent implantation. To assess the relationship between WSS and neointimal thickness after coronary stenting, 3D geometry of the inner vessel wall and outer vessel wall was reconstructed by merging patients'

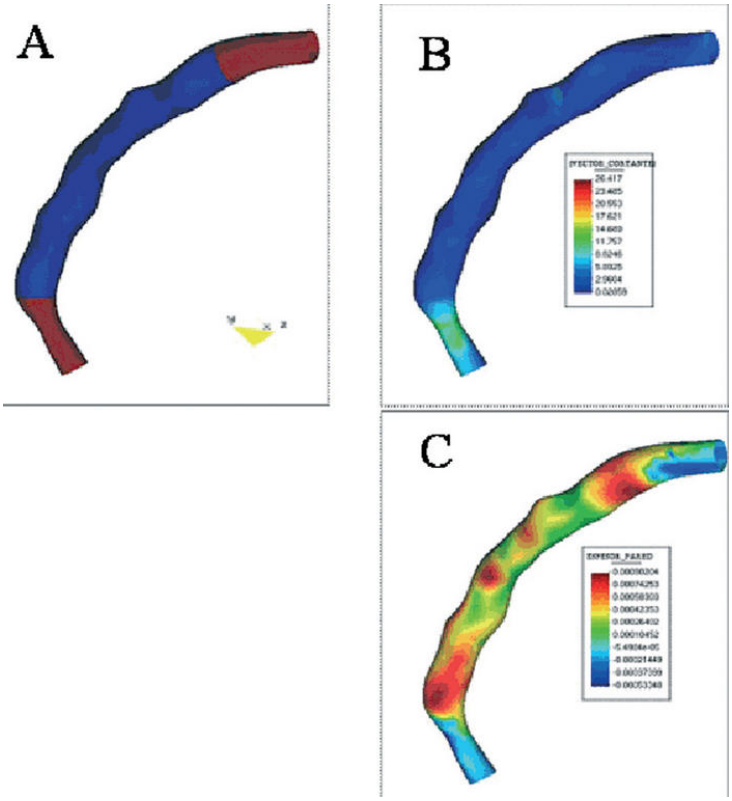


Figure 2.1: (A) Geometric reconstruction of the stented segment of a vessel using IVUS and Angiography. (B) WSS of the vessel obtained from CFD simulations. (C) Neointimal thickness of the reconstructed [6].

angiography and intravascular ultrasound (IVUS). This study represents a series of similar simulation work using the geometry constructed from IVUS. Due to the low resolution of IVUS, such geometry shows no stent appearance but only a very general shape of lumen (Figure 2.1). CFD simulations were performed using the finite volume method, and the results show a negative correlation between WSS and neointimal thickness. However, without stent geometry, true local hemodynamics conditions around the strut were unavailable, and the negative correlation between WSS and neointimal thickness was extremely weak, leading to a rather ambiguous conclusion that more potent factors are certain to be involved in neointima formation [6].

It is critical to have stent geometry, as it is required when accessing the WSS and the blood flow pattern around the stent struts. A study in 2009

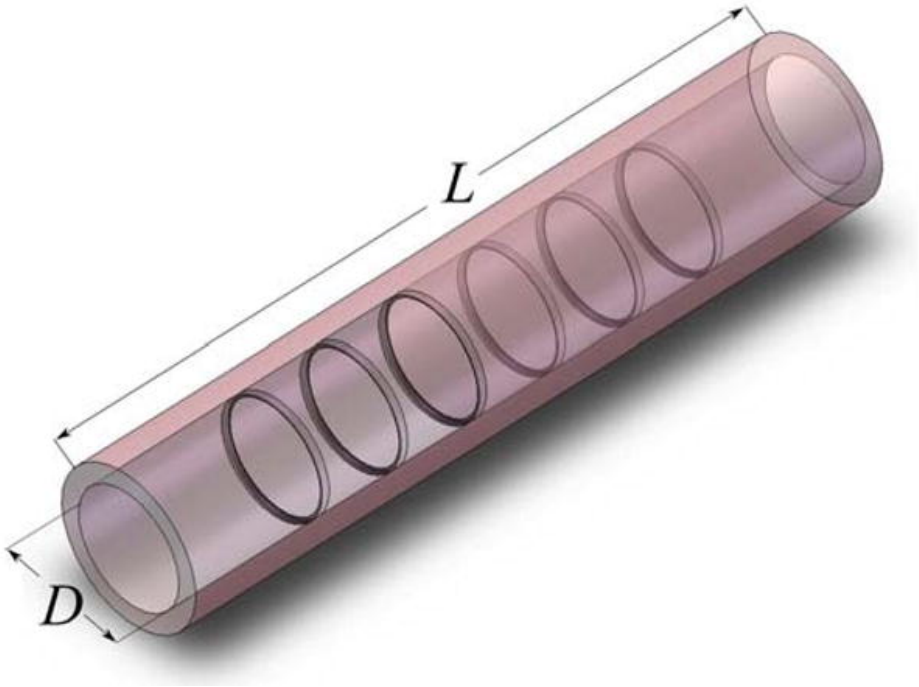


Figure 2.2: The arbitrary geometry of the stented coronary artery with six independent rings representing the architecture of a simplified stent [7].

sought to incorporate stent geometry in its CFD because the results would offer valuable suggestions to creat better stent design. This study is based on pure abstract geometry (Figure 2.2). The vessel is represented by a cylinder, and the stent is represented by six rings with rectangular cross sections.

The CFD domain is the difference between the inner vessel wall and the six rings. Navier-Stokes equations for incompressible blood flow is solved in the CFD domain:

$$\begin{cases} \dfrac{\partial u}{\partial t} + u \cdot \nabla u - \dfrac{\nu}{\rho}\Delta n = -\dfrac{1}{\rho}\nabla p & \text{Navier-Stokes equation} \quad (2.1) \\ \nabla \cdot u = 0 & \text{Incompressible fluid} \quad (2.2) \end{cases}$$

where $u$ is velocity, $p$ is pressure, $\rho$ is blood density, and $\nu$ is blood viscosity. If the above system of equations is solved in 3D Cartesian coordinate system, then $u = [u_x, u_y, u_z]$, and the Navier-Stokes equation 2.1 expands to

$$\frac{\partial u_x}{\partial t} + \left( u_x \frac{\partial u_x}{\partial x} + u_y \frac{\partial u_x}{\partial y} + u_z \frac{\partial u_x}{\partial z} \right) - \frac{\nu}{\rho} \left( \frac{\partial^2 u_x}{\partial x^2} + \frac{\partial^2 u_x}{\partial y^2} + \frac{\partial^2 u_x}{\partial z^2} \right) = -\frac{1}{\rho} \frac{\partial p}{\partial x} \tag{2.3}$$

$$\frac{\partial u_y}{\partial t} + \left( u_x \frac{\partial u_y}{\partial x} + u_y \frac{\partial u_y}{\partial y} + u_z \frac{\partial u_y}{\partial z} \right) - \frac{\nu}{\rho} \left( \frac{\partial^2 u_y}{\partial x^2} + \frac{\partial^2 u_y}{\partial y^2} + \frac{\partial^2 u_y}{\partial z^2} \right) = -\frac{1}{\rho} \frac{\partial p}{\partial y} \tag{2.4}$$

$$\frac{\partial u_z}{\partial t} + \left( u_x \frac{\partial u_z}{\partial x} + u_y \frac{\partial u_z}{\partial y} + u_z \frac{\partial u_z}{\partial z} \right) - \frac{\nu}{\rho} \left( \frac{\partial^2 u_z}{\partial x^2} + \frac{\partial^2 u_z}{\partial y^2} + \frac{\partial^2 u_z}{\partial z^2} \right) = -\frac{1}{\rho} \frac{\partial p}{\partial z} \tag{2.5}$$

and equation 2.2 becomes

$$\frac{\partial u_x}{\partial x} + \frac{\partial u_y}{\partial y} + \frac{\partial u_z}{\partial z} = 0. \tag{2.6}$$

Even though being deprived of a real connection with actual patients' imaging data, the arbitrary geometry (Figure 2.2) provides one advantage: the constructed CFD domain is completely axis-symmetric with respect to the centerline of the vessel, hence the Navier-Stokes equation for incompressible fluid can be solved in the $(l, r)$ cylindrical coordinate system as opposed to the 3D Cartesian system $(x, y, z)$. Then $u = [u_l, u_r]$, the axial and radial velocity components respectively. The independent variable $l$ and $r$ are the stream-wise and radial spatial coordinates. In the cylindrical coordinate system, the equation 2.1 expands to

$$\frac{\partial u_l}{\partial t} + \left( u_l \frac{du_l}{\partial l} + u_r \frac{\partial u_r}{\partial r} \right) - \frac{\nu}{\rho} \left[ \frac{1}{r} \frac{\partial}{\partial r} \left( r \frac{\partial u_1}{\partial r} \right) + \frac{\partial^2 u_1}{\partial l^2} \right] = -\frac{1}{\rho} \frac{\partial p}{\partial l} \tag{2.7}$$

$$\frac{\partial u_r}{\partial t} + \left( u_l \frac{\partial u_r}{\partial l} + u_r \frac{\partial u_r}{\partial r} \right) - \frac{\nu}{\rho} \left[ \frac{l}{r} \frac{\partial}{\partial r} \left( r \frac{\partial u_r}{\partial r} \right) + \frac{\partial^2 u_r}{\partial l^2} - \frac{\nu}{r^2} \right] = -\frac{1}{\rho} \frac{\partial p}{\partial r} \tag{2.8}$$

and equation 2.2 becomes

$$\frac{\partial u_l}{\partial l} + \frac{1}{r} \frac{\partial \left( r u_r \right)}{\partial r} = 0. \tag{2.9}$$

Because the results are indifferent with respect to the azimuthal coordinate $\theta$, the computational cost with cylindrical coordinate system is cut down by one dimension with the above set-up.

To simulate the pulsatile blood flow, a parabolic velocity inlet boundary condition is prescribed:

$$u\left(r,t\right)=\frac{1.525\rho}{4\mu}\left[\left(\cos\left(2\pi t\right)+1.55\right)\left(\left(\frac{D}{2}\right)^{2}-r^{2}\right)\right]. \tag{2.10}$$

The simulation demonstrates that recirculation occurs behind stent struts. Such recirculation entraps pro-coagulant micro-particles and accelerates thrombosis; therefore a more streamlined strut shape is proposed (see Figure 2.3) [7]. WSS can also be computed in the $(l,r)$ cylindrical coordinate system:

$$S_{w}=v\left(\frac{\partial u_{1}}{\partial r}+\frac{\partial u_{2}}{\partial l}\right). \tag{2.11}$$

Though less clinically convincing, this simulation has its merits, as it brings to light the thrombosis-inducing circulations behind the struts. In fact, before our work on patient-specific stent reconstruction, we conducted a similar preliminary study using a more realistic stent geometry (Figure 3.1b) instead of only a few circular rings.

The combination of IVUS and angiography made 3D reconstruction of a stented vessel possible but failed to show a clear stent structure. Compared with IVUS, the newer OCT technology is a leap forward in assessing coronary vessels from an anatomic standpoint, offering much higher resolution and richer information. Soon, researchers realized that the fusion of angiography with OCT can produce more realistic geometry than can the combination of angiography and IVUS. In recent research work on the reconstruction of stented coronary artery, it is widely accepted that OCT, instead of IVUS, should be used with angiography to produce more geometrically correct models enabling reliable WSS assessment in the strut level. In another study, a stented coronary artery was reconstructed by manual segmentation of the OCT images, and blood flow was simulated as steady incompressible flow [8]. We can see the improvement on the quality of the geometry (Figure 2.4); however, the stent architecture is blurred due to the smoothing process. The blood flow streamlines on the micro-environment demonstrate recirculation, which is consistent with the virtual study done by Jimenez et al., but the strut shape is not realistic: in only 14 days after implantation, the strut cross section should still be in a full square shape because it took three years for Abbott BVS to dissolve.

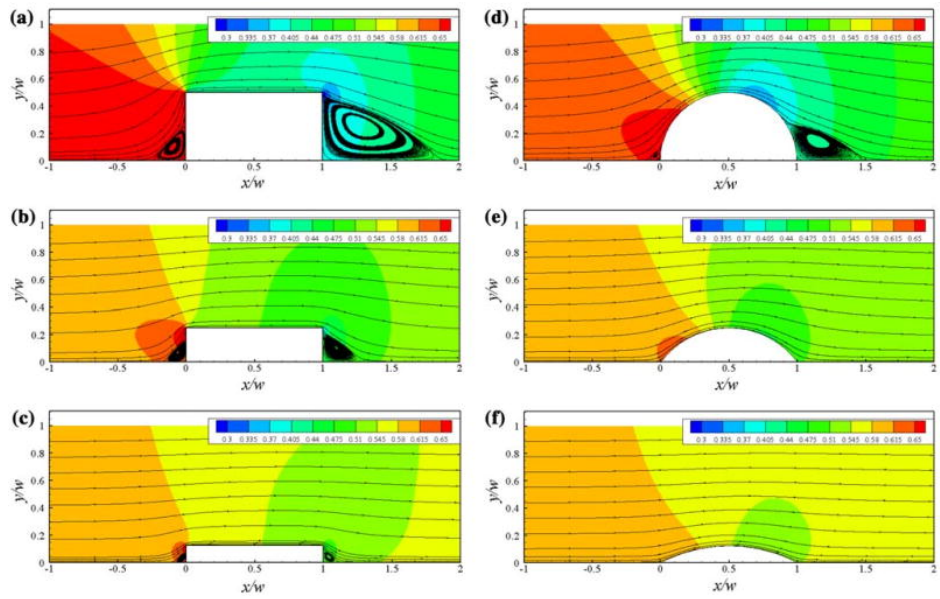


Figure 2.3: Streamlines with pressure in the background, flow field in the vicinity of (a)-(c) rectangular stent struts and (d)-(f) the proposed circular arc stent struts, for different length/width ratios 2:1, 4:1, and 8:1 [7].

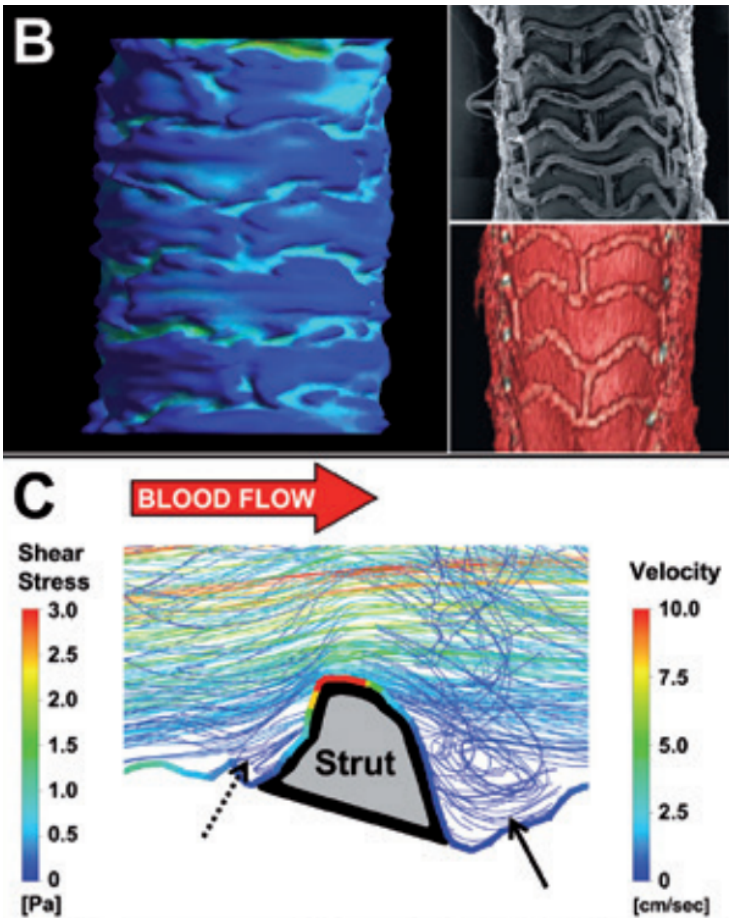


Figure 2.4: Two figures from the work of Papafaklis et al.: (B) WSS on the 3D reconstructed surface of stented coronary artery. An electron microscopy photo (top right) and an 3D volume-rendered image of the stented artery are displayed. (C) 2D Blood flow streamlines around the strut demonstrate flow disturbance with large a recirculation region distal to the strut (solid arrow) and a much smaller one proximal to the strut (dotted arrow) resulting in very low and low WSS, respectively, as demonstrated by the color-coded WSS map superimposed on the lumen/strut border [8].

In 2014, a similar study was conducted in vivo (see Figure 2.5). The stent pattern is visible in the reconstructed geometry, but again no clear stent architecture is present. The longitudinal view showed a flow recirculation zone, which is believed to have affected neointima formation [9]. Nonetheless, the curvy strut cross section in Figure 2.5 is far from being real. The struts should still be in a box-shape in the baseline stage.

Another approach to construct stented vessel geometry is to combine the patient-specific lumen geometry constructed from angiography with a virtually deployed stent. Virtual stent deployment is achieved using a series of Boolean operations. The general virtual deployment method was first introduced and described by Gundert et al.. Then Ellwein et al. customized and implemented this method for the simulations of the drug-eluting CYPHER stent (Cordis Corporation, Bridgewater, NJ) [10]. Separate solid models of the vessel lumen and the lofted outer surface of the stent were constructed from the white and cyan segments of the OCT images (Figure 2.6a), respectively, using the procedure described in Stages A-D above (Figure 2.6b and 2.6e). The stent radial thickness was then subtracted from the solid model of the lofted stent to create a thinner lofted stent model (Figure 2.6b). Subtracting the thinner lofted stent model from the thick stent yielded a stent model that mimicked the inner surface of the stent (Figure 2.6c and 2.6d). The final subtraction of this stent model from the lumen model (Figure 2.6f) generated the flow domain (Figure 2.6g) which was used for subsequent CFD simulations [10].

It is evident that stent modeling is still a wide research area. Innovations of interventional procedures and new medical devices may obtain benefits from computational studies, and geometrical modeling should be applied to more realistic cases and more thoroughly validated [33]. Much effort still need to be made in the geometry reconstruction of stented vessel. To achieve more realistic blood flow and WSS, the stent geometry should be the priority. Here we propose an entirely different mythology for the reconstruction: constructing the stent and the lumen geometry separately. Before we detail the geometrical processing underlying our work, it is worth to give a preview of our CFD results using our new construction method in order to demonstrate the improvement on the quality of the simulations (Figure 2.7). Comparing to previous work, in our simulation the stent architecture is fully emerged. The stent pattern is clear and the struts have full volume as they are supposed to be in baseline stage. Such patient-specific geometry enables us to draw more conclusions on the relationship between WSS and neointimal

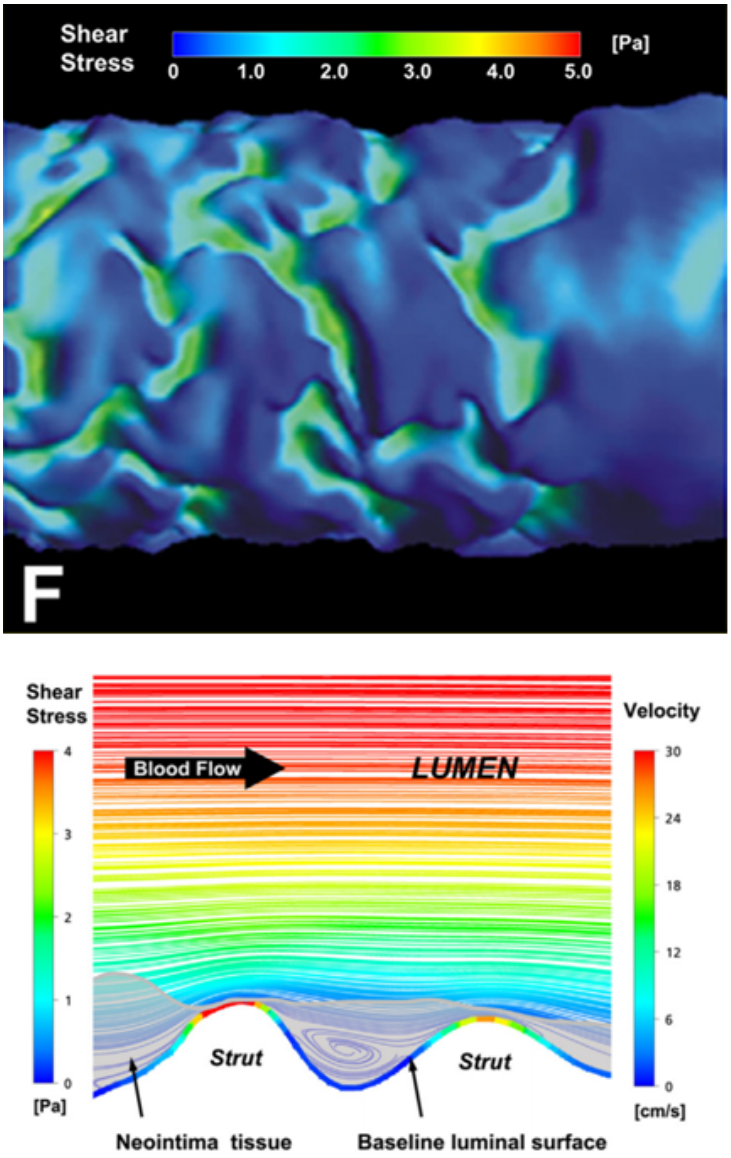


Figure 2.5: Two figures from the work of Bourantas et al.: (Top F) WSS on the 3D reconstructed surface of stented coronary artery in baseline. (Bottom) 2D Visualization of Blood flow streamlines around the strut demonstrate flow disturbance with a recirculation region between to struts, resulting in low WSS as demonstrated by the color-coded WSS map superimposed on the lumen/strut border. The struts are over-smoothed, because in baseline (post deployment) the strut cross-section should be box-shaped [9].

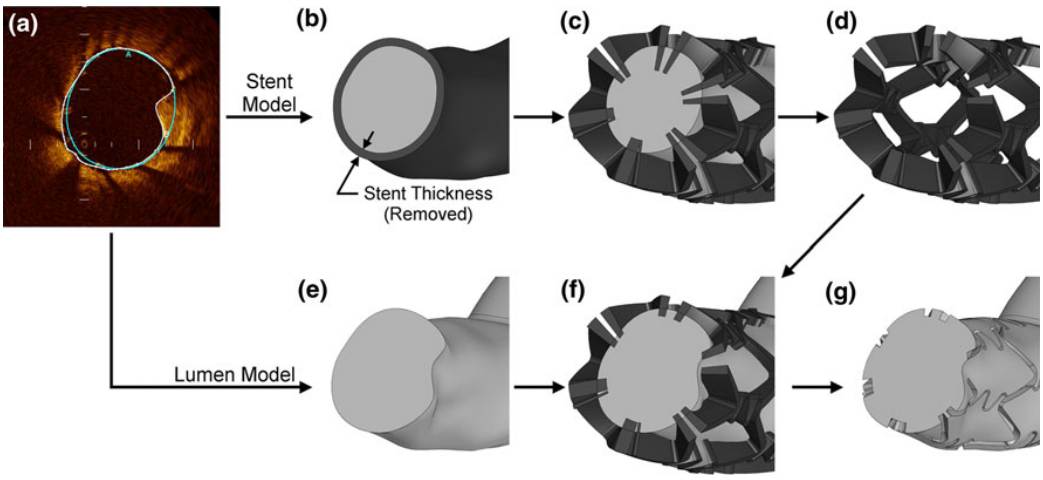


Figure 2.6: Method of virtual stent implantation. Solid models of the outer surface of the stent (b) and vessel lumen (e) were lofted from the white and cyan segmentations of the OCT images (a). The stent radial thickness was subtracted from the model of lofted stent segmentation (b), which was subsequently subtracted from a thick stent model (c) to create a customized stent model (d) for this stent. Subtracting the customized stent model (d) from the lumen model (e) as shown in (f) generated a computational representation of the blood flow domain (g) [10].

thickness. We also confidently show the blood flow streamlines in 3D instead of 2D, which verifies the existence of recirculation behind BVS strut in most patient-specific sense. The methodology we created to achieve such patient-specific simulations is the essence of the this thesis and will be unveiled in the next few chapters.

## 2.2 Previous work on patient-specific assessment of bioresorbable stent

In 2012 and 2013, our interdisciplinary group also attempted to construct patient-specific geometry similar to that of Bouranta et al. and Papafaklis et al.. We dedicate this section to briefly summarize this work which was published in 2013. The patient-specific reconstruction/simulation method presented in Chapter 4, 5, 6, and 7 is an significant advancement over the work presented in this section.

Several devices have undergone first-in-man studies. Although the polymeric struts of the ABSORB BVS are thicker (156 mm) compared with metallic stents, the hemodynamic effects change over time as the scaffold resorbs. Therefore, the overall biomechanical footprint of the bioresorbable scaffold compared with that of metal stents is transient, with different effects on local vessel and strut-level WSS (WSS). We have proposed that such detailed biomechanical evaluation of the ABSORB BVS will add critical mechanistic insights into its potential beneficial effects, particularly in angulated and curved vessels [34]. Here we illustrate the assessment of biomechanical properties by two methods in two selected patients who underwent implantation of the ABSORB BVS. The evaluation used 3D angiographic reconstruction techniques and CFD to calculate the WSS pre- and post-BVS deployment (Figures 2.8A to 2.8D) for vessel-level analysis. The second used optical coherence tomography (OCT) imaging data to reconstruct the 3D geometry and CFD to visualize flow streamlines over the polymeric struts for more detailed strut level analysis (Figures 2.8E and 2.8E'). Fusion of angiographic with OCT data has been previously shown to be a feasible approach to calculate WSS by CFD simulations [35], and biomechanical analyses by these methods may yield important insights into potential advantages of bioresorbable technologies over metal stents. Compared with IVUS, the newer OCT technology is a leap forward in assessing coronary vessels from an

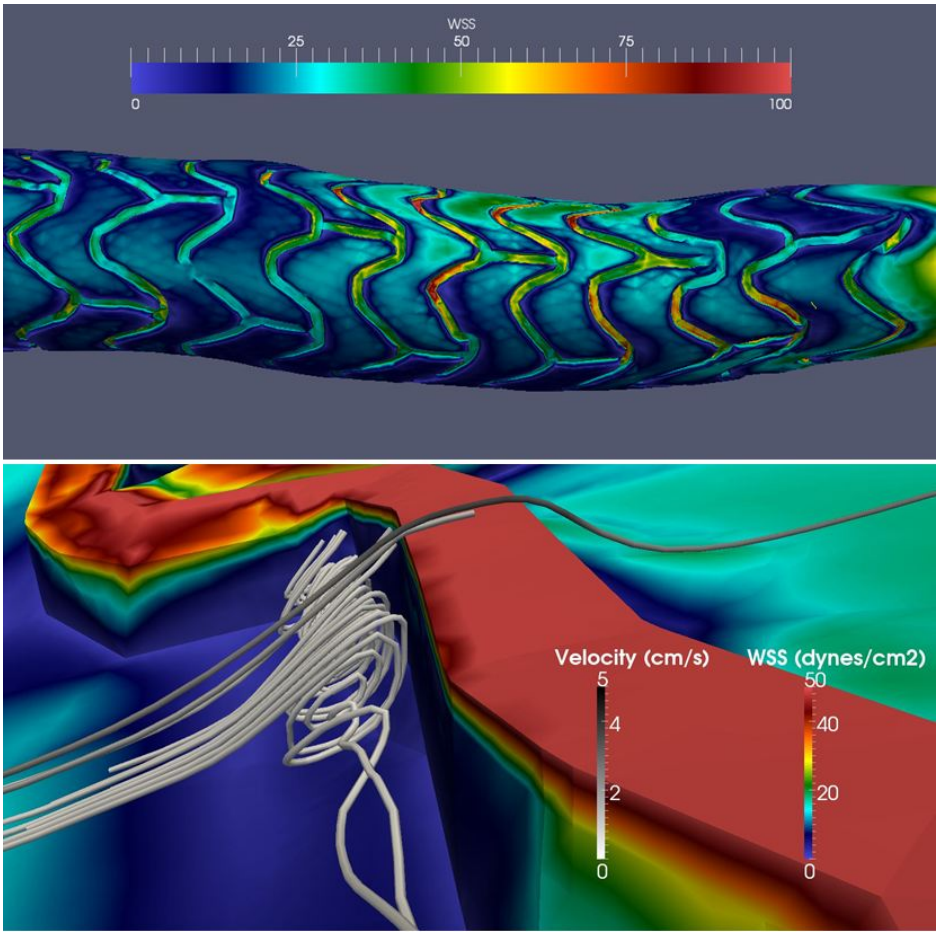


Figure 2.7: (Top) WSS results from the patient-specific simulations. (Bottom) Blood flow recirculations behind the a stent strut.

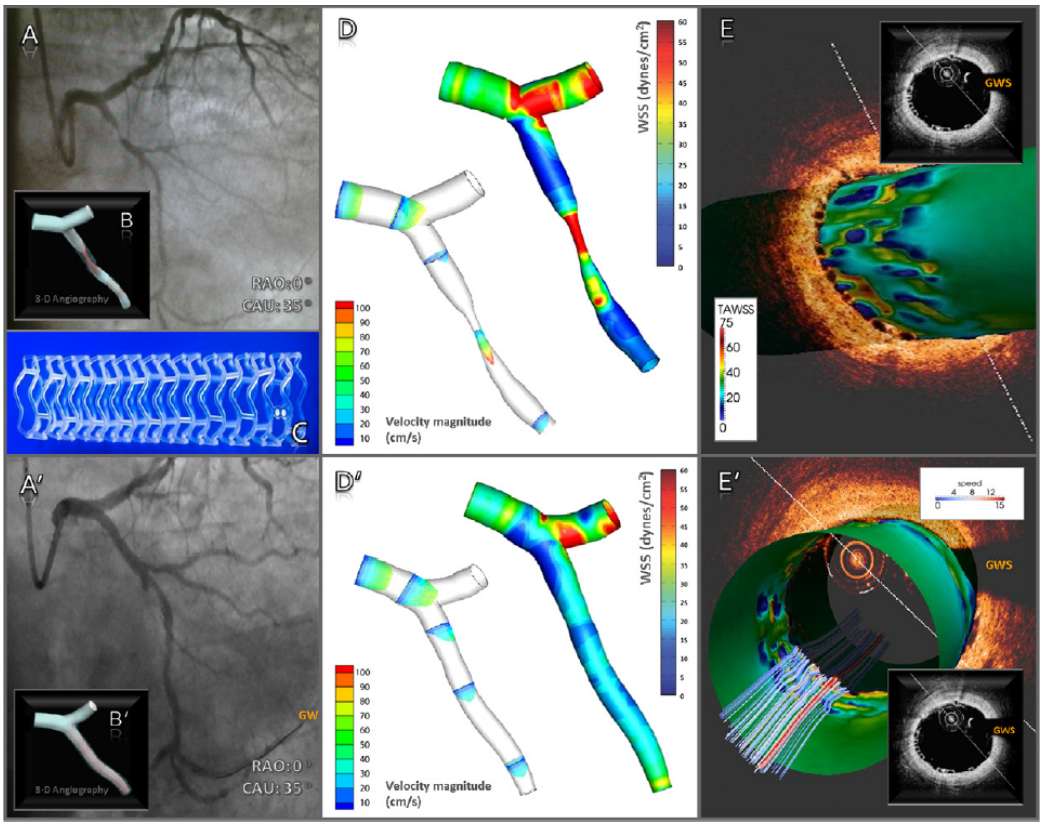


Figure 2.8: Presentation of WSS Derived From Angiographic and OCT Imaging Data Using CFD Simulations After Implantation of the Absorb Bioresorbable Vascular Stent. (A, A') Two-dimensional (2-D) angiographic views of the significant proximal left circumflex artery (A) and the stented segment after implantation of Absorb BVS (A'). (B, B') 3D angiographic views before (B) and after (B') stent implantation. (C) The Absorb BVS. (D, D') WSS magnitude distribution from angiographically derived 3D geometries before (D) and after (D') stent deployment. Velocity profiles pre- and post-implantation of the Absorb BVS are superimposed. (E) 2D OCT cross section with embedded polymeric struts demonstrating in a 3D pattern the distribution of WSS between the polymeric struts. The quantified color coding demonstrates low WSS regions (blue color). The matched OCT cross section is superimposed. (E') Reconstructed streamlines of the velocity field at the systolic peak demonstrating disturbed flow patterns in the proximity of the arterial wall induced by the polymeric struts [11].

anatomic standpoint, offering much higher resolution and richer information. The high resolution of OCT led to the appearance of some stent struts in the reconstructed geometry (Figures 2.8E and 2.8E') [11]. The CFD with the use of such geometry show disturbed blood flow around the struts. However, the method of simply stacking the OCT images can only show shattered stent struts, and the stent architecture is completely lost due to the noise. A better reconstruction method is still needed to create high-quality stent geometry.

## 2.3 Motivations and objectives

BVS is an innovative product that could truly restore a patient's coronary vessel to its natural state, but BVS has not yet met expectations regarding its reliability. Many researchers in cardiology and bioengineering have been drawn to study BVS because of its novelty and huge clinical potential. Several questions regarding BVS should be answered. Does the thick strut cause blood recirculation and a high degree WSS oscillation? If yes, are the recirculations and oscillations the major reason for plaque progression? If yes again, will the problems vanish as the struts become thinner in the resorption process? In addition, will the strut still be strong enough to support the vessel after it is partially absorbed? Ultimately, how shall BVS be improved to lower the risk of retenosis and to benefit more patients? The answers to all these questions require patient-specific simulations of stented arteries. Those questions motivate us to analyze the stent deployment and the blood flow in the stented vessel with simulations that truly reflect the hemodynamics inside the stented artery. All the work presented in this chapter inspired us, but they fall into three categories of shortcoming: 1) using entirely arbitrary geometry, 2) using patient-specific lumen but a virtually deployed stent, and 3) using patient-specific geometry with either a vague or no appearance of the stent. Our challenge is to conduct simulations that have both patient-specific stents and lumen geometry. This requires a stent reconstruction methodology that can reveal the stent's true shape and position in the vessel. In addition, we will not stop only after a handful of patients have been simulated; we aim to process hundreds of patients so that we can draw powerful conclusions that are statically convincing. Therefore, our goal is to develop a reconstruction and simulation procedure that can automatically produce highly realistic patient-specific stent geometries and simulations efficiently.

# Chapter 3

# Preliminary assessment with idealized geometry

Three-dimensional design simulations of coronary metallic stents utilizing mathematical and computational algorithms have emerged as important tools for understanding biomechanical stent properties, predicting the interaction of the implanted platform with the adjacent tissue, and informing stent design enhancements. It is important to conduct CFD simulations with patient-specific geometry of the stented artery. In Chapter 2, however, we showed that attempting to reconstruct patient-specific geometry by stacking either IVUS or OCT images often leads to geometry with minimal or no resemblance to the stent. The stent geometry is critical, because with it the simulation results can show how the stent affects blood flow and WSS. In order to demonstrate the stent-flow interaction, Jimenez et al. used manually constructed stent geometry in their simulations. We refer to this type of geometry as "idealized geometry" because it is an arbitrary representation rather than being based on patients' medical images. In Chapter 4 and 5, we will present our methodology of patient-specific stent geometry reconstruction from OCT and angiography. However, in 2013 and 2014 we also conducted a preliminary study with idealized geometry, similar to that of Jimenez et al.. Compared to the Jimenez study, our study used much more realistic stent geometry. As shown in Figure 3.1, Jimenez et al. used six rings to represent the implanted stent, whereas we used stent geometry that was almost identical to the original stent design of the Abbott ABSORB BVS. With idealized stent geometry, we can control the degree of embedding, the strut thickness, and also the curvature of the vessel. By these means, virtual stent

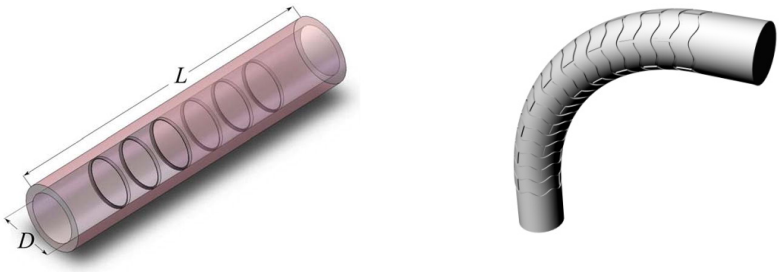


(a) (b)

Figure 3.1: (a) The idealized geometry used by Jimenez et al.. (b) The idealized geometry used in our preliminary study.

deployment is achieved. In this chapter, we demonstrate the hemodynamic implications following virtual deployment of bioresorbable stents using finite element methods and advanced CFD simulations to visualize the stent-flow interaction immediately after implantation and following stent resorption over time.

CFD simulations with time-averaged WSS quantification following virtual bioresorbable stent deployment in idealized straight and curved geometries were performed. WSS was calculated at the inflow, at the endoluminal surface (top surface of the strut), and at the outflow of each strut surface post-procedure (stage I) and at a time point when 33% of stent resorption had occurred (stage II) (see Figure 3.2). The implementation of CFD simulations over virtually deployed bioresorbable stents demonstrates the transient nature of stent-flow interactions as the bioresorption process progresses over time. Such hemodynamic device modeling could be useful guide future bioresorbable stent design.

## 3.1 Overview on simulations with idealized geometry

Recent data suggest that variations in the local hemodynamic environment after stenting cause regional WSS alterations that can invoke a differential vascular healing response around the stent struts [36]. The vessel geometry after stenting is determined by several factors, including material properties

of the stent, strut thickness of the stent, and underlying plaque composition. By design, bioresorbable devices have thicker struts in order to retain the necessary support for the vessel. The thick struts impair local blood flow; however, such impairment is expected to reduce during the stent resorption. Furthermore, bioresorbable devices offer a more compliant platform that limits vascular straightening and thus reduces disturbed flow patterns at the proximal and distal edges. Although critical to understanding healing and long-term performance of stents, these dynamic WSS alterations are difficult to measure in vivo as it would require detailed measurements taken different time points through an invasive procedure.

The use of computational modeling techniques to assess the performance of isolated or virtually deployed coronary stents has been proven to be effective in predicting their mechanical behavior over time. These numerical simulations provide a preliminary "proof-of-concept" for new technologies to further qualify their suitability for clinical application [37].

Herein, we provide a series of three-dimensional simulations in idealized geometries focusing at the strut level at two different time points: stage I, which represents the post-implantation stage of the virtually deployed stent, and stage II, which represents the time point where 33% of stent resorption has been achieved. Each of these stages focuses on the anatomic configuration of the struts. In particular, three distinct portions of the lateral surfaces were defined: (1) the lateral inflow surface where the strut surface faces the inflow area; (2) the lateral outflow surface where the strut surface faces the outflow area; and (3) the endoluminal surface or top of the strut facing the lumen (see Figure 3.2). During stage II, two distinct phenomena take place: neointimal tissue generation and bulk resorption of the stent, which affect its spatial dimensions and subsequently local flow conditions (see Figure 3.2).

Our goal was to test the hypothesis that local hemodynamic conditions derived from advanced CFD simulations change as the virtually applied bioresorption progresses over time. These observations may potentially translate to improved flow patterns over the stented segments or the stent edges, which in the clinical setting affect local tissue responses.

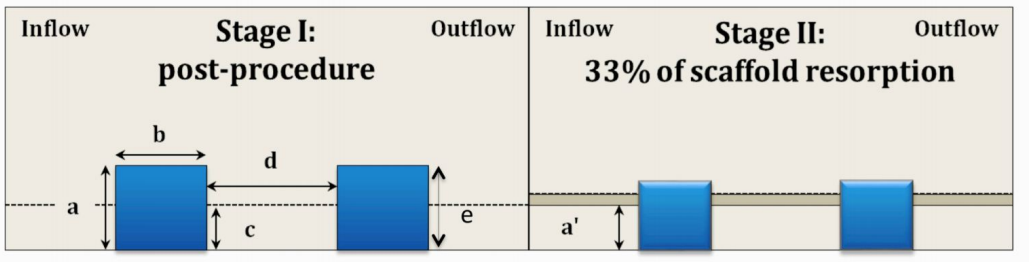


Figure 3.2: (stage I) a: lateral inflow strut surface is 0.015 *cm* (150 $\mu m$), b: endoluminal strut surface, c: distance from vessel wall is 0.0075 *cm* (half embedded strut), d: distance between struts is 0.10 *cm*, e: lateral outflow surface. (stage II): a': 0.010 *cm* (100 $\mu m$), the gray lane presents the generation of neointimal tissue.

## 3.2 Method

### 3.2.1 Geometric reconstruction of the stented vessel

The geometry of the deployed stent was constructed based on the structure of an actual 3.0 by 18 mm ABSORB BVS (Abbott Vascular, Santa Clara, CA) using the validated CAD software Rhino 5.0 (McNeel, Seattle, WA, `http://www.rhino3d.com`) for geometry reconstruction. We modeled 19 horizontal rings interconnected by three vertical bridges or "beams." We performed simulations of two idealized vessel geometries: a straight vessel and a curved vessel with a 90° angle. We examined two stages in each vessel model. In stage I, the post-implantation stage, the strut thickness was 0.015 *cm* (150 *mm*), the distance between each strut 0.1 *cm*, the degree of embedding in the vessel wall 50% simulating half-embedded struts (the distance between the endoluminal and abluminal strut surface: 0.0075 *cm*), and the radius of the vessel lumen 0.15 *cm*. In stage II, the follow-up stage, the strut thickness was reduced to 0.010 *cm* (67%), reflecting a 33% strut bioresorption, and the radius of the lumen was reduced to 0.14975 *cm*. The reduction of strut thickness simulated bioresorption and neointimal hyperplasia, while the reduction of the lumen radius simulated tissue growth inside the vessel wall. Since we were interested in the changes in WSS around the struts, we defined three different strut surfaces: lateral inflow, the surface facing the inflow area; lateral outflow, the surface facing the outflow area; and the endoluminal strut surface, the top surface of the strut (see Figure 3.2).

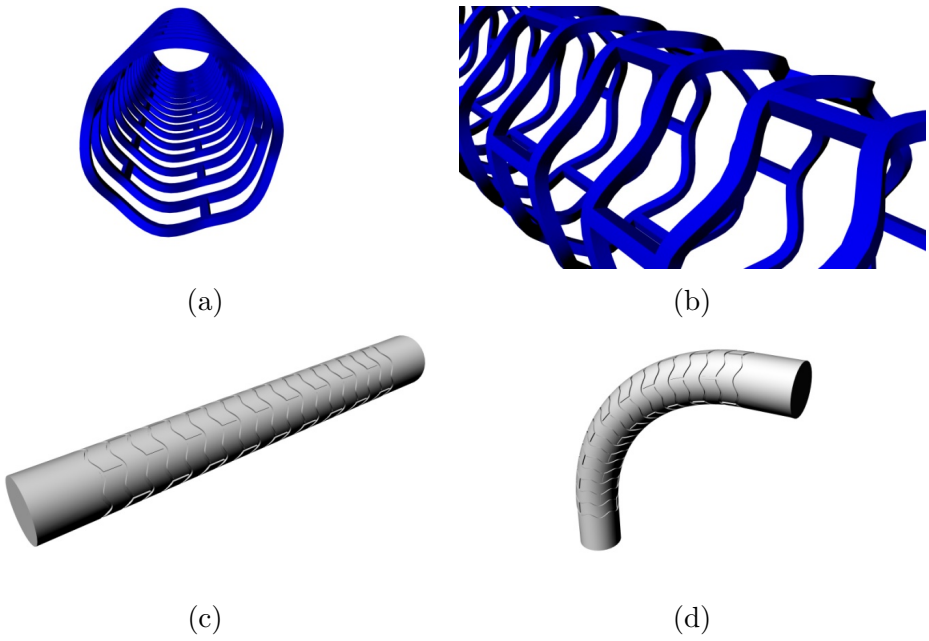

(a) (b)

(c) (d)

Figure 3.3: (a)(b) The idealized geometry constructed based on the Abbott BVS. (c) The CFD domain for the straight vessel model. (d) The CFD domain for the curved vessel model.

### 3.2.2 Meshing of geometry

The geometry volume was discretized as an unstructured mesh of tetrahedral elements using Netgen (Linz, Australia, `http://hpfem.jku.at/netgen/`) and Gmsh (`http://geuz.org/gmsh/`). Since the region of interest was close to the boundaries (wall and struts), we computed a mesh featuring more refined elements (resulting in a more accurate numerical solution) in these regions. Given the complexity of the geometry induced by the stent, the meshing process was split into two steps where the boundary layer with a thickness of 0.025 $cm$ was meshed with an element size of 0.004 $cm$. Then the kernel of the lumen was filled with a coarse element with size 0.012 $cm$ by another mesher software, GMsh. Both mesher software packages employ cutting-edge mesh optimization algorithms.

### 3.2.3 Computational fluid dynamics

The quantities of interest in the CFD domain were the velocity ($cm/s$), pressure ($dynes$), and WSS ($dynes/cm^2$), which can be obtained by solving the Navier-Stokes equation for an incompressible fluid (see equation 2.1 and equation 2.2)

### 3.2.4 Boundary conditions

We assume that the vessel wall $\partial\Omega_0$ is rigid; we prescribe a specific inflow function normal to the inflow section $\partial\Omega_1$ and the "do-nothing" boundary condition to the outflow section $\partial\Omega_1$:

$$\begin{cases} u \cdot n = \dfrac{Q\left(t\right)}{|\partial\Omega_1|},\ u \times n = 0 & \text{on } \partial\Omega_1 \\ u = 0 & \text{on } \partial\Omega_0 \\ pn - v\left(\nabla + t\nabla u^T\right) \cdot n = 0 & \text{on } \partial\Omega_2 \end{cases} \tag{3.1}$$

where $Q$ is a constant inflow rate at 2.7 $cm^3/s$, which is the maximum coronary artery flow rate under normal conditions. The CFD simulations are carried out using LifeV (EPFL, Switcherland; Politecnico di Milano, Italy; INRIA, France; and Emory University, USA).

(a)

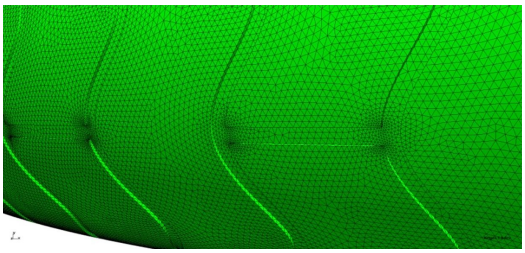

(b)

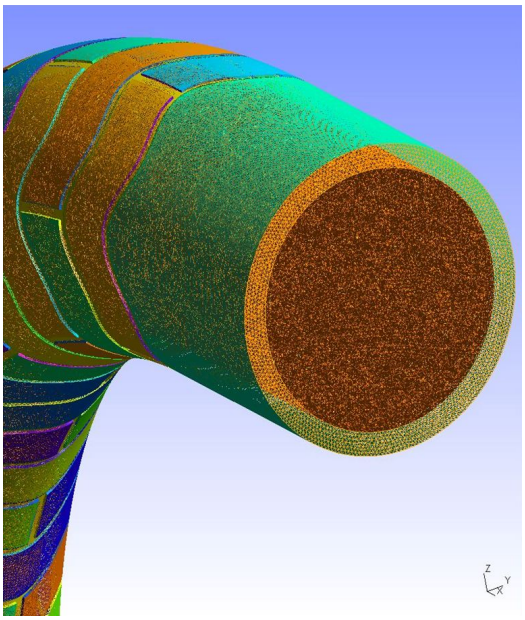

(c)

Figure 3.4: (a) The meshed boundary layer. (b) The fine elements on the boundary layer. (c) The kernel is filled with coarse elements.

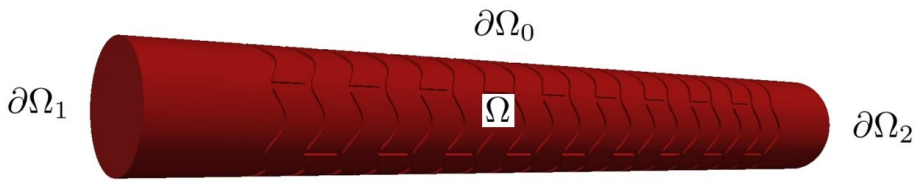


Figure 3.5: The CFD domain

### 3.2.5 Post-processing

After we obtained results for velocity $u$ and pressure $p$, the stress tensor in the fluid could be computed:

$$Tn = \left(v\left(\nabla u + \nabla u^T\right) - pI\right)n. \tag{3.2}$$

The WSS is the component of the stress on the vessel tangential to the vessel wall:

$$S_w = Tn - (Tn \cdot n)\, n, \text{ on } \partial\Omega \tag{3.3}$$

and we visualize the magnitude of WSS, $\|S_w\|$. All quantities of interest ($u$, $p$, and $S_w$) were visualized by Paraview (Kitware, Clifton Park, NY, `http://www.paraview.org`). More importantly, WSS was not only visualized, but also statistically analyzed using Matlab (MathWorks, Natick, MA `http://www.mathworks.com/products/matlab/`) and SPSS (IBM, Armonk, NY, `http://www-01.ibm.com/software/analytics/spss/`).

## 3.3 Results

In this section WSS values are presented as averages. Change (difference) for WSS was estimated as follow-up minus post-procedure (or stage II minus stage I). Percent change was calculated as follow-up-post-procedure/post-procedure $\times$ 100% (or stage II minus stage I/ stage I $\times$ 100%).

The average WSS values following virtual stent deployment (stage I) over the inflow and outflow strut surfaces were 3.2 and 3.1 $dynes/cm^2$, respectively, and 87.5 $dynes/cm^2$ at the endoluminal strut surface. The percent (%) WSS increased from stage I to stage II by 100% and 142% over the inflow

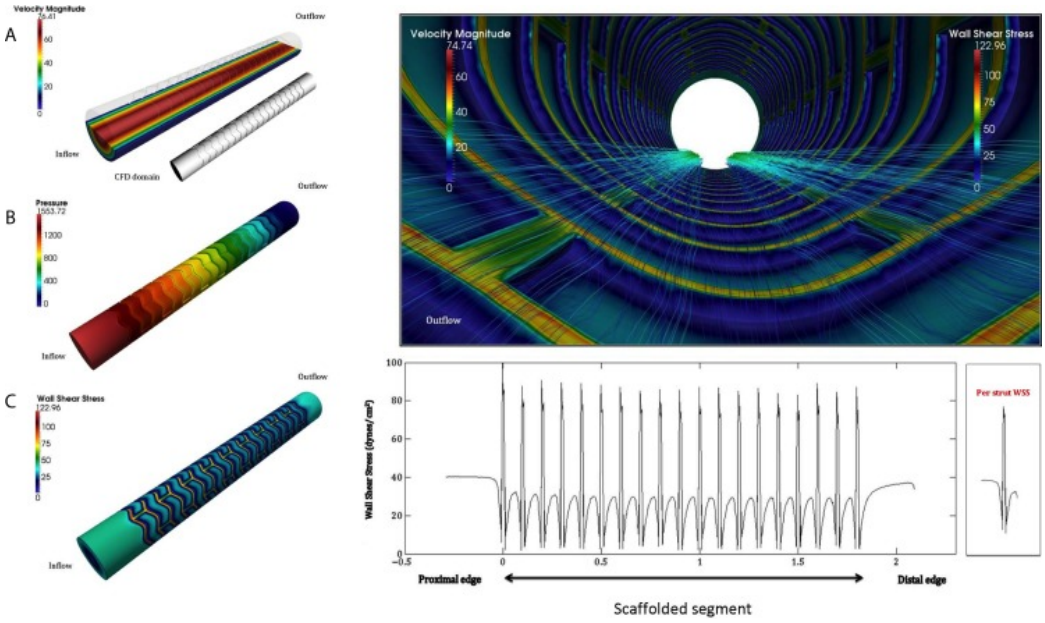


Figure 3.6: Numerical modeling of the virtually deployed bioresorbable scaffold in an idealized straight geometry (post-procedure or stage I). CFD simulations visualizing the velocity streamlines and WSS magnitude on the endoluminal and lateral outflow surfaces of the struts following virtual scaffold deployment. Plot of the quantified WSS vs. axial distance on the endoluminal and both strut sides at stage I. Panels A, B, C: Velocity magnitude, pressure and wall shear stress distribution over the CFD domain.

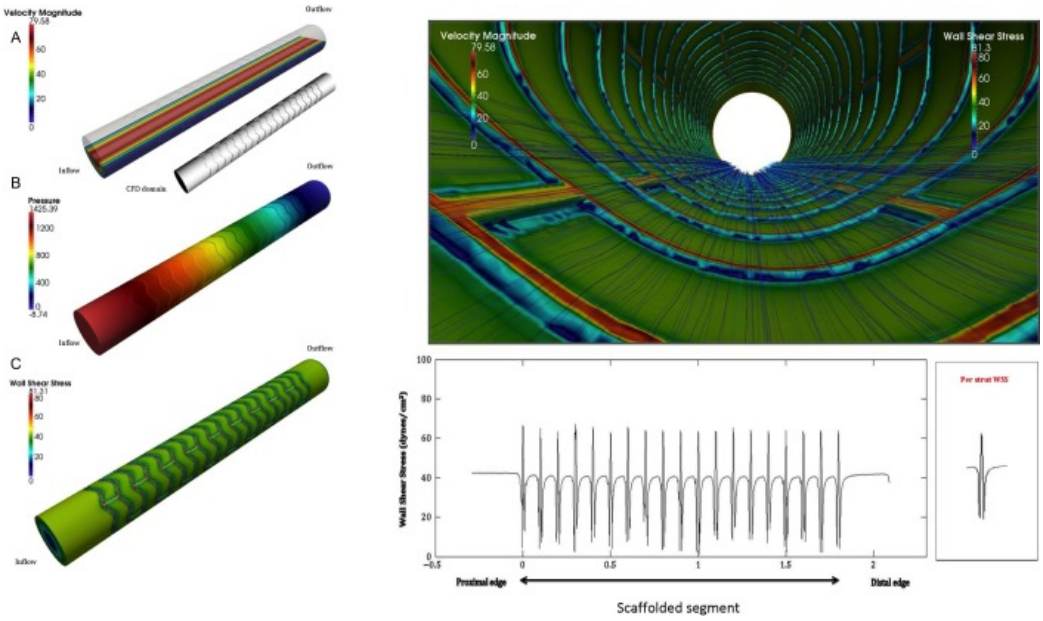


Figure 3.7: Numerical modeling of the virtually applied bioresorption in an idealized straight geometry (follow-up or stage II). CFD simulations visualizing the velocity streamlines and WSS magnitude on the endoluminal and lateral outflow surfaces of the struts following virtually applied bioresorption. Plot of the quantified WSS vs. axial distance on the endoluminal and both strut sides at stage II. Panels A, B, C: Velocity magnitude, pressure and wall shear stress distribution over the CFD domain.

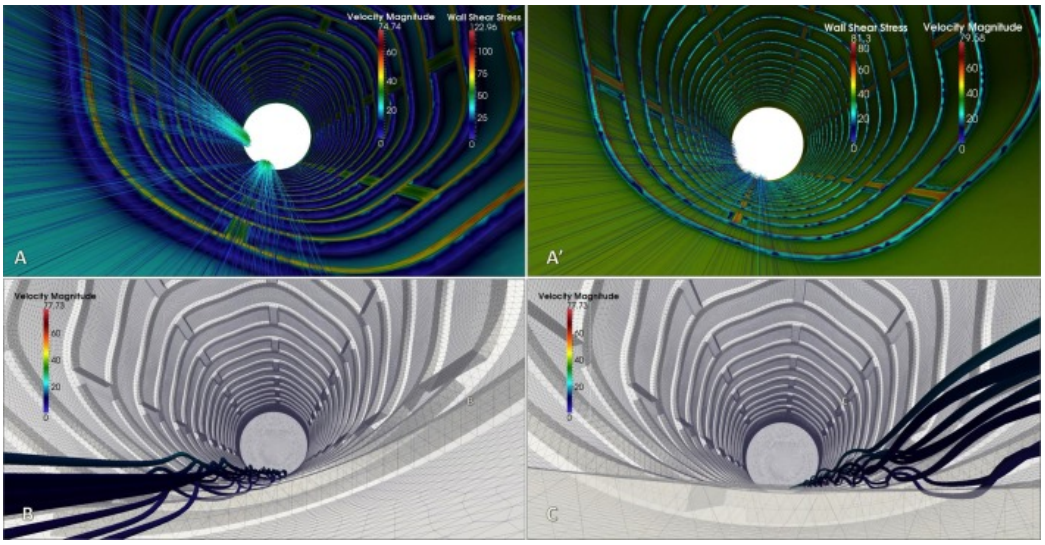


Figure 3.8: Numerical modeling of the simulated stage I (post-procedure) and stage II (virtually applied bioresorption) at the distal edge in an idealized straight geometry. Panels A, A': CFD simulations of the velocity profiles, pressure and WSS at strut 19 (distal edge) Panels B, B': CFD simulations of the velocity magnitudes visualizing the altered flow patterns over the virtually deployed struts.

and outflow surfaces, respectively, and decreased by 27% over the endoluminal surface (Figure 3.9A).

The average WSS values of the inner curvature at stage I over the inflow and outflow strut surfaces were 4.3 and 2.9 $dynes/cm^2$, respectively, and at the endoluminal strut surface was 88.6 $dynes/cm^2$. Similar analysis of the outer curvature demonstrated WSS values of similar magnitude: 5.8, 3.9, and 118.1 $dynes/cm^2$, respectively. The WSS from stage I to stage II at the inner curvature increased by 63% in the inflow and by 66% in the outflow surface and decreased by 20% over the endoluminal surface. Similarly, at the outer curvature the %WSS increased at the inflow and outflow surfaces by 29% and 56%, respectively, and decreased over the endoluminal surface by 28% (Figure 3.9B).

The average WSS value following virtual stent implantation over the inflow surface of the proximal edge did not change significantly; however, over the outflow surface of the proximal edge, it changed significantly: from 2.2 to 12.9 $dynes/cm^2$, amplified by a factor of 4.86. At the distal edge, percentile WSS increased by 59% at the inflow and by 79% over the outflow surface (Figure 3.10).

In curved vessels, the average WSS change of the inflow and outflow strut surfaces of the proximal edge at the inner curvature increased by 79% and 66%, respectively. At the distal edge, a similar analysis showed a decrease by 67% and 3%, respectively (Figure 3.11).

## 3.4 Conclusion and discussion

The present study applied CFD to simulate the biologic behavior of virtually deployed bioresorbable stents. The idealized simulations presented in this chapter supply proof-of-concept of a method that potentially applies clinical translations for further development of bioresorbable platforms. There are several limitations of this analysis which have to be addressed. First, the idealized geometry and the rigidity of the vessel wall are considered major limitations of the current study. Located on the cardiac tissue, coronary arteries undergo movements which potentially introduce significant changes in the fluid dynamics, and such changes deserve specific investigations in the future. In addition, although there is movement induced by the fluid-structure interaction, we believe it should not affect the blood flow significantly. Second, the stent resorption process was assumed to be uniform, while in reality

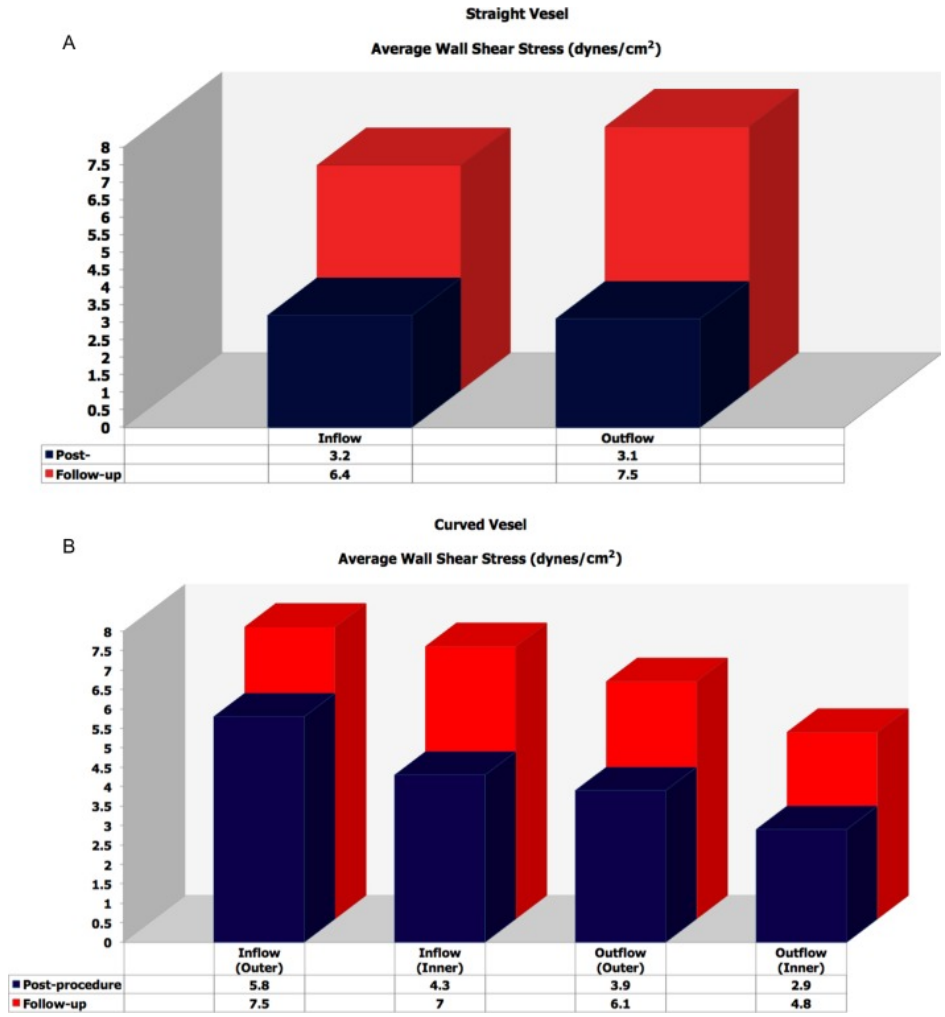


Figure 3.9: WSS quantification over the simulated strut surfaces at stages I and II in (A) straight and (B) curved idealized geometries.

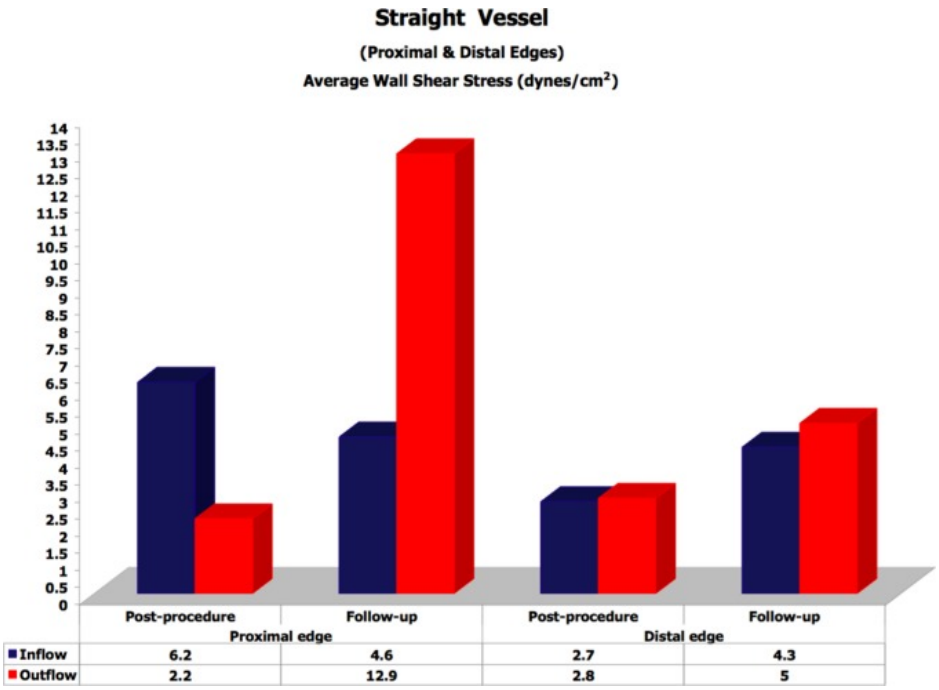


Figure 3.10: WSS quantification over the simulated strut surfaces of the proximal and distal edges at stages I and II in straight idealized geometries.

| Curved Vessel Average WSS (dynes/cm$^2$) | Post- | Follow-Up | Relative Change (%) | Post- | Follow-Up | Relative Change (%) |
|---|---|---|---|---|---|---|
| | *Inner Curvature: Proximal edge* | | | *Inner Curvature: Distal edge* | | |
| Inflow | 7.7 | 13.8 | 79 | 9.0 | 3.0 | − 67 |
| Endoluminal surface | 126.1 | 87 | − 31 | 68.5 | 58 | − 15 |
| Outflow | 5.6 | 9.3 | 66 | 7.9 | 7.7 | − 3 |
| | *Outer Curvature: Proximal edge* | | | *Outer Curvature: Distal edge* | | |
| Inflow | 6.8 | 5.2 | − 24 | 9.3 | 3.4 | − 63 |
| Endoluminal surface | 85.8 | 53.5 | − 38 | 170 | 117.8 | − 31 |
| Outflow | 2.0 | 3.9 | 95 | 2.4 | 4.9 | 104 |

Figure 3.11: WSS quantification over the simulated proximal and distal edges in stages I and II in a curved geometry.

the resorption rate varies in different parts of the stent. Third, the flow conditions in this model were assumed to be steady, and the boundary conditions were not patient-specific. These limitations motivate us to build a pipeline for patient-specific geometrical reconstruction and CFD simulation with prescription of realistic pulsatile inflow function.

# Chapter 4

# Automatic bioresorbable stent strut detection in OCT images

The key to our patient-specific simulations is the stent geometry that we reconstructed from real patients' OCT images. Fortunately, OCT is particularly suitable for BVS because the translucent BVS struts reflect significantly fewer light waves than the surrounding vessel wall [27]. Figure 4.2a includes one frame of an OCT pullback run that we used for the stent reconstruction. The struts appear as small box-shaped boundaries with black cores[38]. Detection of these boxes is the first step of stent reconstruction. Since a large number of patients must be processed in a Computer Aided Clinical Trial framework, the strut detection should be fast and automated as much as possible Therefore, we have developed an automatic BVS strut detection program.

Automatic OCT-image stent detection was also considered by A. Wang et al. and C. Xu et al. [38] [39]. Compared with these two contributions, our approach does not rely on a line-by-line horizontal scan of the raw polar image. Instead, our detection approach is based on an iterative procedure applied directly to the images in a Cartesian framework. The parameters in the detection algorithm can be adjusted to a patient-specific setting. Strut shapes do not necessarily need to be box-like. The detection results are ready to be used with our following stent reconstruction. In this chapter, we illustrate all the procedure developed for the stent detection. In Section 4.1, we describe the detection method in six steps. In Section 4.2, we present the detection results for two OCT image sets (Case 2 and Case 3). In Section 4.3, we draw some conclusions regarding this detection method.

## 4.1 Method

As shown in Figure 4.1, the strut detection program contains six main steps: 1) *Preprocessing* – the image typically contains parts that are not relevant to our purpose of strut detection. We first remove - possibly automatically - those parts. Then a mask is applied to cover the unnecessary OCT parts and extract the region of interest (ROI) for the detection. 2) *Main detection* – the program automatically detects small enclosed white shapes as being the struts. The strut contours and centroids are recorded. 3) *False positive elimination* – false positives are eliminated based on contour length and distance to the inner vessel wall. 4) *Supplementary detection* – we remove the main detection results and then apply a more aggressive detection algorithm. 5) *Final false positive elimination* – additional filters are applied to eliminate the false positives resulting from the supplementary detection. 6) *Correction and patching* – the detection results of each OCT are presented to the operator for correction. Then the program allows the operator to remove any persisting false positives and add any missed struts so that a complete and correct set of strut points can be obtained from each OCT frame.

### 4.1.1 Preprocessing

The OCT images data often contains features unnecessary or even obstructive to strut detection. The OCT pullback runs processed for this study come with a slant vessel diameter ruler in the lumen center, a longitudinal review in the lower image section, and several logos and legends in the corners. The catheter and the protective sheath belong to the original OCT image but are also useless. We should remove these features from the OCT images for better detection efficiency. Because these features' locations are consistently in the shadowy region throughout the pullback run, we can remove them by changing their pixels' color to black, resulting in images such as that which appears in Figure 4.2b.

The struts only reside near the vessel wall area, which has high intensity value. We extract the vessel wall area as $V$ by setting an intensity threshold of 0.7. This choice of threshold is a result of a trial and error empirical approach. To ensure that all struts near the vessel wall can be detected, we expand the extracted vessel wall area $V$ to $V_e$ with a perimeter of 3 pixels, chosen by trial and error; $V_3$ includes the pixels within distance $r = 3$ to any pixel in $V$. This expansion is actualized by the Matlab erosion function

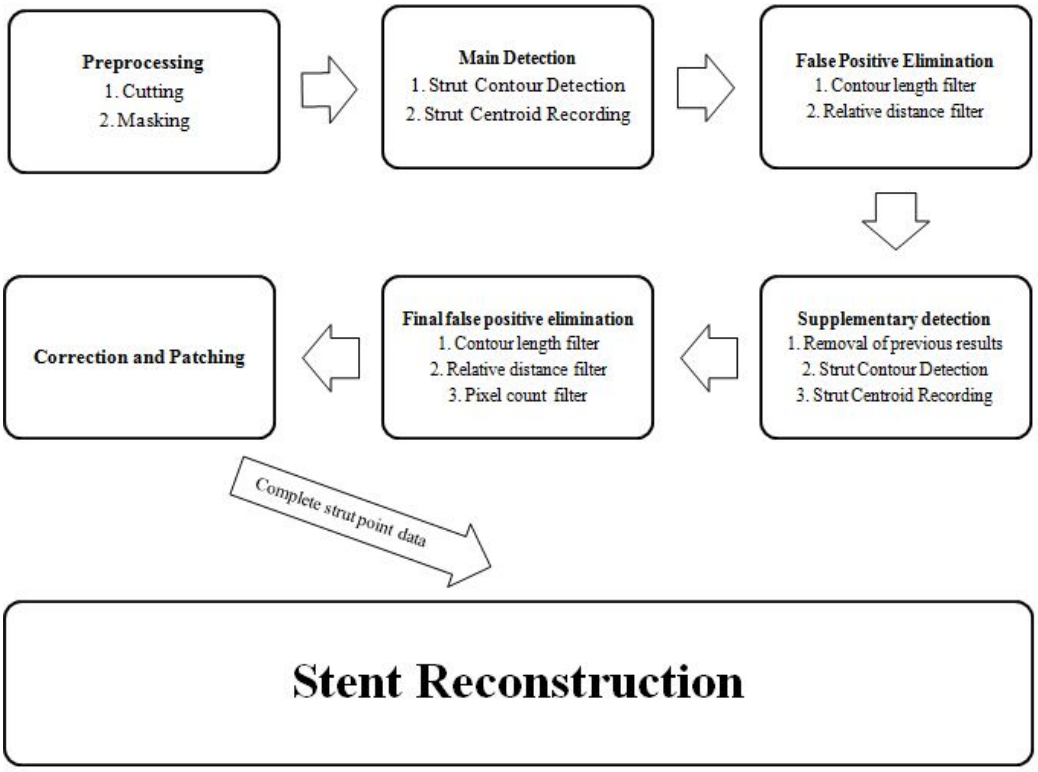


Figure 4.1: The flow chart of the BVS strut detection program.

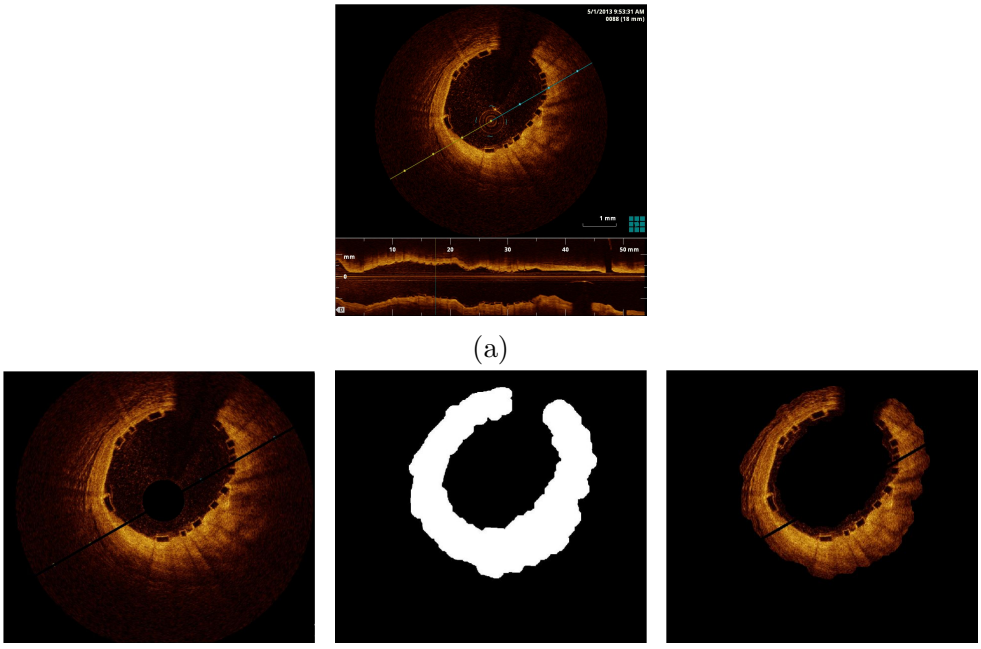

(a)

(b) (c) (d)

Figure 4.2: (a) A baseline OCT image in polar coordinate system. The lower part of the image is the longitudinal review of the stented vessel. (b) The OCT image after the unnecessary features are removed and before the mask is applied. (c) The binary mask for the extraction of ROI. (d) The final ROI for strut detection after the mask is applied.

*imerode* [40]. Then $V_e$ is used to create a binary mask (Figure 4.2c). After applying this mask, the OCT image is reduced to an ROI that only contains the expanded vessel wall area, $V_e$. Figure 4.2d shows the final ROI after the mask is applied. Comparing to Figure 4.2b, Figure 4.2d shows a smaller region for more efficient detection, since much noise outside and inside the vessel wall is eliminated by the mask.

### 4.1.2 Main detection algorithm

The extracted ROI is an RGB image in which each pixel has three intensity value components – $R$, $G$, and $B$ – which are integers ranging from 0 to 255. The ROI is converted to a gray-scale image in which each pixel has only one intensity value component. The intensity value is denoted by $I$ and is formed

by a weighted sum of the $R$, $G$, and $B$ components [41]:

$$I = (0.2989R + 0.5870G + 0.1140B)/255. \tag{4.1}$$

The Gamma Correction is then applied to the image by mapping intensity values from a lower intensity interval, $[a, b]$, to a higher intensity interval, $[c, d]$ [42]:

$$I_{out} = (d - c)(\frac{I_{in} - a}{b - a})^{\gamma} + c. \tag{4.2}$$

The shape of the mapping function can be adjusted by different $\gamma$ values. When $\gamma = 1$, the mapping is linear. This means that the gray level is simply remapped on a different range. By selecting a different value of $\gamma$ we actually warp the gray level. When $\gamma \leq 1$, the function curve is "concaved-up," meaning that the mapping function is weighted toward higher intensity values, sending more dark pixels to a higher intensity value range. By trial and error, we choose:

$$I_{in} = [0, 0.5],\ I_{out} = [0, 1]. \tag{4.3}$$

For main detection $\gamma = 0.6$; for supplementary detection $\gamma = 0.4$. In this way we can perform a more selective thresholding for the strut detection in the supplementary detection, having already filtered out the false positives from the main detection.

After the gamma correction, the gray-scale ROI is converted to a binary image so that the strut edge can be detected. The threshold $t$ for the binary conversion is determined by Otsu's method [43]. This is a method in image processing used to automatically perform clustering-based thresholding. The base algorithm considers two classes of pixels (foreground and background) and computes the optimal threshold separating the two classes so that the variance in each class is minimal. As we will see, correspondingly, the variance between the two clusters is maximized. Here is a brief description of the method in our case:

The intensity values were uniformly divided into $L$ levels: $[1, 2, ..., L]$. The number of pixels at level $i$ is denoted by $n_i$, and the total number of pixels is $N = \sum_{i=1}^{L} n_i$. Thus, the probability that a pixel is in level $i$ is $P(i) = \frac{n_i}{N}$ and the total mean is $\mu_t = \sum_{i=1}^{L} P(i)$. The binary conversion threshold $t$ is chosen from the levels $[1, 2, ..., L]$ to provide the best separation of the two classes: class $C_1$ comprises all pixels in level $[1, 2, ..., t]$, and class $C_2$ comprises all pixels in level $[t + 1, t + 2, ..., L]$, in terms of their class variances.

The individual class variances for $C_1$ and $C_2$ are as follows:

$$\sigma_1^2 \sum_{i=1}^{t} (i - \mu_1(t))^2 \frac{P(i)}{q_1(t)} \tag{4.4}$$

$$\sigma_2^2 \sum_{i=t+1}^{L} (i - \mu_2(t))^2 \frac{P(i)}{q_2(t)} \tag{4.5}$$

where $q_1$ and $q_2$ are the class probabilities given by the following:

$$q_1(t) = \sum_{i=1}^{t} P(i),\ q_2(t) = \sum_{i=t+1}^{L} P(i) \tag{4.6}$$

and $\mu_1(t)$, $\mu_2(t)$ are the classes' means:

$$\mu_1(t) = \sum_{i=1}^{t} \frac{iP(i)}{q_1(t)},\ \mu_2(t) = \sum_{i=t+1}^{L} \frac{iP(i)}{q_2(t)}. \tag{4.7}$$

Then the following discriminating measures are introduced:

$$\sigma_W^2 = q_1\sigma_1^2 + q_2\sigma_2^2 \tag{4.8}$$

$$\sigma_B^2 = q_1(\mu_1 - \mu_T)^2 + q_2(\mu_2 - \mu_T)^2 = q_1q_2(\mu_2 - \mu_1)^2 \tag{4.9}$$

$$\sigma_T^2 = \sum_{i=1}^{L} (1 - \mu_t)^2 P(i) \tag{4.10}$$

are the within-class variance, between-class variance, and total variance of all levels respectively. Notice that

$$\sigma_w^2 + \sigma_B^2 = \sigma_T^2. \tag{4.11}$$

The best class separation occurs when $t$ maximizes the between-class variance. Since the total variance is constant, the within-class variance is minimized when the between-class variance is maximized. Therefore, we run trough all $t$ to find the desired threshold $t^*$ such that:

$$\sigma_B\left(t^*\right) = \min_{1 \le t \le L} \sigma_W^2\left(t\right) = \min_{1 \le t \le L} \left(q_1(t)\sigma_1^2(t) + q_2(t)\sigma_2^2(t)\right). \tag{4.12}$$

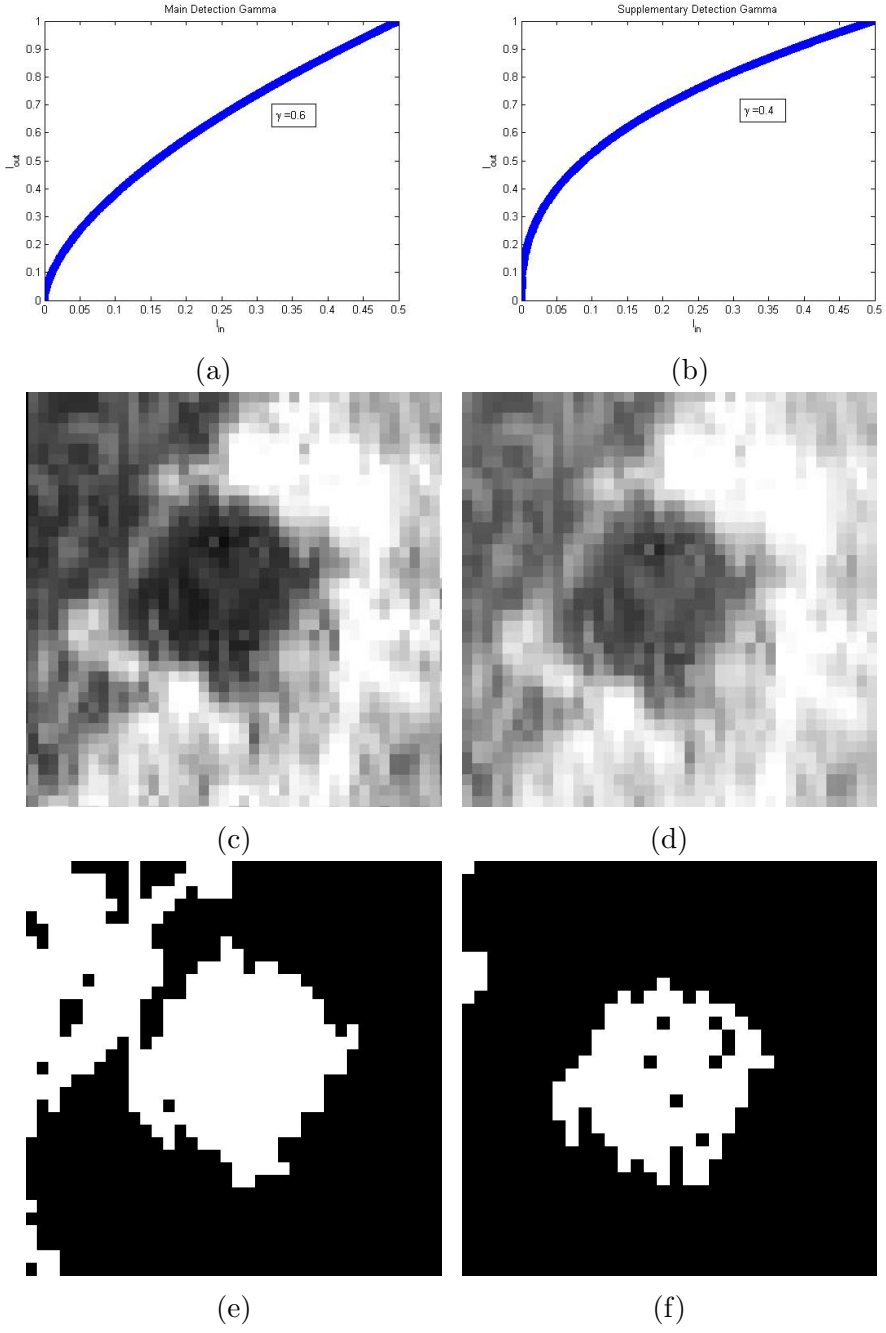


Figure 4.3: (a) Gamma correction function curve with $\gamma = 0.6$. (b) Gamma correction function curve with $\gamma = 0.4$. (c) The gray-scale image of a strut after $\gamma = 0.6$ is applied. (d) The gray-scale image of the strut after $\gamma = 0.4$ is applied. (e) Binary image of the strut using $\gamma = 0.6$. This strut is missed by the main detection since the white area is not fully closed. (f) Binary image of the strut using $\gamma = 0.4$. After the stronger gamma correction, the strut is now detected since the strut box appears as a closed white area.

Pixels with an intensity value lower than $t^*$ become 0-pixels while those with an intensity value higher than $t^*$ become 1-pixel. At this point, the strut cores are entirely black, and the strut edges are white.

Then the image is 0-1 inverted so that the struts appear as small white boxes surrounded by black pixels (Figure 4.4a). A recursive flood-fill algorithm is applied to detect all regions formed by the connected white pixels. The flood-fill algorithm implementation is described in the following:

**Algorithm 1** Flood-fill algorithm

```
1: Initialize Empty White-area
2: function Flood-fill(Binary-Image, pixel(x, y, White-area))
3: if pixel (x, y) is black then return
4: if pixel (x, y) is white then, save pixel (x, y) to White-area
5:     recursive perform Flood-fill in 8-connectivity neighborhood of
   pixel(x,y)
6:     Flood-Fill(Binary-Image, pixel(x, y+1,));
7:     Flood-Fill(Binary-Image, pixel(x+1, y+1));
8:     Flood-Fill(Binary-Image, pixel(x+1, y,));
9:     Flood-Fill(Binary-Image, pixel(x+1, y-1));
10:    Flood-Fill(Binary-Image, pixel(x, y-1,));
11:    Flood-Fill(Binary-Image, pixel(x-1, y-1));
12:    Flood-Fill(Binary-Image, pixel(x-1, y));
13:    Flood-Fill(Binary-Image, pixel(x-1, y+1)); return
```

Regardless of their size, any enclosed white regions will be recognized as stent struts by the detection algorithm. Small white regions with less than 50 pixels are discarded because struts should have at least 300 pixels in baseline (see Figure 4.4b). The remaining white regions are considered candidate struts, and their borders are recorded as candidate strut edges. These candidate strut edges are always closed, so we refer to them as "candidate strut contours." These contours' centroids are computed and recorded (Figure 4.4c) for our 3D stent reconstruction, which will be discussed in Chapter 5.

### 4.1.3 Elimination of false positives

Two filters are consecutively applied to eliminate the false positive struts obtained during the main detection.

(a) (b) (c)

Figure 4.4: (a) Binary OCT image before noise reduction. (b) Binary OCT image after noise reduction. White regions with area smaller than 50 pixels have been discarded. (c) A detected strut. Green line is the strut contour; white point is the strut centroid.

**Contour length filter:** The strut thickness is 150 $\mu m$ in baseline, which is the length of 20 OCT-image pixels. Therefore a strut box should be about 80 pixels long. A candidate strut contour longer than 200 pixels or shorter than 40 is a false positive and is eliminated from the results (see Figure 4.5a).

**Wall distance filter:** In baseline, the struts are usually aligned with the lumen boundary. Therefore, most struts should be near the lumen contour, which is the inner vessel wall on the OCT image (the white line in Figure 4.5b). We can filter out false positives based on their relative distance to the lumen contour. The strut candidate centroid and the catheter center are used to determine a straight line, which always intersects the lumen contour. The distance between the centroid and the intersection point is measured as being the candidate's relative distance to the lumen. If this distance is greater than 40 pixels, the strut candidate will be eliminated as a false positive (Figure 4.5b).

### 4.1.4 Supplementary detection

We take an iterative approach to detect more struts by applying a supplementary detection which is more aggressive than the main detection. To avoid redundancy, all main detection results are removed from the ROI before the supplementary detection process begins. We fill the detected contours with white pixels, so after the inversion these areas will be black and thus impos-

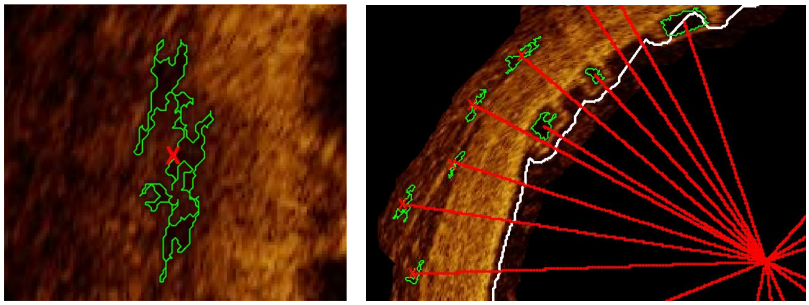

(a) (b)

Figure 4.5: (a) A strut eliminated by the Contour length filter. (b) Several struts eliminated by the Wall distance filter.

sible to be re-detected.

After the detected struts are filled or "whited out," we apply Gamma correction with a lower $\gamma$ value in order to recognize lower intensity pixels as strut contours. With a new gamma value of 0.4, even blurred strut edges can be detected.

### 4.1.5 Final elimination of false positives

More false positives emerged during the supplementary detection. Most of them can be eliminated right away after we apply the Contour length filter and the Wall distance filter again. However, a minute number of false positives can pass both filters. As shown in Figure 4.6b, such false positives persist because they neither have long contours nor are far from the vessel wall.

It should be noted that such false positives are usually located inside the lumen contour. Thanks to their unique positions, these false positives can be eliminated by another filter that we describe hereafter.

**Pixel count filter:** For every strut contour candidate, we extend a square region of 100 $\times$ 100 pixels in size from the centroid toward the lumen center, and then the number of bright pixels in this square is counted. If a candidate is a stent strut, the square will inevitably cover one of the strut's edges. The strut edges appear as bright pixels, so the white pixel count will be high. However, because the false positives do not have bright strut edges, their squares should not contain many bright pixels. This filter has an intensity value threshold of 0.7 and a pixel-count threshold of 10. A strut

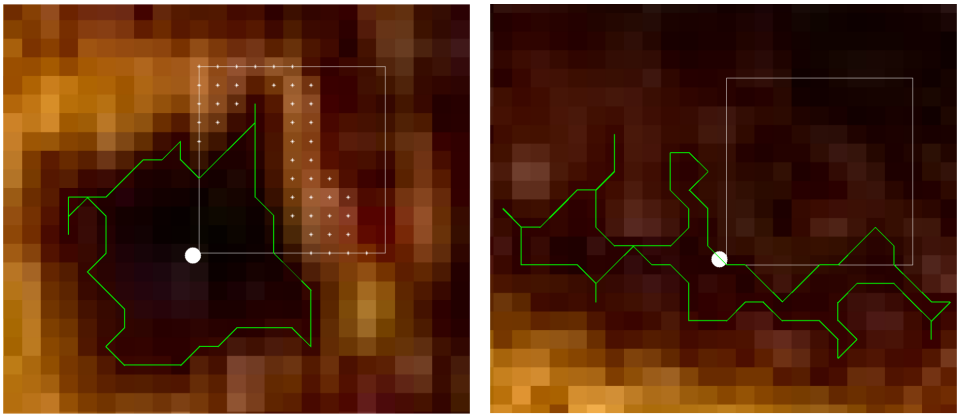

(a) (b)

Figure 4.6: (a) A strut that passed the Pixel counter filter with 44 high intensity pixels in the scan square. (b) A strut eliminated by the Pixel counter filter. The scan square contain no pixel with high intensity value.

candidate whose square contains fewer than 10 pixels with intensity values higher than 0.7 is filtered out as a false positive.

### 4.1.6 Patching and correction

After two detection rounds, usually more than 80% of the struts are already detected. Such results are sufficient for a stent-deployment assessment. However, for our 3D stent reconstruction goal, all strut centroids should be recorded. Therefore, we incorporate a manual correction/patching feature to complete the detection program.

This correction/patching feature will first allow the operator to remove any persisting false positive and then add any missed struts to the final results. After the automatic detection and filtration, the results will be presented with the OCT in the background. In rare cases, a false positive can persist through all three filters. The operator can remove such persisting false positives by simply clicking on them with the mouse cursor. More importantly, the operator can also use the cursor to record any missed struts' centroids. Then the centroids of the missed struts are recorded and the local images of the missed struts are simultaneously saved in a data bank (see Figure 4.7). These struts usually contain incomplete edges and thus are not recognized by the automatic detection. We believe this data bank of missed

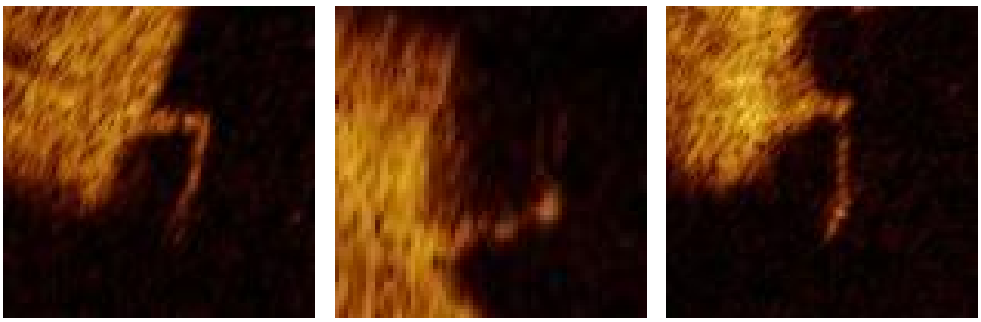

(a) (b) (c)

Figure 4.7: Three local image of persisting false positives saved in the data bank for future analysis. Most of persisting false positives have incomplete edges due to the catheter shadow, thus a closed strut contour can not be detected.

strut images will be useful in future studies.

## 4.2 Results and validation

Case 2 and Case 3 OCT pullback runs were processed using this strut detection program (Case 1 strut detection had been completed manually before the automatic detection program was created). The results are shown in Chart 4.9. In this chart, the number of correctly detected struts is equal to the number of automatically detected struts minus the number of persisting false positives. The number of persisting false positives is down to double digits and is usually concentrated in an marginal number of OCT frames. Furthermore, in most frames, all struts can be accurately detected automatically (Figure 4.8). The total number of struts after patching is considered to be the 100% correct detection results. The detection program can automatically detect more than 80% of all struts, and the detection accuracy in Chart 4.9 is defined as the number of correctly detected struts over the total number of struts after patching.

Using the program's correction/patch feature, the operator removes all persisting false positives and patches any missed strut point in the results, ensuring a complete and accurate 3D strut point cloud (see Figure 4.10a) in which the points obtained by main detection, supplementary detection, and

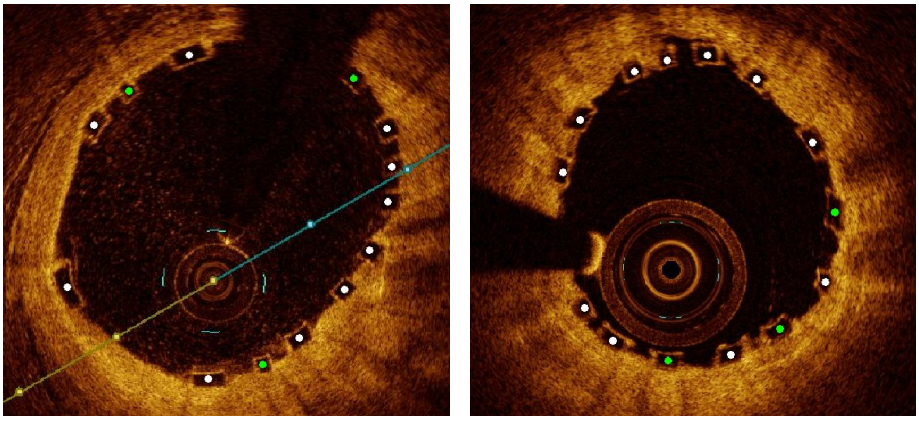

(a) (b)

Figure 4.8: Detection results from 2 OCT slices. White points are strut centroid detected by the main detection; green points are strut centroids detected by the supplementary detection.

manual patching are displayed in different colors.

The strut detection program can be visually validated by the quality of reconstructed 3D stent geometry as shown in Figure 4.10b. We can see that the stent struts match the strut positions in the OCT images. The method that constructs the stent geometry from the point cloud is discussed in detail in Chapter 5.

## 4.3 Conclusion

An automated or semi-automated BVS strut detection method is crucial for using computational tools on a large number of patients. Since the struts are detected from real patient OCT images, the subsequently constructed stent geometry reflects the stent's true disposition information. When used in CFD simulations, such geometry can propagate the quantitative analysis for clinical research on the use of BVS systems in interventional cardiology. In this chapter, we have introduced a strut detection program which uses an iterative "detect-then-filter" algorithm to automatically find and record the struts and their centroids. For now, we can state that the algorithm is accurate for clinical purposes. We have successfully used the strut point cloud to reconstruct the 3D stent geometry, which validates the detection

| **Pullback Run** | **Case 2** | **Case 3** |
|---|---|---|
| Number of slices | 100 | 63 |
| Number of automatically detected struts | 783 | 602 |
| Number of persisting false positives | 18 | 34 |
| Number of slices affected by persisting false positives | 9 | 7 |
| Number of correctly detected struts | 765 | 568 |
| Number of manually patched struts | 180 | 101 |
| Total number of struts after patching | 945 | 669 |
| Detection Accuracy | 81% | 85% |

Figure 4.9: Strut Detection Results

and this program's usefulness. As for future development, we believe the system will be improved to a better automation level. In particular, in the follow-up of the present work we will create machine learning algorithms that will analyze the missed struts. In this respect, the data bank of missed strut images we have created may become a database for training the algorithms in order to further improve the program's overall accuracy.

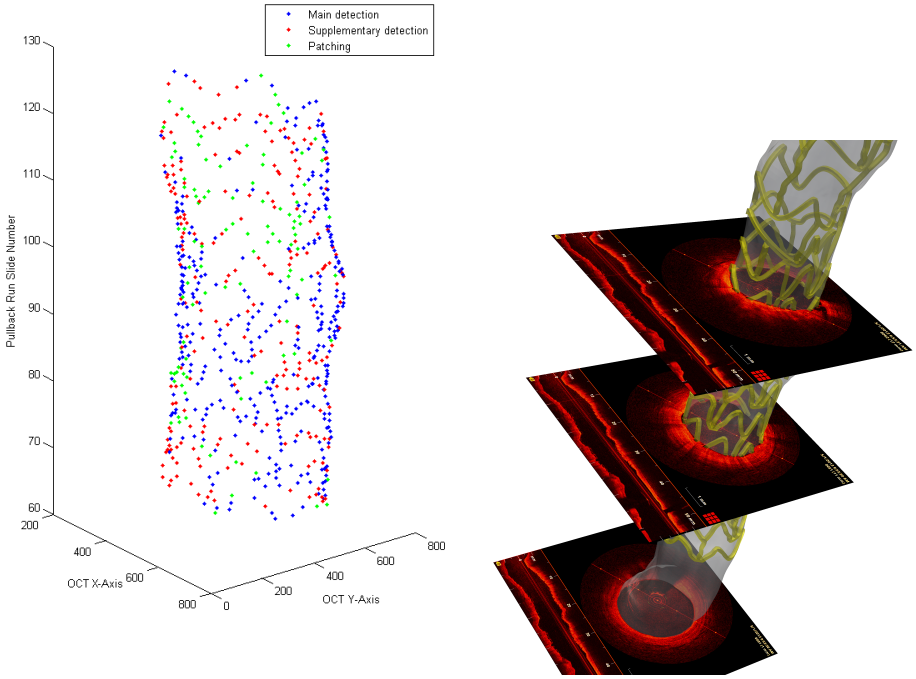


(a) (b)

Figure 4.10: (a) Complete 3D strut point cloud. (b) Reconstructed 3D stent geometry from the 3D point cloud matches the OCT pullback run.

# Chapter 5

# Geometrical reconstruction of implanted bioresorbable stent

After the struts are detected from the images, we need a method to reconstruct the 3D structure of the stent deployed in a patient's coronary artery. This is a nontrivial procedure in which we stack the data points retrieved at the previous step and then properly connect them to have a surface representation of the 3D stent structure. The 3D stent structure is obtained by first extracting a wire-frame of the strut point cloud and then by expanding the skeleton to a 3D surface structure. In this chapter, we detail how we implemented these steps and performed the testing.

## 5.1 3D Strut-point cloud formation

The strut points we detected from the OCT images are saved in 3D space, $(P_1, P_2, N)$, where $P_1$ and $P_2$ are the horizontal and vertical pixel coordinates of the strut center location, and $N$ is the OCT frame number. Table 1 shows results of OCT frame 88, Case 2. After all OCT frames are processed, we then transform the results to the actual physical scale, $(X, Y, Z)$, by using the OCT calibration factor (110 $pixels/mm$) and pullback speed (5 $frames/mm$):

$$\begin{cases} X = P_1/110 & (5.1) \\ Y = P_2/110 & (5.2) \\ Z = N/5 & (5.3) \end{cases}$$

| $P_1$ | $P_2$ | $N$ |
|---|---|---|
| 641 | 223 | 88 |
| 675 | 241 | 88 |
| 677 | 261 | 88 |
| 675 | 320 | 88 |
| 656 | 374 | 88 |
| 643 | 400 | 88 |
| 625 | 478 | 88 |
| 593 | 497 | 88 |
| 552 | 504 | 88 |
| 391 | 428 | 88 |
| 386 | 283 | 88 |
| 399 | 256 | 88 |
| 423 | 229 | 88 |

(a)

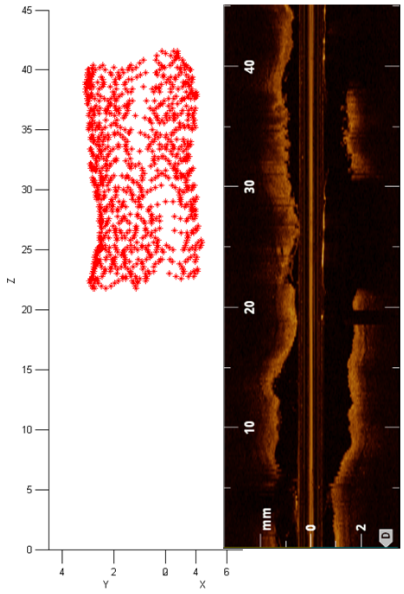


(b)

Figure 5.1: (a) The results of strut detection for an OCT slice. (b) The 3D strut point cloud aligned with the OCT longitudinal review.

The OCT calibration factor varies but it is accessible from each OCT file header. The result is the 3D strut point cloud, which aligns with the longitudinal OCT image review (Figure 5.1b). The 3D point cloud presents some stent pattern and will thus be used to extract the stent wire-frame.

## 5.2 Connectivity recovery

The 3D strut point cloud will be used to identify the specific connectivity pattern between each detected strut point. In this section, we illustrate the process to recover this connectivity, leading to the stent skeleton creation.

### 5.2.1 2D projection

We aim to create an automated approach that recovers 3D point cloud connectivity by exploiting the knowledge of the original stent design. Figure 5.2

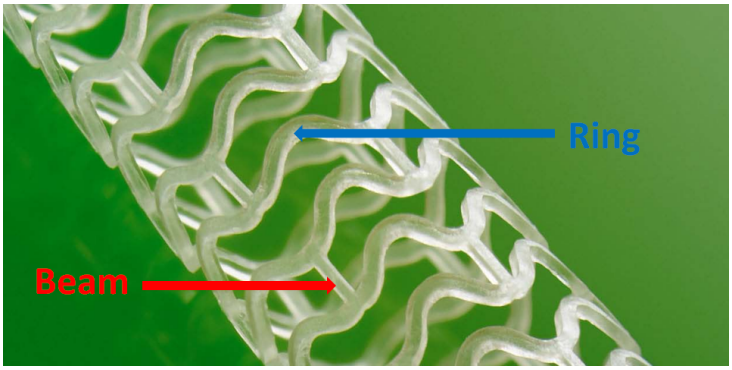


Figure 5.2: Abbott ABSORB BVS before deployment

shows an Abbott ABSORB stent geometry before its deployment. In this specific stent object within the study, two distinct elements can be recognized, namely the following: 1) "Ring" structures - closed ring-like patterns noted by the blue arrow. 2) "Beam" structures - short straight patterns that connect two rings. The definition of "ring" structure and "beam" structure are first introduced in Section 1.3 of this thesis.

A first fundamental observation is that these two patterns, evident in the 3D model, can also be identified in the 3D strut point cloud as shown in Figure 5.3c. A second key aspect is that the patterns are even more evident when the strut point cloud undergoes a change of coordinates in which the cylindrical 3D point cloud structure is flattened into a 2D space (Figure 5.3d).

The procedure to flatten or "unroll" the 3D point cloud to a 2D space is inspired by the mapping between a cylinder and a rectangle. If all the strut points are close enough to be co-planar to a cylindrical surface, then the following method would suffice:

**The unrolling method:** We store the 3D coordinates of the stent point cloud in a $N_p \times 3$ matrix $M = [X, Y, Z]$, in which each column corresponds to a Cartesian axis and $N_p$ represents the number of points. After we compute the center of mass of the struts locations (identified by the point $(X_{mean}, Y_{mean}, Z_{mean})$, we use this point as the center and pass it to cylindrical coordinates:

$$[X_{sh}, Y_{sh}, Z_{sh}] = [X - X_{mean}, Y - Y_{mean}, Z - Z_{mean}] \tag{5.4}$$

$$r = \sqrt{X_{sh}^2 + Y_{sh}^2} \tag{5.5}$$

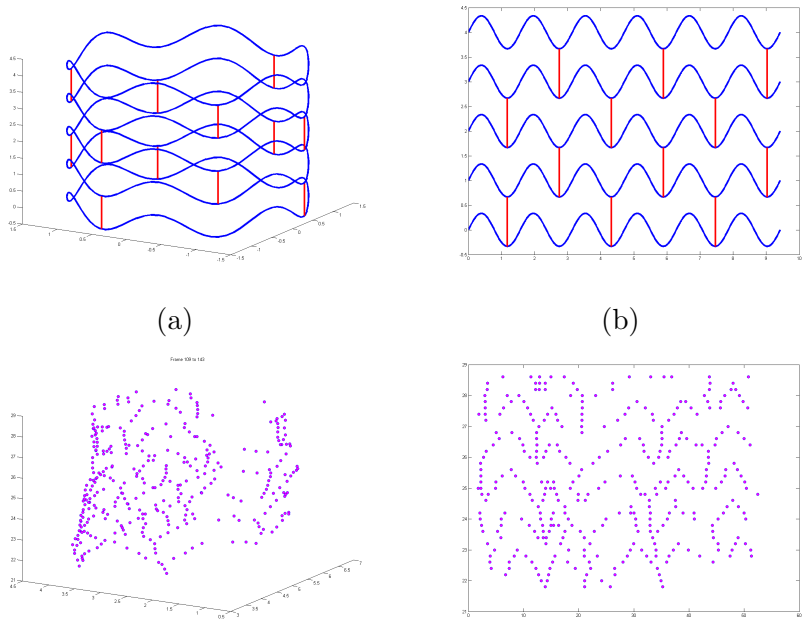

(a) (b)

(c) (d)

Figure 5.3: (a) 3D stent pattern. (b) 2D stent pattern after unrolling the cylindrical stent pattern. (c) 3D strut point cloud. (d) 2D strut point cloud.

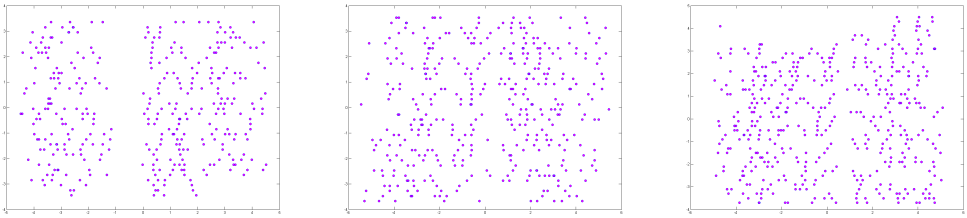

(a) (b) (c)

Figure 5.4: 2D point cloud obtained by the unrolling method.

$$\theta = \arctan(\frac{Y_{sh}}{X_{sh}}) \tag{5.6}$$

Then we create the horizontal axis $d_u$ for the 2D point cloud, which is the element-wise product of $r$ and $\theta$:

$$d_u = r \circ \theta \tag{5.7}$$

The 2D point cloud is created by plotting $Z_{sh}$ against $d_u$. The entire 3D point cloud can be opened in about three sections (Figure 5.4).

This approach is ideal if the 3D point cloud aligns closely to a cylinder because we use the fixed center of mass as the center to compute the polar coordinates, $r$ and $\theta$. In most OCT pullback runs, each OCT slice's center varies dramatically, which is why the results show unrecognizable patterns in some regions.

A better 2D point cloud can be generated with a different approach, which instead sorts all points by their $\theta$ coordinate and then generates the horizontal axis based on the distance between each pair of consecutive points:

**The relative distance method:** Vectors $r$ and $\theta$ are included in the shifted coordinates' matrix:

$$M = [X_{sh}, Y_{sh}, Z_{sh}, r, \theta]. \tag{5.8}$$

We then sort matrix M by column $\theta$ to obtain $M_{sor}$:

$$M_{sor} = [X_{sor}, Y_{sor}, Z_{sor}, r_{sor}, \theta_{sor}]. \tag{5.9}$$

The horizontal axis, $d_p$, is created by incrementally adding the relative distance between two consecutive points:

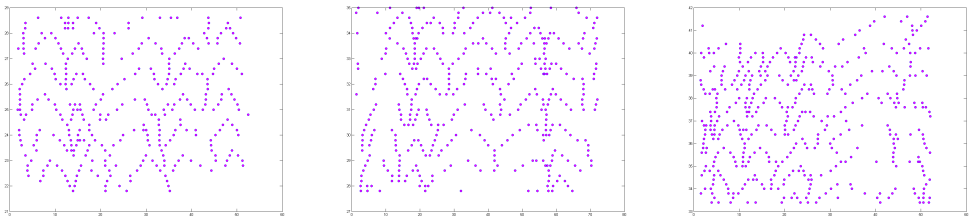

(a) (b) (c)

Figure 5.5: 2D point cloud obtained by the relative distance method.

$$d(1) = ||X_{sor}(1), Y_{sor}(1)||, \tag{5.10}$$

$$d(i) = \sum_{1}^{i} \| \left(X_{sor}(i), Y_{sor}(i)\right) - \left(X_{sor}(i-1), Y_{sor}(i-1)\right) \| \text{ for } 2 \leq i \leq n. \tag{5.11}$$

The 2D point cloud is generated by plotting $Z_{sor}$ against $d_p$ as shown in Figure 5.5.

Comparing the two methods' results shows that the relative distance method yields a better 2D point cloud. The unrolling method sorts the points along the $\theta$ with the mass center as the coordinate center, while the relative distance method sorts the point by tracking their relative distances. The plots in Figure 5.5 consistently provides recognizable 2D patterns because the relative distance method does not rely on a fixed center.

Later in the reconstruction, we will have to match all 2D points back to the original 3D point cloud, so we order both the 3D and 2D point clouds by $Z_{sor}$:

$$M_{3D} = [X_{sor}, Y_{sor}, Z_{sor}], \tag{5.12}$$

$$M_{2D} = [d_p, Z_{sor}]. \tag{5.13}$$

The $i$th row of $M_{2D}$ corresponds to the 3D point in the $i$th row of $M_{3D}$.

### 5.2.2 Interactive pattern interpretation in 2D

Ideally, the classification of points based on the two possible substructures - ring or beam - should be done automatically. Due to distortion in the stent deployment, it is, however, quite hard to create a completely automated system; the automatic identification of rings and beams may always be subject to some errors. For this reason, at this stage we prefer to stick to a manual pattern interpretation process, as we describe in the present section.

The 2D point clouds are then categorized into rings and beams by an interpretive drawing process. First, two transparent layers, "1" and "2," are created on top of the 2D point cloud. On layer 1, the operator draws lines to cover the strut points that are likely to appear on the rings. On layer 2, the operator draws lines to cover the strut points that are likely to appear on the beams (Figure 5.7a and 5.7b). Then the two layers are converted into the following matrices: $R_{pixels}$ and $B_{pixels}$. For example, $R_{pixel}$ will have a row entry of $(m_1, n_1)$ if the pixel $(m_1, n_1)$ is painted by the operator as a ring pixel. Afterwards, the algorithm separates pixels stored in $R_{pixels}$ and $B_{pixel}$ into different ring and beam pixel groups and then labels them accordingly (Figure 5.7c and 5.7d).

Preferably, the operator will draw each ring and beam line continuously. If there are no breaks in these lines, the pixels covered by each line will be connected; therefore, we can separate the ring and beam pattern drawings into different ring and beam pixel groups by the flood-fill algorithm described in Section 4.1 (see Algorithm 1) . It is important to note that beam lines are short while ring lines are rather long. Requiring the operator to always draw each ring continuously (with only one stroke) makes the drawing process a burdensome task, however, we aim to make the stent reconstruction as automatic as possible. Being the only manual step in the reconstruction process, this drawing process should be made easy for the operator. Therefore, we implemented a more robust separating algorithm that does not require each ring line to be drawn continuously. The operator can draw each ring with several strokes, which can then be automatically grouped into one unified ring line while different ring lines will still be separated:

First, pairwise distance between all pixels in the ring pattern are computed:

$$d_{i,j} = \|p_i, p_j\|. \tag{5.14}$$

The linkage function takes the distance information and then links pairs of nearby points into binary clusters (each initial cluster comprises only two

points). These newly-formed clusters are then linked to each other and also to other points in order to create bigger clusters until all the points in the original data set are linked in a hierarchical tree [44]. The distance between two clusters is measured by the minimum distance, which is as follows:

$$\min \{ d(i,j) : p_i \in A,\, p_j \in B \} \tag{5.15}$$

Multiple strokes of the same ring line are usually very close to each other as shown in Figure 5.6. The distance between two clusters is categorized by the minimum distance. Because the distance between two strokes of the same ring line is smaller than the distance between two ring lines, we set a cutoff point, $d_{cut}$, so that strokes with the minimum distance – less than $d_{cut}$ – will be grouped as one ring line:

$$d_{inner-ring} < d_{cut} < d_{inter-ring}. \tag{5.16}$$

Through experimentation, we found that $d_{cut} = 0.3$ works for all drawings. In this way, the operator need neither to draw a long ring continuously nor to specific which ring or beam she or he is drawing. Using this method, each ring line will be separated as one cluster despite having multiple strokes.

After the automatic separation process, each ring and beam line is in its own pixel group as shown in Figure 5.7c and Figure 5.7d. The blue line in Figure 5.8a represents the painted pixel group for ring 4. Any strut point in the 2D point cloud that has distance of less than $\tau$ to any point of this pixel group will be categorized as ring 4 strut points. The results are shown in Figure 5.8e: the points in blue boxes have been separated from the 2D point cloud as ring 4 strut points based on their distance from the ring 4 pixel group.

### 5.2.3 3D categorization

After all the 2D strut points are categorized, we map all 2D strut points back to 3D. The $i$th point in $M_{2D}$ corresponds to the $i$th point in $M_{3D}$ since the points in the $M_{2D}$ and $M_{3D}$ were kept in the exact same order.

We plot the categorized the 3D point cloud in Figure 5.9 for a simple verification. In this Figure, the ring and beam points are sorted and connected by straight lines (we will use the proper spline for geometry reconstruction in Section 5.3. As shown in Figure 5.9, the 3D point cloud has been put into a wire-frame in which all 3D strut points are categorized into rings and beams. Thus, we have recovered the 3D strut point cloud connectivity.

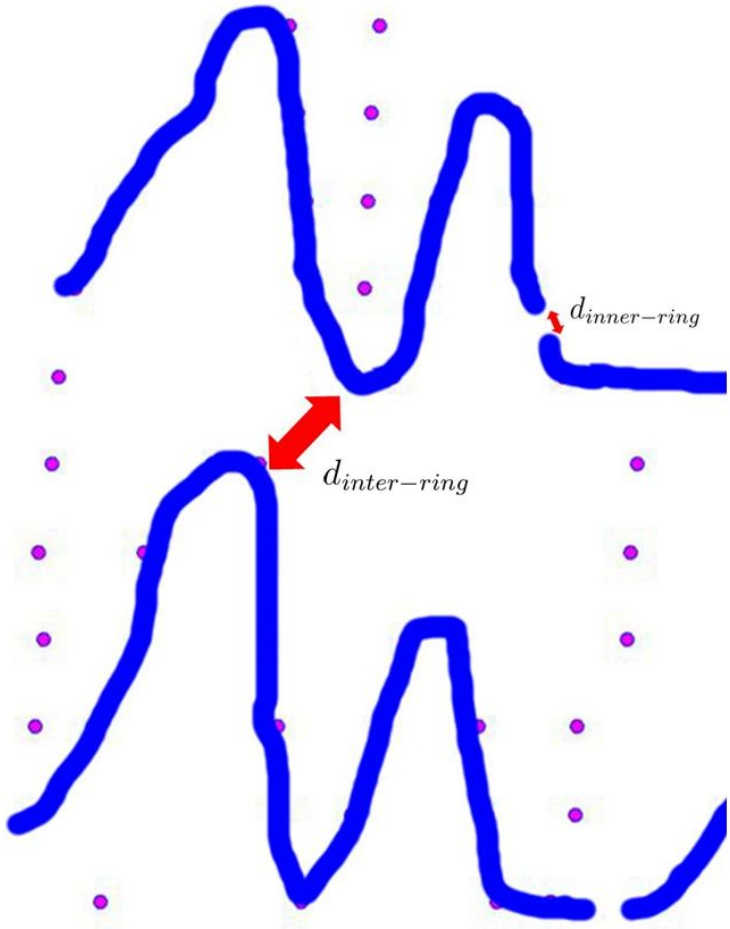


Figure 5.6: Multiple strokes of the same ring line can be grouped together by the cutoff $d_{cut}$, which satieties $d_{inner-ring} < d_{cut} < d_{inter-ring}$.

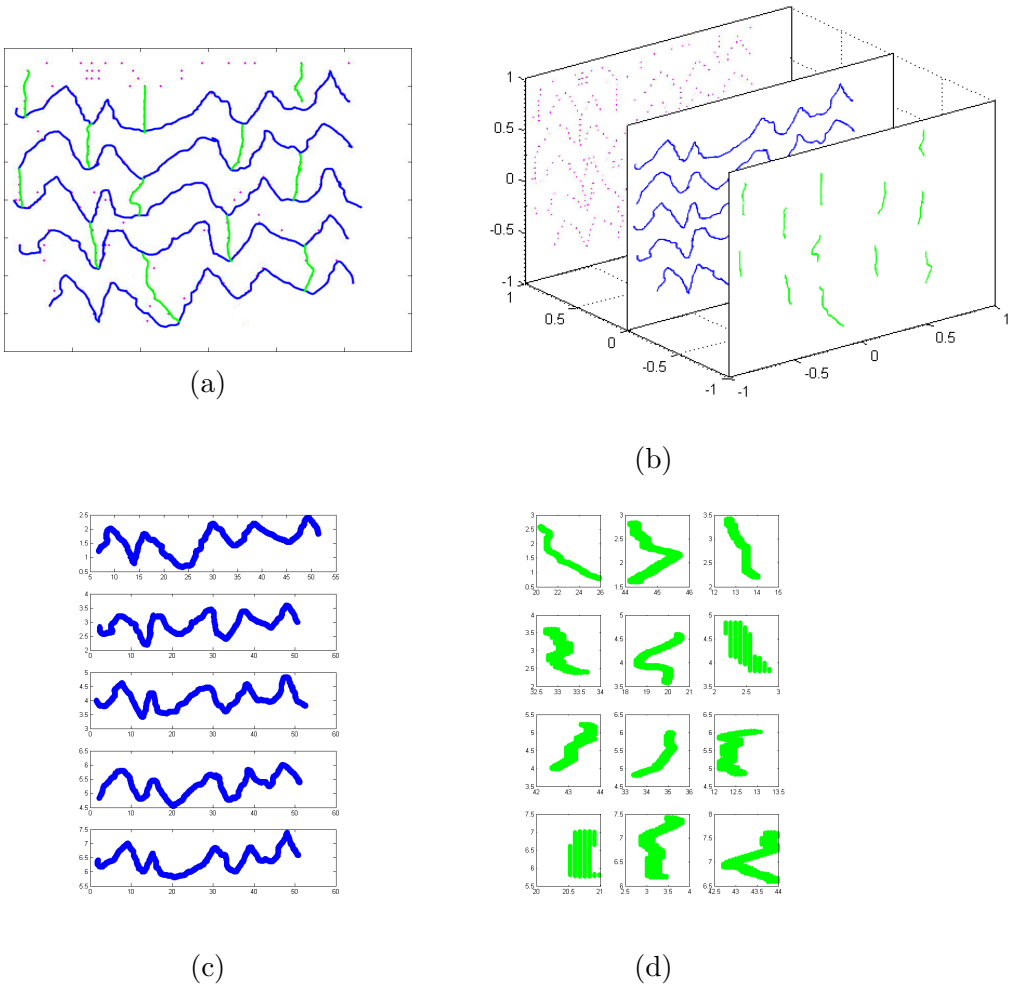

(a)

(b)

(c)

(d)

Figure 5.7: (a) Interpretive drawings. (b) Interpretive drawing in 2 layers. (c) Separated ring pixel groups. (d) Separated beam pixel groups.

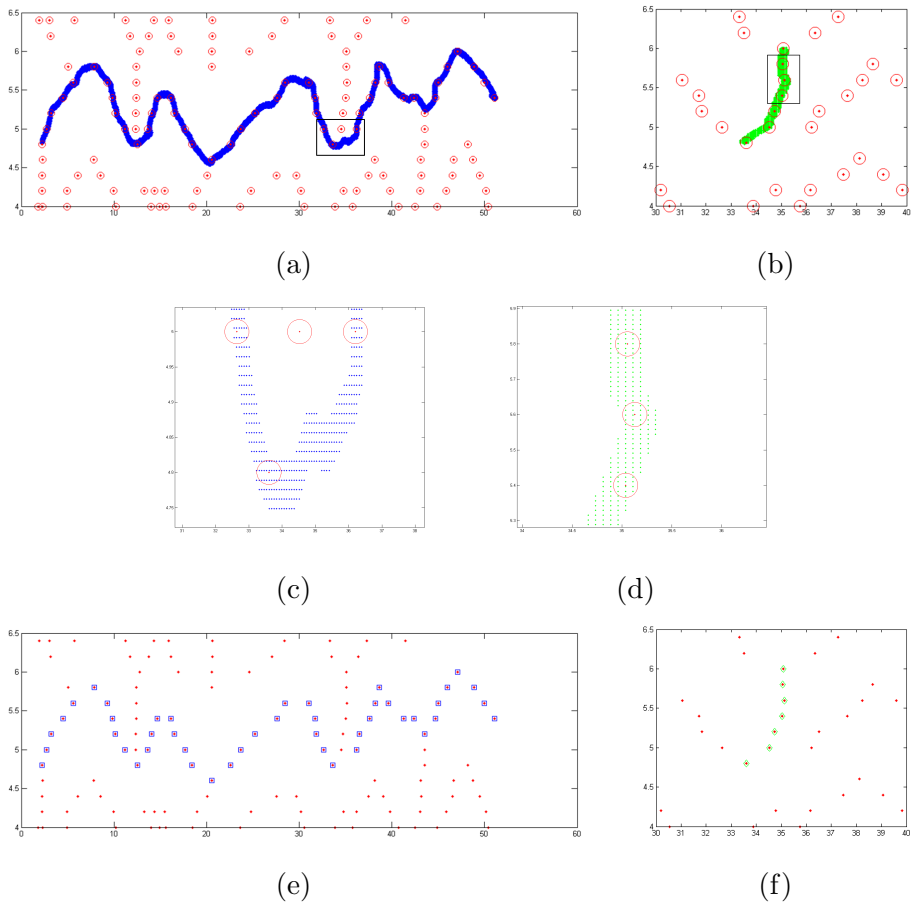

Figure 5.8: Categorization of 2D point cloud: (a) The operator draw a blue line to cover the points on a ring. (b) The operator draws a green line to cover the points on a beam. (c) Points that are within distant $\tau$ to the ring line are categorized as the ring points. (d) Points that are within distant $\tau$ to the beam line are categorized as the beam points. (e) A set of ring points separated out from the 2D point cloud. (f) A set of beam points separated out from the 2D point cloud.

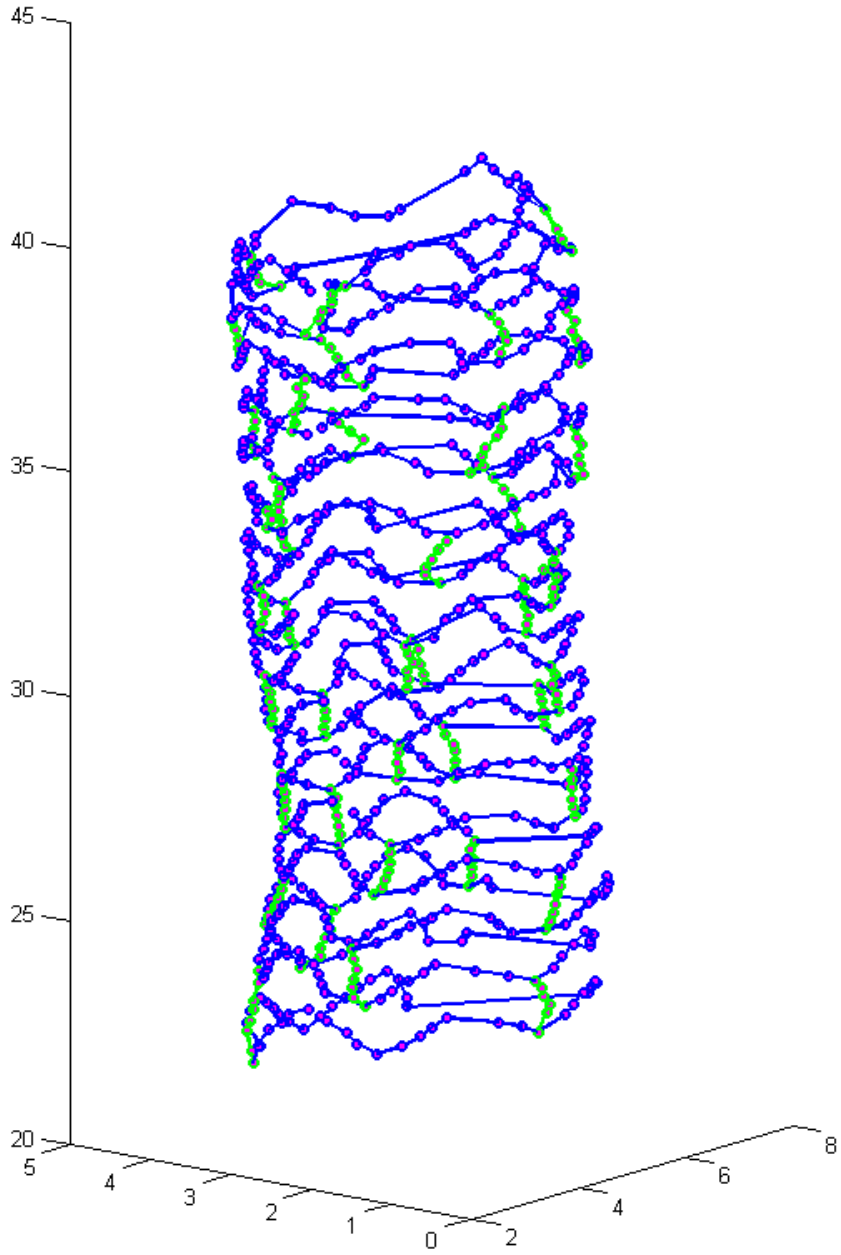


Figure 5.9: Connected 3D point cloud.

## 5.3 Stent volume reconstruction

The point cloud categorization in separate geometrical subsets, rings, and beams provides a skeletonization of the deployed stent.

As the OCT-derived data is limited to the central strut points' location; the actual volume occupied by the stent can be reconstructed only by a series of assumptions. The procedure, which is detailed in the remainder of this section, can possibly be adjusted to include more detailed OCT-derived data about the stent cross-sections' sizes and shapes.

For a given stent skeleton, the steps that lead to its volumetric reconstruction are as follows: 1) smooth wire-frame creation (i.e. a smooth volumeless stent skeleton representation); 2) strut cross-section registration along selected wire-frame points; 3) ring and beam volume bounding surface assembly; 4) connecting joint facet formation to obtain a continuous, closed surface.

### 5.3.1 Wire-frame creation

The stent skeleton is a coarse representation derived from a limited number of strut cross-sections identified in the OCT slices. In order to obtain a realistic stent volume reconstruction, a smooth stent skeleton interpolation is necessary. Ring and beam wire-frames are individually created using piecewise cubic splines.

The ring wire-frame is a periodic cubic spline that interpolates ring points $(x_1, y_1, z_1)$, $(x_2, y_2, z_2)$, ..., $(x_n, y_n, z_n)$. Since the spline is in 3D space, it should be parametric. Therefore, a parameter should be chosen to reflect the distance between the data points. A straightforward approach is to use the polar coordinate, $\theta$, as it is already computed during the strut point sorting.

$$\theta_i = \arctan \frac{y_i}{x_i}. \tag{5.17}$$

A natural choice here is to use a periodic spline as a function of $\theta$. This spline can be represented as follows:

$$S = S\left(X(\theta), Y(\theta), Z(\theta)\right) \tag{5.18}$$

where $X$, $Y$ and $Z$ are cubic spline functions with respect to $\theta$,

$$(x_i, y_i, z_i) = (X(\theta_i), Y(\theta_i), Z(\theta_i)). \tag{5.19}$$

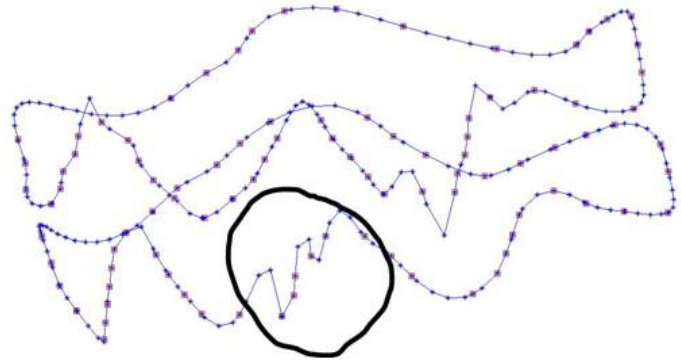

(a)

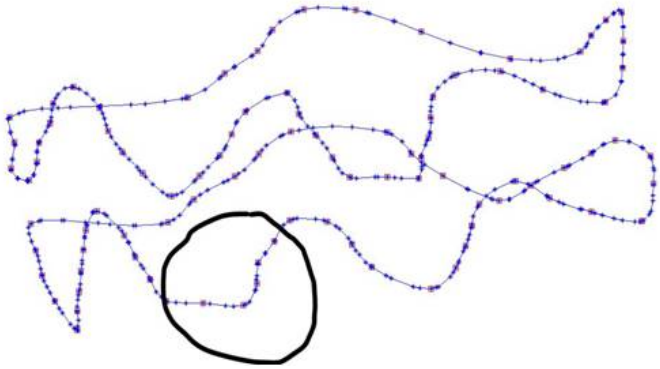

(b)

Figure 5.10: (a) When using $\theta$ as the parametric parameter, the ring splines show "wiggles". (b) The "wiggles" no longer exist when using the Eugene Lee's centripetal scheme with $k = 0.5$.

Unfortunately, while we need a periodic interpolation, cubic splines do not guarantee sufficient monotone properties to avoid occasional unphysical wiggles in the skeletonization (see Figure 5.10). For this reason, we need to resort to more specific techniques that may guarantee a smoother final result. In particular, we used Eugene Lee's centripetal scheme [45].

Rather than using $\theta$, this scheme helps choose a suitable parameter, $t$, which provides the proper spline tightness:

$$t_0 = 0 \tag{5.20}$$

$$t_i = t_{i-1} + \frac{\|P_i - P_{i-1}\|^k}{\sum_{j=1}^{n} \|P_j - P_{j-i}\|^k} \text{ for } 1 \leq i \leq n \tag{5.21}$$

where $P_i = (x_i, y_i, z_i)$. By trial and error, we found that $k = 0.5$ best represents the BVS. Moreover, $k$ can be adjusted according to the stent's physical property. As $k \to 1$, the spline becomes looser, but as $k \to 0$, the spline becomes tighter, which might be suitable for a more rigid metallic stent.

The 3D cubic spline $S\left(X(t), Y(t), Z(t)\right)$ is periodic, so we identified $t_1$ and $t_{n+1}$ as being equal. Then we ensured that

$$X(t_1) = X(t_{n+1}),\ X'(t_1) = X'(t_{n+1}),\ X'(t_1) = X''(t_{n+1}) \tag{5.22}$$

where $X(t)$ is defined as:

$$X(t) = X_i(t) = a_i + b_i(t - t_i) + c_i(t - t_i)^2 + d_i(t - t_i)^3 \tag{5.23}$$

for $t \in [t_i, t_{i+1}]$, $i = 1,\ 2, ..., n$ and

$$X_i(t_i) = x_i \quad i = 1,\ 2, ...,\ n$$

$$X_i(t_{i+1}) = x_{i+1} \quad i = 1,\ 2, ...,\ n$$
$$X_i'(t_i) = X_{i-1}''(t_i) \quad i = 2,\ 3, ...,\ n$$
$$X_i''(t_i) = X_{i-1}''(t_i) \quad i = 2,\ 3, ...,\ n$$

and similarly for $Y(t)$ and $Z(t)$.

Periodic and natural splines are used for rings and beams, respectively. By construction, all splines are parametrized by a single variable, $t$, where the value of $t_j$ for the interpolated data, $\mathbf{x}_j$, is the accumulated square root of the segment lengths connecting all $\mathbf{x}_j$ (i.e. $t_j = \sum_{i<j} \sqrt{||\mathbf{x}_{j+1} - \mathbf{x}_j||}$).

As for the algorithm described so far, we may have a disconnected skeleton since a beam is necessarily binded with two rings. However, we do need a connected skeleton for consistency with the real stent. In a fully connected wire-frame the two endpoints of all beams lie on the two rings that they are connecting. To construct a connected wire-frame, the ring splines are created first. Then, all beams are scanned to identify which ones have one

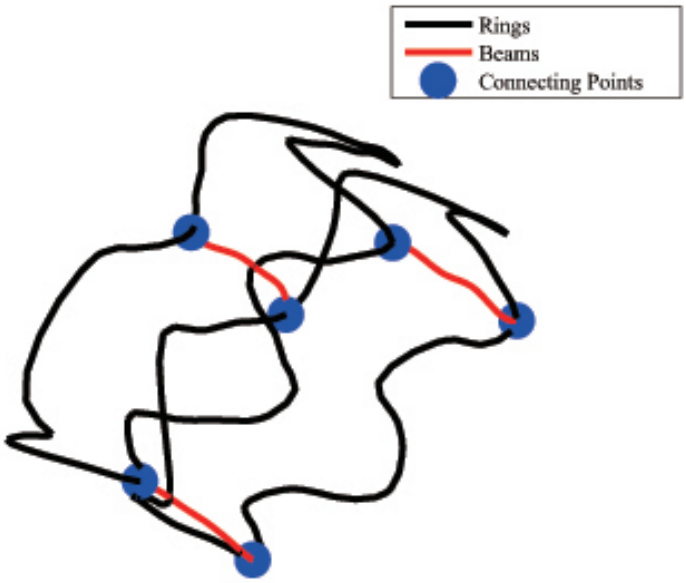


Figure 5.11: Stent connected wire-frame limited to two rings and the three beams.

or both endpoints disconnected from the bounding rings. If necessary, the disconnected beam data set is augmented with the closest ring point that lies on the associated ring spline. After this computation, the parameter $t$ for each beam spline is zero on the associated distal ring and $t_{\text{end}} = \sqrt{d}$, where $d$ is the sum of the length of all segments connecting the beam skeleton data points, on the associated proximal ring.

The volume of the stent around the wire-frame must be delimited by an appropriate choice of bounding surfaces. The fact that the strut cross-sections are known geometrical entities, derived either from OCT-data or from reasonable assumptions, offers a well-structured framework to define the wire-frame bounding surfaces via a two-step process. First, the strut cross-sections are registered via a rigid translation on selected wire-frame points. Second, points on adjacent cross-sections are connected to form quadrilateral facets. The final total volume bounding surface will be the union of the facets.

### 5.3.2 Registration of the strut cross-sections

The struts of the undeployed bioresorbable stent object of this study have a constant square cross-section with $l = 150\ \mu m$ side length. For the purposes of this study, it is assumed that during deployment, the deformations of the cross-sections resulting from the stent expansion performed by the clinical operator and from the implantation on a real tortuous anatomy can be all neglected. It can be also safely assumed that the stent cross-sections are not deformed by drug elution process taking place between the implantation and the post-implantation OCT imaging, since stent absorption is a three-year process.

A reference square cross-section $\phi_{\mathrm{R}}$, with side of length $l$, is defined on a cartesian reference system $(x, y, z)$. The center point $C_R$ of $\phi_{\mathrm{R}}$ coincides with origin of the reference system $(0, 0, 0)$. The square sides are aligned with the $x$ and $y$ axes, and a unit normal $\mathbf{n}$, is defined along the direction of the $z$ axis. A counter-clockwise numbering of the vertices, starting from the vertex in the first quadrant, provides a well-defined orientation of $\phi_{\mathrm{R}}$ on $(x, y, z)$ (see Figure 5.12). For every beam and ring forming the stent wire-frame, a set of unit vectors $\mathbf{t}_j(\mathbf{P}_j)$ is assigned to corresponding points $\mathbf{P}_j$ sampled on the splines. The directions of $\mathbf{t}_j$s are tangent in $\mathbf{P}_j$ to the splines associated to beams or rings. For each point $\mathbf{P}_j$, the reference cross-section $\phi_{\mathrm{R}}$ is rotated and translated via a linear transformation $T$ that acts on the reference vector $\mathbf{n}$ to transform it in the vector $\mathbf{t}_j$. In other words, this operation translates $\phi_{\mathrm{R}}$ to a new reference system whose origin coincides with $\mathbf{P}_j$ and $z$ axis coincides with $t_j$.

Although this operation is mathematically sound, in this study the OCT-derived stent dot data provide no information about the orientation of the transformed cross-section $\phi_{\mathrm{P}_j}$. Therefore, without further adjustments, the edges of $\phi_{\mathrm{P}_j}$ still have an arbitrary in-plane orientation around the normal $\mathbf{t}_j$. In the undeployed configuration, the square cross-sections have a straightforward orientation that is identifiable via the set of cylindrical unit directions $(\mathbf{h}, \rho, \theta)$ naturally defined on the stent cylindrical outline(see Figure 5.3a). Specifically, each cross-section on the plane $h = \bar{h}$ has two sides oriented perpendicularly to the local radial coordinate $\rho$ evaluated in correspondence of its center $C$. In the deployed stent configuration, due to the deformations associated with the implantation, the orientation of the struts cross-sections may have a non-negligible departure from the aforementioned undeployed orientation. For simplicity, in this study it is assumed that no change occurs

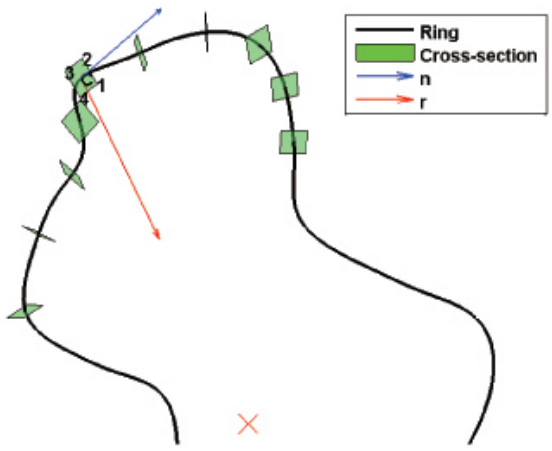


Figure 5.12: Samples of registered and re-oriented cross-sections $\phi_{\mathrm{P}_j}$. The normal, all registered vertices numbering and the final orientation $\mathbf{r}$ are reported for a selected $\phi_{\mathrm{P}_j}$.

in the cross-section orientation during the implantation.

Based on this argument, on each OCT slice, a local 2D polar reference system $(\mathbf{r}, \alpha)$ with origin in the vessel centerline can be defined. Thus, $\phi_{\mathrm{P}_j}$ can be re-oriented by rotating it around $\mathbf{t}_j$ to make two opposed square edges perpendicular to the direction defined by $\mathbf{r}$.

### 5.3.3 Assembly of ring and beam facets

The eight vertices of two consecutive $\phi_{\mathrm{P}_j}$ form the vertices of four quadrilateral facets $\mathcal{F}$. The numbering of the vertex defined on the reference $\phi_{\mathrm{R}}$ is consistently kept during the cross-sections registration on the wire-frame. For this reason, it is possible to automatically define the facets by grouping the vertices of $\phi_{\mathrm{P}_j}$ and $\phi_{\mathrm{P}_{j+1}}$ following a fixed rule. For example, one facet $\mathcal{F}_1$ is defined by the ordered set $\mathcal{F}_1 = (\phi_{P1,j}, \phi_{P2,j}, \phi_{P2,j+1}, \phi_{P1,j+1})$.

Rings are periodic and therefore the unions of all facets, ring by ring, results in a set of closed surfaces. Without any further processing, beams are open surfaces that, by definition of the wire-frame, intersect the rings that they connect.

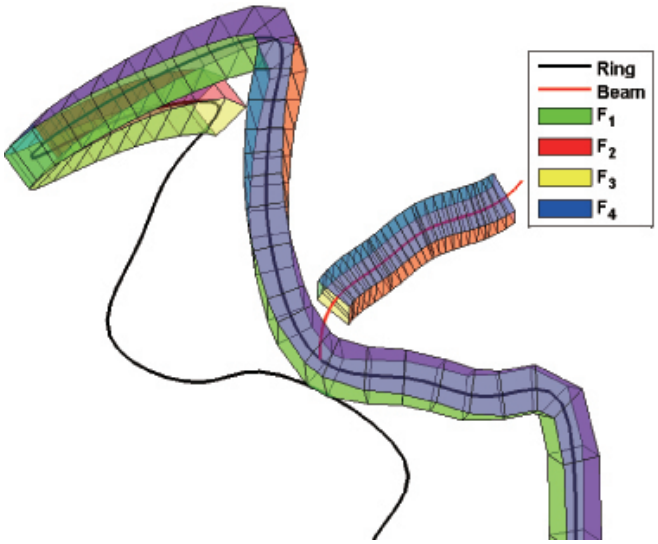


Figure 5.13: Sample of bounding facets assembled on a ring.

### 5.3.4 Formation of joints facets and creation of a continuous surface

The final objective of the procedure is to create a continuous surface that bounds the stent volume. The assembly of all bounding surfaces results in unwanted intersections between beams and rings. Furthermore, all rings are closed surfaces and provisions need to be made to continuously connect appropriate ring and beam facets, and remove rings facets where necessary.

In order to avoid collisions between beam surfaces and rings, each beam is individually examined. The registration of the reference cross-sections $\phi_{\mathrm{R}}$ is repeated on a new set of points $\hat{\mathbf{P}}_j$. The new set of points is calculated on the corresponding spline by finding the value of the parametrization variable $t$ which guarantees that, after the cross-sections registration, none of the $\hat{\mathbf{P}}_j$ collides with the closest connecting ring bounding surface. In practice, this can be achieved by setting a threshold distance between each beam's endpoints and the rings. Alternatively, more refined strategies based on solid collision algorithms could be employed.

The four vertices that define the open boundaries at the extremes of the collision-free beams form the first set of points of the joints facets. The remaining four joints facet vertices are found by identifying a suitable facet on the rings that are closest to the beams open boundaries. To limit the geomet-

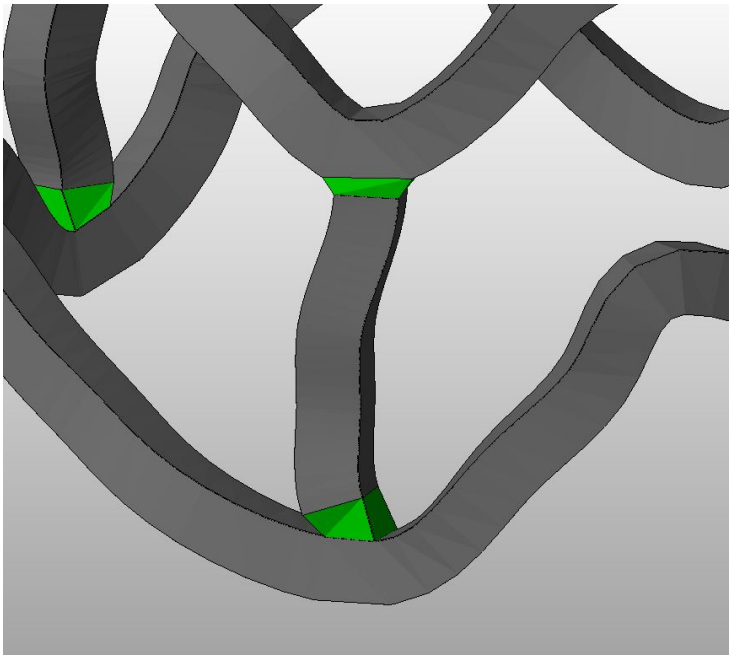

Figure 5.14: The joints between rings and beams are constructed separately.

rical reconstruction artifacts associated with the creation of connecting joints facets, the registration of the reference cross-sections on the rings is repeated with a procedure similar to the beam re-sampling detailed above. In this case, the goal of the re-sampling is to find, for each beam extreme connected to a ring, the two values of $t$ on the ring spline that define a quadrilateral facet of dimensions similar to the beam cross-section. On the re-sampled ring spline, all facets are recreated except the ones located in correspondence of the re-sampled connecting $t$ values, thereby leaving the ring surface open in correspondence of the sought joints. Finally, the joints facets are created from the union of the matching beam and ring joint vertices.

Here I acknowledge Dr. Gaetano Esposito's significant contribution to the stent reconstruction method introduced in this chapter, especially for the novel techniques that create stent struts with uniform thickness and connect rings and beams with smooth joints.

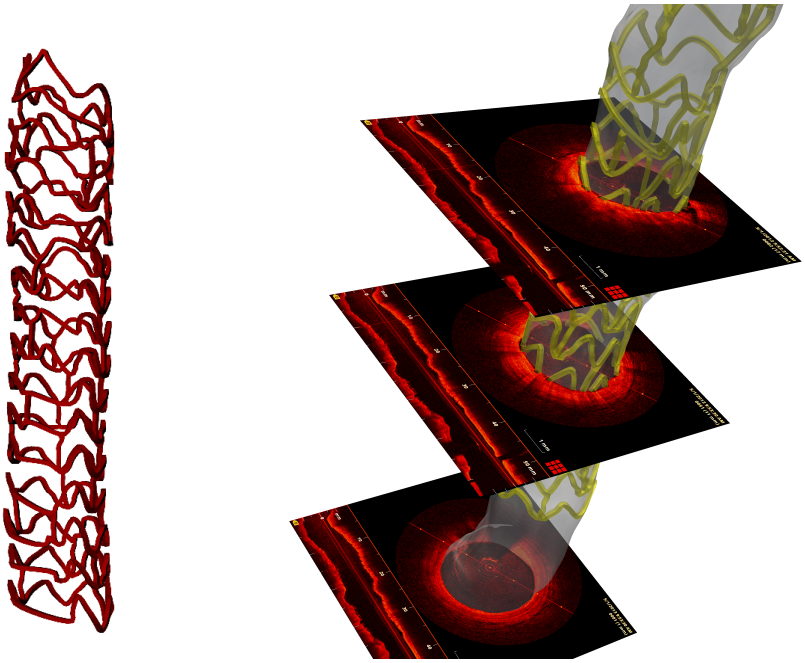

(a) (b)

Figure 5.15: (a) Reconstructed stent. (b) Reconstructed stent and lumen matched with OCT images.

## 5.4 Results and discussion

Using the methodology described in this paper, we successfully reconstructed deployed stents from three different patients. We provide a picture of our stent reconstruction's results in Figure 5.15a. The reconstructed stents appear to meet our expectations: the ring and beam structures are preserved, and the strut thickness is consistent in each. Furthermore, all parts are well connected, and the ring and beam joints are as smooth as in the stent design.

The reconstructed stent is patient-specific because it is derived from real patients' OCT images. When placing the OCT imaging of our stent geometry's corresponding cross-section (as shown in Figure 5.15b), the stent struts coincide with the OCT images, validating the stent reconstruction method.

The OCT image always has a catheter shadow due to the way the images were taken. The shadow is black and contains no information. However, the part of the stent in the shadow is also constructed along with the rest

of the stent because we applied periodical splines on every ring structure. Therefore, not only does the algorithm reconstruct the strut from the OCT image, but it also gives a predictive rendering for the hidden stent part.

For the technique presented in this chapter, the axis of the reconstructed stent is rectilinear since the reconstruction is based on the stack of OCT images available. However, the coronary artery has a curvature which can be retrieved only by other types of images. In particular, by using angiography we can bend the OCT rectilinear reconstruction to the real coronary curvature, as we explain in the next chapter.

# Chapter 6

# Reconstruction of stented coronary artery

## 6.1 Lumen reconstruction

The lumen geometry is constructed by stacking a series of 2D contours of lumen boarder that are automatically detected from the OCT slides. The lumen border extraction method is based on the work of L. Athanasiou et al. and M. Moraes et al.. First, the OCT image undergoes Ostu's automatic thresholding method [43] and becomes a binary image, in which the vessel wall appears to be white pixels. The catheter center is marked, and then radial pixel scanning from the catheter center is performed on the thresholded binary image. The first white pixels reached by the radial scan-lines are considered pixels on the lumen border. The initial lumen border pixel profiles have gaps at the catheter shadow and the side vessel branches. The gaps could be wide. To close a gap, we add the average point of the two end points of the gap to the pixel profile, and then we construct a periodic spline to complete the lumen border (see Figure 6.1a [46] [47]. This spline is considered the segmented lumen border. We can stack the lumen borders from all OCT slides with spacing of the OCT slides to form a rather straight lumen geometry, and we can also place the he lumen border perpendicularly to the catheter path and form a curved lumen geometry the curvature of which is obtained from the angiography (detailed in the next section).

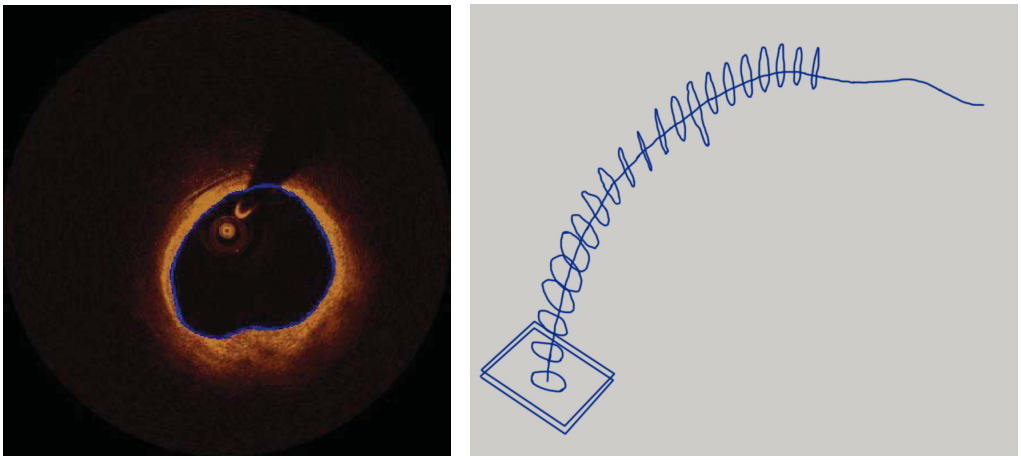

(a) (b)

Figure 6.1: (a) The blue line is the segmented lumen border from an OCT image. (b) Segmented lumen borders are placed perpendicular to the catheter centerline to form a curved lumen geometry.

## 6.2 Application of curvature to the stent and lumen

From the biplane angiography the 3D catheter path can be reconstructed (see Section 1.4.2). Then two landmarks are identified: we choose a point on the catheter path and another point on the corresponding slide of the OCT stack, and then we create a linkage between the two points. Both the catheter path extraction and the linkage of the two points are achieved using the software MEDIS (Leiden, The Netherlands, www.medis.hl). Then the lumen borders are stacked on the catheter path in a way similar to the method introduced by C. Slager et al. [48]. Starting from these landmarks, the lumen border splines are moved on top of the catheter and oriented perpendicularly to it (see Figure 6.1b). It should be noted that even though all OCT slices have a consistent planter orientation on the catheter, this orientation is often chosen randomly. The limitation of such a planter orientation is discussed in Section 9.2.

Once the lumen border profiles are positioned in 3D, the points of the spline are triangulated to create a surface, which is the final 3D vessel. Smoothing and surface re-meshing operations are often needed to make the

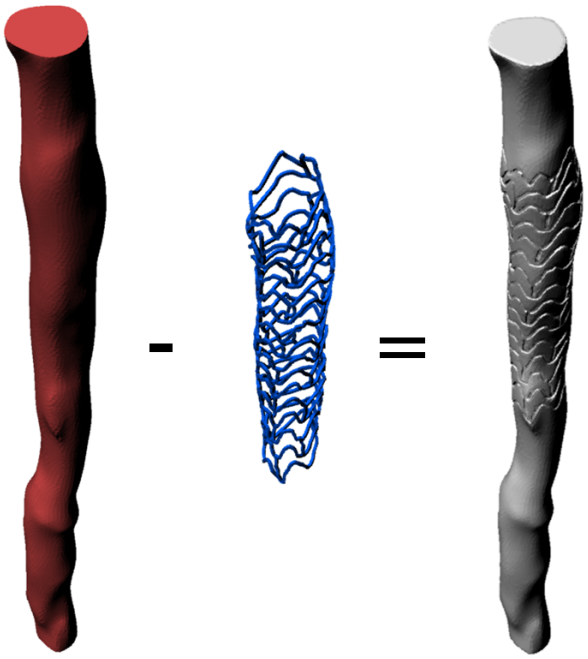

Figure 6.2: The Boolean operation: lumen subtracts stent.

surface ready for CFD simulations or other operations.

## 6.3 Finding the Euclidean difference of the lumen and the stent

A deployed stent keeps the vessel open, but the struts of the stent also take up space inside the vessel. Space remains for blood flow in the lumen after we exclude the volume of the stent geometry. Therefore, we subtract the stent geometry from the lumen geometry. This subtraction is a Boolean operation in 3D between the lumen STL and the stent STL files, illustrated in Figure 6.2. The resulting Boolean difference is the region of interest for CFD simulations.

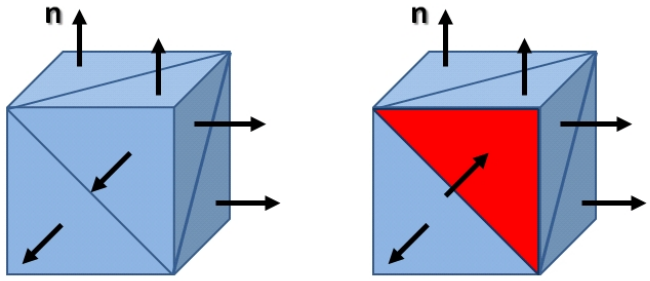


Figure 6.3: A STL geometry of a cube. The red triangle on the right side has its normal vectoring pointing inward, thus shall be corrected.

## 6.4 Geometry repair

We have obtained the geometry of the stented lumen by subtracting the stent geometry from the lumen geometry. The difference geometry is an STL file, which is a surface shell formed by triangles. All triangles have normal vectors pointing outward from the surface shell (see Figure 6.3). The STL file has the following format in general:

```
beginsolid
  facet normal ni nj nk
    outer loop
      vertex x1 y1 z1
      vertex x2 y2 z2
      vertex x3 y3 z3
    endloop
  endfacet
endsolid name
```

We use the software Magics 16 (Plymouth, MI, `http://www.software.materialise.com/magics/`) and Netfabb (Lupburg, Germany, `http://www.netfabb.com`) to repair the domain geometry. The stented lumen contains subtle features and STL errors that make it difficult to mesh. It is helpful to perform automatic repairs using the tool offered by Netfabb, but many problems are very resisting. Thus the geometry has to undergo a series of repair steps. Several types of triangles on the triangulated STL surfaces are problematic and have to be completely removed during the repair process in order to make the geometry meshable.

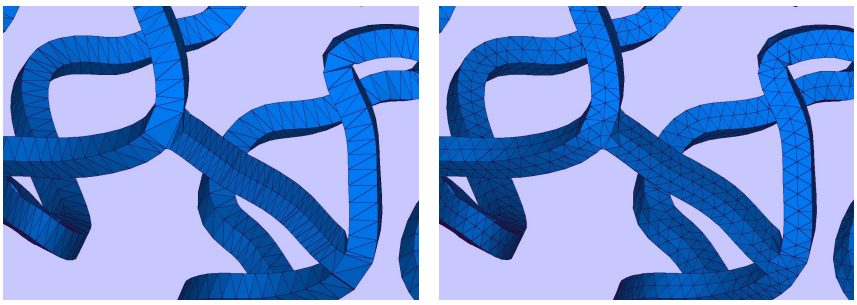

(a) (b)

Figure 6.4: (a) Stent STL file contains sharp triangles. (b) After re-triangulation, the stent STL contains no sharp triangles.

First, sharp triangles have to be removed. We define sharp triangles as triangles with one angle less than 15°. Due to the reconstruction method, the stent geometry contains an enormous amount of sharp triangles, leading to a large number of sharp triangles printed on the Boolean difference. A common practice to eliminate sharp triangles is to re-triangulate the surface of the Boolean difference, but the Boolean difference is the CFD domain and must be re-triangulated as little as possible to keep the original patient-specific geometrical features. Therefore, we first re-triangulate the stent geometry instead and eliminate its sharp triangles prior to the Boolean operation (see Figure 6.4).

Second, intersecting triangles have to be removed. Intersecting triangles are triangles that cut into each other. This occurs when the STL surface has intersections, especially after a Boolean operation is performed. Intersecting triangles can be detected and then removed by Magics; however, after the removal of all intersecting triangles, the geometry surface is often left with small holes, which are considered common errors for STL files. A correct STL geometry has to be a fully closed shell, thus we manually or automatically patch all holes.

The last type of problematic triangle is the overlapping triangle. A pair of triangles is defined as overlapping triangles if the circumcenters of the two triangles are less than $D_{overlap} = 0.01\ mm$ and the two planes where the two triangles reside form an angle less than 10°. When the geometry of the stent strut is fully embedded in the lumen geometry, the Boolean difference has a very thin layer on top of the hollow groove left by the stent, as shown in

Figure 6.5: A pair of intersection triangles.

Figure 6.6b. When those layers are thinner than 0.01, the triangles on the two sides of the layer form overlapping triangle pairs. Overlapping triangles prevents the geometry from being meshed. The only remedy is to remove the thin layers entirely. In some cases, the thin layers occur in a couple dozen places, and the removal can be done manually. If the number of thin layers is overwhelming, we implement Ellwein's method [10] and increase the radial thickness of the stent struts from 0.15 $mm$ to 0.30 $mm$, then take the Boolean difference.

After the removal of all problematic triangles, the surface STL may still not be meshed. The reason is usually the large number of sharp edges. An edge is sharp if the two planes where the two adjacent triangles sharing the edge form an angle of less than or equal to 90°. A 3D mesher can handle only a small number of sharp edges. A large number of short sharp edges is detrimental to the 3D meshing process. Unfortunately, the Boolean difference contains a large number of short sharp edges. One way to resolve this issue is to conservatively apply the smoothing function, which rounds off some sharp edges.

For any corner point $P = (x, y, z)$ on the geometry surface, the smoothing algorithm finds all its adjacent corner points $P_1, P_2, ..., P_n$, where $P_i =$

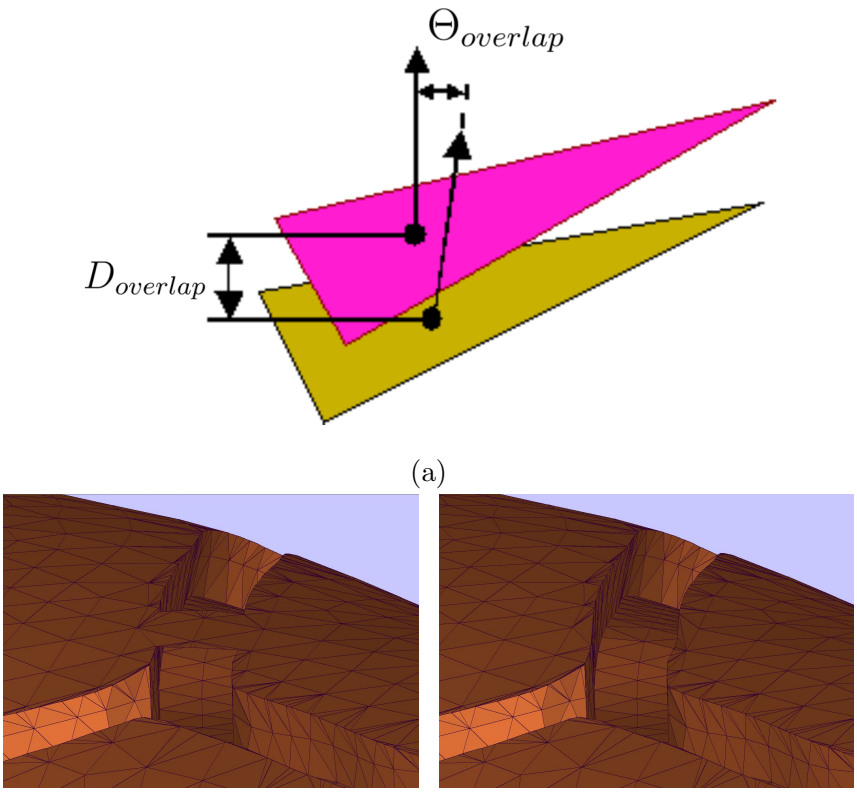


Figure 6.6: (a) A pair of overlapping triangles. (b) A thin piece on top of stent groove contains overlapping triangles. (c) The STL geometry after the thin piece is removed.

$(x_i, y_i, z_i)$. The center of mass of the adjacent corner points is calculated:

$$P_{mean} = (\overline{x}, \overline{y}, \overline{z}) = \left( \frac{\sum_{i=1}^{n} x_i}{n}, \frac{\sum_{i=1}^{n} y_i}{n}, \frac{\sum_{i=1}^{n} z_i}{n} \right). \tag{6.1}$$

A full iteration of smoothing would bring point $P$ all the way to $P_{mean}$. However, we aim to keep the original shape of the geometry and only smooth it to lesser extent. Through trial and error, we choose the smooth factor to be $t_{smooth} = 0.1$, which means we only move point $P$ 10% closer to point $P_{mean}$:

$$f : P \to P_{smooth},\ \overrightarrow{PP_{smooth}} = 0.1\overrightarrow{PP_{mean}}. \tag{6.2}$$

After the smoothing function is applied, the surface becomes slightly smoother, and corners with sharp edges become rounder because they are pulled inward. Smoothing is local re-triangulation and can change the original shape of the geometry, thus it must be applied carefully. The smoothing factor should never be greater than 0.2.

We typically obtain a geometry that could be meshed after completing the above steps. Unfortunately, this geometry repair is still not completely automated and it requires a strong interaction with the operator. We are working on an alternative solution that could improve or even bypass the repair steps, and we will discuss this possible solution as a future direction in Chapter 10.

In Figure 6.7, we present the successful reconstruction of the three patients obtained so far (Case 1, 2 and 3). It is worth noting that, to the best of our knowledge, these are the most accurate patient-specific geometries we found in the literature.

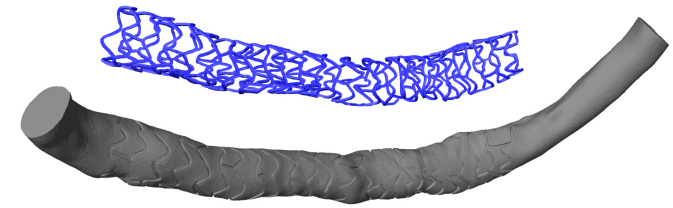

(a)

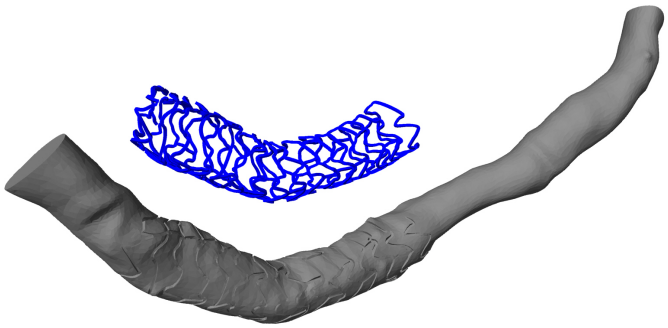

(b)

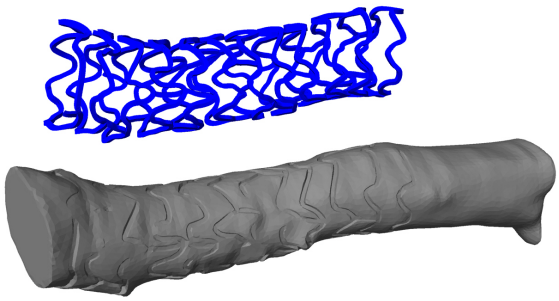

(c)

Figure 6.7: Reconstructed stent and stented lumen with curvature obtained from angiography for (a) Case 1, (b) Case 2, and (c) Case 3.

# Chapter 7

# The CFD simulations

In this chapter, we finally present numerical simulations of blood flow in patient-specific settings. We proceed by first presenting the delicate step of meshing that we accomplish by using Netgen. Then the Navier-Stokes equation is solved in the CFD domain for the incompressible blood flow. After the pressure and velocity are obtained, WSS is also computed. Then we present our results with visualization and discussion.

## 7.1 A priori adaptive meshing

The geometry of the stented artery needs to be efficiently discretized for the CFD simulation. The geometry was meshed with unstructured tetrahedral elements. To catch the disturbance and possible recirculation around the stent struts, we have to ensure that the size the elements near struts is at least 4 times smaller than the height of the strut, making extremely small elements of 0.02 $mm$ in size. If we keep this element size across the entire geometry, the estimated total number of nodes will be over 20 million, making the execution of the CFD impossible. Therefore, an a priori adaptive meshing scheme was implemented so that we could have highly concentrated mesh near the stent struts yet keep the overall number of nodes manageable for the finite element CFD:

1. A coarse base mesh was created with element size around $h_{base} = 0.1\ mm$ for the entire geometry of the stented lumen.

2. A boundary layer of thickness $d = 0.3\ mm$ was identified. This layer starts from the outer surface of the stented lumen geometry and goes 0.3 $mm$

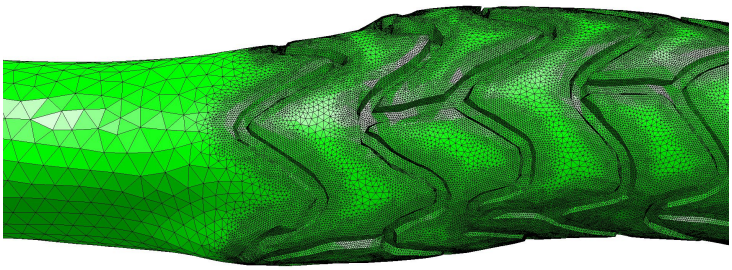

(a)

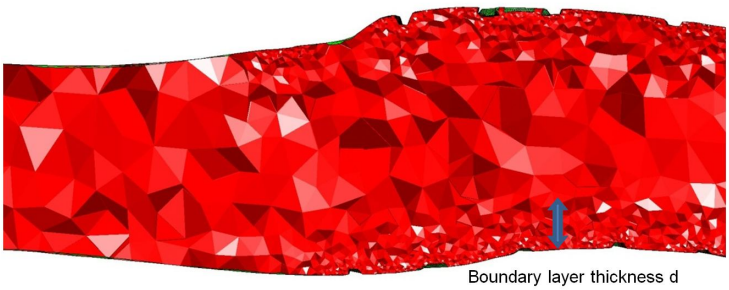


(b)

Figure 7.1: (a) Regions near the struts are meshed with small elements. (b) Boundary layer with thickness $d$.

toward the center of the lumen. Thus the thickness of the boundary layer is about $\frac{1}{5}$ of the average lumen radius $r = 1.5\ mm$.

3. All surfaces of the stent struts are labeled using the stent geometry.

4. A refinement process gradually takes place in the boundary layer. The elements on the labeled strut surfaces are refined to $h_{fine} = 0.02\ mm$ in size. As we went from the strut surfaces to the inner surface of the boundary layer, the element sizes were reduced to $h_{base} = 0.1\ mm$ in a linear rate with respect to the boundary layer thickness $d$.

The a priori adaptive meshing scheme ensured that there are enough elements near the struts to reveal local subtlety in the blood flow while keeping the total number of nodes under 3 million. Compared to the previous uniformly refined boundary layer used in the preliminary study with idealized geometry, this gradually refined boundary layer improves the reliability of the CFD. The gradual change in element size gives a smaller spread in eigen-

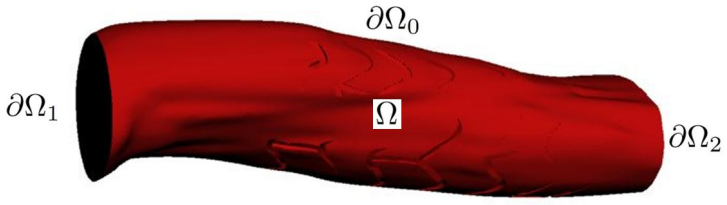


Figure 7.2: A demonstration of the CFD domain and boundaries.

values of the finite element mass matrix $A$, which keeps a relatively small conditioning number: $Cond(M) = \|A\|_2\|A^{-1}\|_2$.

The small conditioning number leads to less perturbation in $A$, making the solution more reliable.

## 7.2 Computational fluid dynamics

Blood is incompressible and viscous, and the stented coronary artery is large enough to apply the Newtonian fluid model for CFD. Therefore, we use the Navier-Stokes equation to model the blood flow in the stented coronary artery (see Equation 2.1). We denote the reconstructed patient-specific CFD domain by $\Omega$. We denote by $\partial\Omega_1$ and $\partial\Omega_2$ the proximal and distal sections, respectively, because they coincide with the inflow and outflow sections of domain $\Omega$. The remaining boundary of the domain $\Omega$ is denoted by $\partial\Omega_0$

For the boundary conditions, we assume that the vessel wall $\partial\Omega_0$ is rigid; we prescribe a specific inflow function normal to the inflow section $\partial\Omega_1$ and the "do-nothing" boundary condition to the outflow section $\partial\Omega_2$:

$$\begin{cases} u \cdot n = \dfrac{Q\,(t)}{|\partial\Omega_1|},\ u \times n = 0 & \text{on } \partial\Omega_1 \\ u = 0 & \text{on } \partial\Omega_0 \\ pn - \nu\left(\nabla u + \nabla u^T\right) \cdot n = 0 & \text{on } \partial\Omega_2 \end{cases} \tag{7.1}$$

The flow rate function $Q(t)$ is interpolated by cubic spline from 100 flow rate data points of a real patient, shown in Figure 7.3. This flow rate function represents the pulsatile nature of a cardiac cycle with a single peak at 2.7 $cm^3/s$ and a single nadir at 0.9 $cm^3/s$. The period duration of $Q(t)$ is 0.85 $s$, which is also the length of the cardiac cycle. The flow rate function

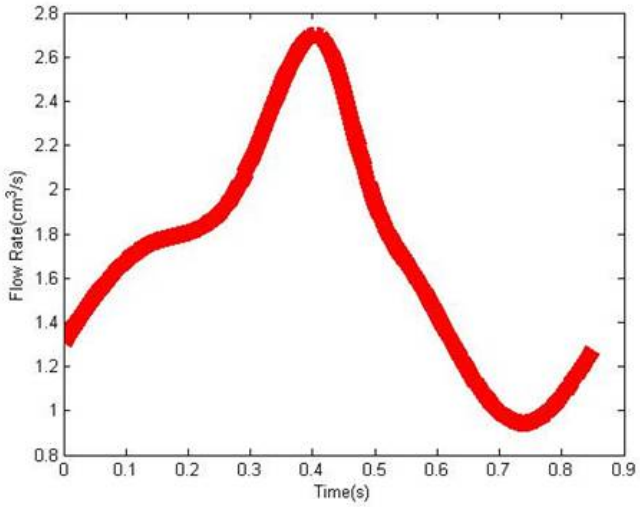


Figure 7.3: The pulsatile flow rate function prescribed on $\partial\Omega_1$.

is not from the same patient whose OCT is processed because the flow rate was not measured during the stenting procedure. However, in any future simulations, we can prescribe the inflow function of the same patient whose OCT images are processed if the patient's inflow function is available.

The Navier-Stokes equation with the boundary conditions is solved using the finite element method on the tetrahedral discretization. As shown in Figure 7.4, for each tetrahedron element, the pressure $p$ is represented by the four corner point (1-4) values and interpolated using a linear polynomial($P_1$). The velocities $u$ are represented by all 10 points (4 corner points, 1-4, and 6 side points, 5-10), using quadratic polynomials ($P_2$). The choice of the ($P_2$, $P_1$) for velocity and time is called Taylor-Hood finite element, and it is inf-sup compatible [49]. Though quadratic elements ($P_2$) for velocity could be computationally expensive, it is necessary because velocities subsequently determine the WSS, an important factor in the clinical analysis of a stented coronary artery.

After the results for $u$ and $p$ are obtained, the WSS $S_w$ on $\partial\Omega_0$ is computed:

$$S_w = Tn - (Tn \cdot n)\, n \text{ on } \partial\Omega, \tag{7.2}$$

where

$$T_n = \left(\nu \left(\nabla u + \nabla u^T\right) - pI\right) n, \tag{7.3}$$

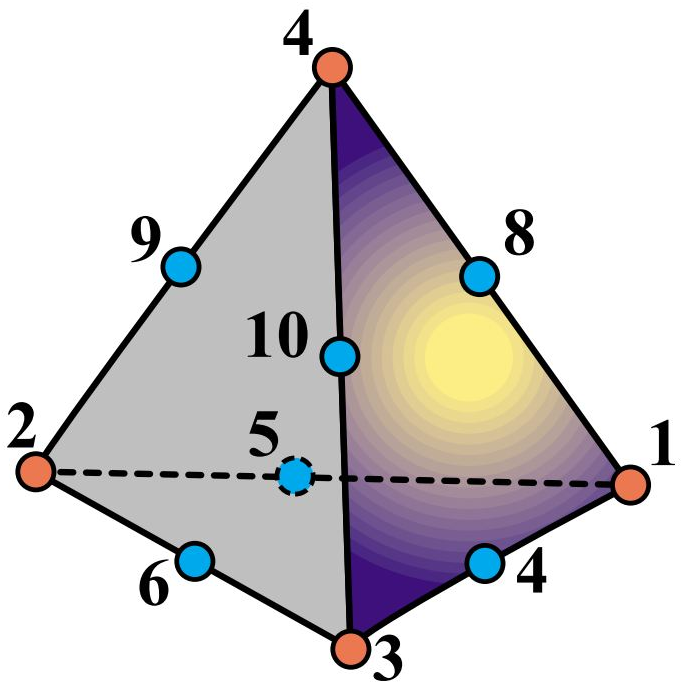


Figure 7.4: A demonstration of a tetrahedron element.

and we visualize $\|S_w\|$, the magnitude of the WSS. The CFD simulations are carried out using LifeV (EPFL, Switcherland; Politecnico di Milano, Italy; INRIA, France; and Emory University, USA). The visualization of all results are done with the software Paraview.

## 7.3 CFD results and discussion

In this section, we will first present the CFD results of Cases 1, 2, and 3 with their patient-specific curvatures.

Adding curvature to the vessel geometry could bring the simulation one step closer to hemodynamics reality inside the patient's coronary artery; however, the OCT images' planter orientation on the catheter path could be random, making the final curved geometry less accurate. In addition, the steps required for making the curved vessel geometry slow down the reconstruction/simulation process. Therefore, it is necessary that we run a simulation (Case 2) without the curvature. The simulation results will provide information about the blood flow within the originally reconstructed lumen and stent geometry before a potentially inaccurate curvature is applied. This can also serve the purpose of comparison between a straight vessel simulation and a curved vessel simulation so we can understand how much the curvature affects the hemodynamics of a stented coronary artery.

### 7.3.1 Results of Case 1-3 with curvature

Using the reconstructed geometries of the curved stented lumen (Figure 6.7, Section 6.4), we conducted CFD simulations for Cases 1, 2 and 3 , including patient-specific curvature, using the departmental server GAUSS which has four Intel Xeon X5670 CPUs with 2.93 GHz. The number of time steps in one cardiac cycle was set at 100, and the number of nodes in the mesh for the three cases was under 30,000 to allow velocity and pressure results to be obtained within 72 hours.

Pressure and velocity behaved as expected (Figure 7.5a - 7.5f): pressure was reduced from the inflow section to the outflow section and velocity was reduced from the center of the lumen to the vessel wall. Although the mesh is relatively coarse, we can still observe spatial WSS oscillation around the stent struts (Figure 7.5g - 7.5i). All images in Figure 7.5 were taken at the cardiac peak (time 0.4675 $s$ of cycle 0.85 $s$). Such WSS oscillation in space

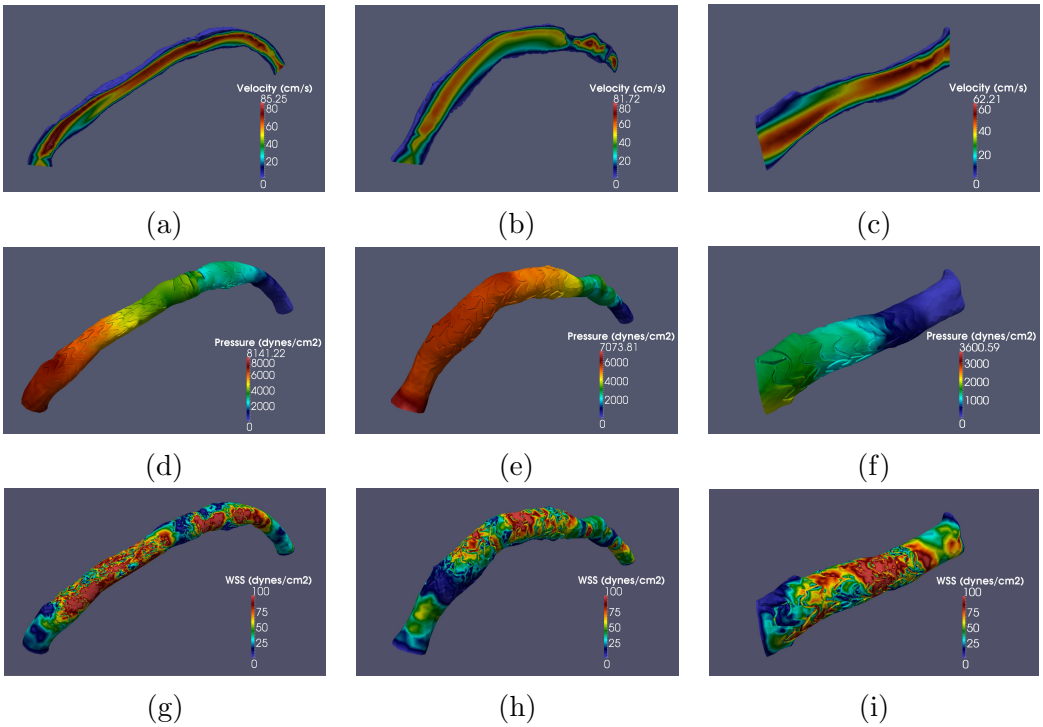


Figure 7.5: (a) Simulations results of Case 1-3 at cardiac peak: (a) Case 1 velocity. (b) Case 2 velocity. (c) Case 3 velocity. (d) Case 1 pressure. (e) Case 2 pressure. (f) Case 3 pressure. (g) Case 1 WSS. (h) Case 2 WSS. (i) Case 3 WSS.

is induced by the disturbed blood flow around the stent struts.

### 7.3.2 Results of Case 2 without curvature

We chose Case 2 geometry without curvature and meshed it with the a priori adaptive meshing scheme described in Section 6.1. In the boundary layer, we ensured that at least four elements could fit in the stent strut thickness, and the overall number of nodes (points in tetrahedral mesh) was just under three million. We set the time step to $\Delta t = 0.0017$ so that we could have 500 time steps in the 0.85 $s$ cardiac cycle. Simulations on this scale have to be performed in parallel on a cluster computer more powerful than the departmental server. We used 32 Intel Xeon E5-2680 processors with 2.70 GHz at Texas Advanced Computing Center, each processor containing eight

cores and 32 gigabytes of memory. It took approximately 72 hours to finish the CFD for one cardiac flow cycle.

At the peak of the cardiac cycle, pressure $p$ decreased from 3000 ($dyne/cm^2$) at the inflow section to 1000 ($dyne/cm^2$) at the outflow section; at the cardiac nadir, the pressure decreased from 1500 at the inflow section to 500 at the outflow section (see Figure 7.6a and 7.6b). The stent structure has an impact on the velocity. In general, the velocity magnitude is lower near the vessel wall because of the viscosity of the fluid. The velocity stream lines along the stent show disturbance. It should be noted that recirculations are found behind the struts (Figure 7.8a). This indicates that the thick strut promotes flow separation in the proximal and distal region of the strut.

The oscillatory behavior of WSS caused by the stent struts is significant (Figure 7.7). To understand the pattern of such oscillation in space, we extracted a line of WSS data (Figure 7.9a), then plotted the WSS magnitude against the horizontal direction of the stent (Figure 7.9b). A bar chart was also created according to the WSS magnitude at five locations of each oscillation (Figure 7.10). As the blood flow first enters the strut, WSS drops to a local minimum (inflow ditch). Then WSS increases along the proximal surface and reaches a maximum at the endoluminal surface. WSS remains high on the endoluminal surface (top strut), but it immediately starts to decrease when the blood flow reaches the distal surface of the strut. WSS drastically decreases along the distal surface all the way to another minimum (outflow ditch). As the blood flow leaves the strut, WSS slowly increases again. Similar to the behavior of WSS observed in the idealized study (described in Section 3.3), this pattern of WSS oscillation in space repeats itself at every strut.

The combination of such WSS oscillation and flow recirculation could induce plaque progression. Procoagulant conditions are greatly increased around the stent strut because the accelerated flow over the strut edges yields high WSS magnitudes, activating platelets, some of which will enter the distal flow separation zone (Figure 7.8b). Then the recirculation zones retain those activated platelets to critical concentrations for the activation of thrombosis [50]. The detected recirculations could be a contributing factor to thrombosis and restenosis after BVS deployment [7].

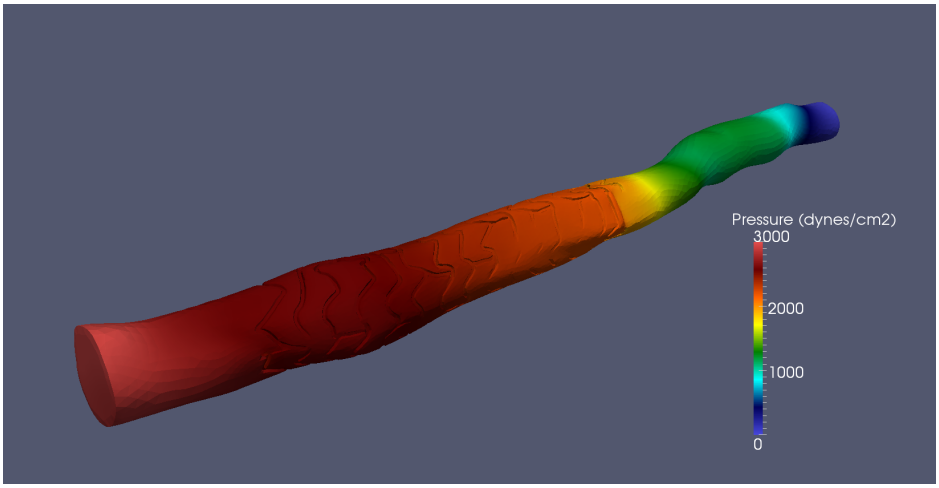


(a)

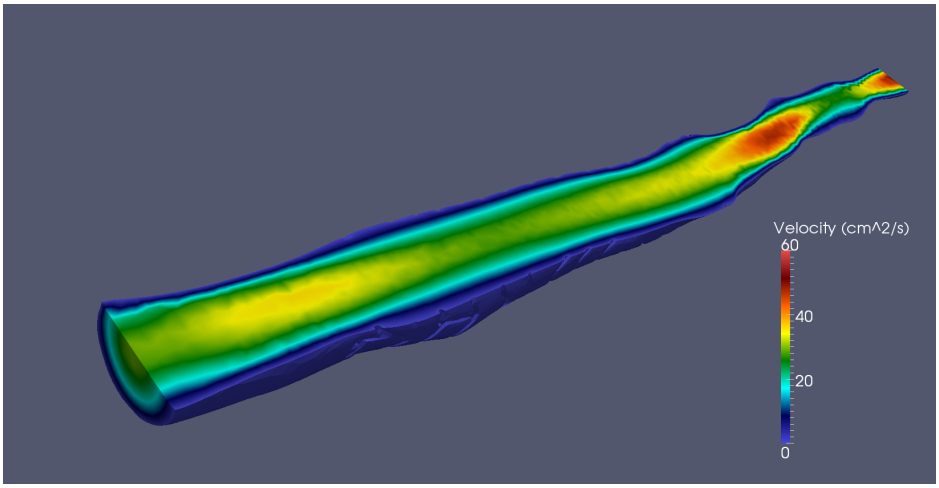


(b)

Figure 7.6: (a) Pressure at the peak of the flow. (b) Velocity at the peak of the flow.

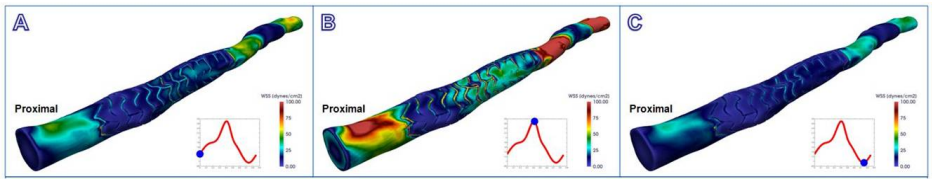


(a)

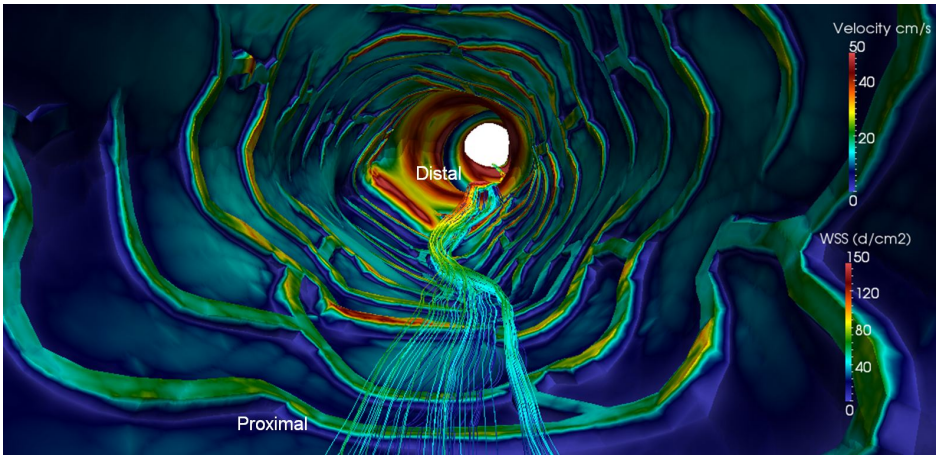


(b)

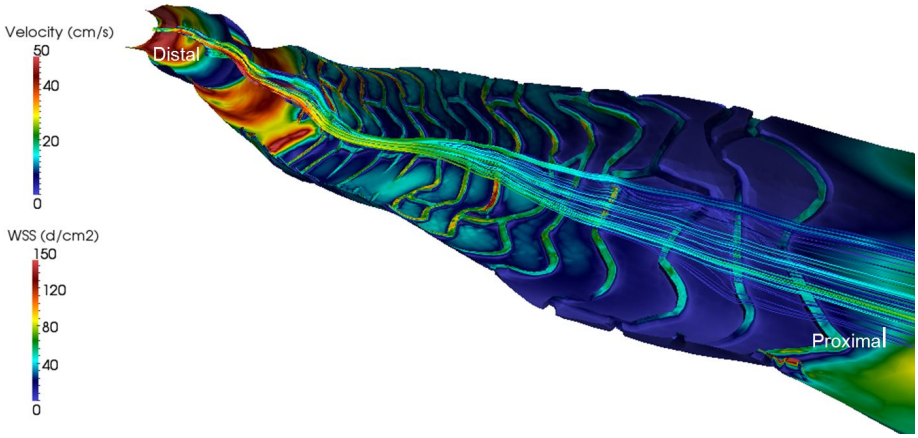


(c)

Figure 7.7: (a) WSS in first time, flow peak, and flow nadir. (b) Velocity streamlines with WSS in background at flow peak. (c) The longitudinal review of velocity streamlines with WSS in background at flow peak.

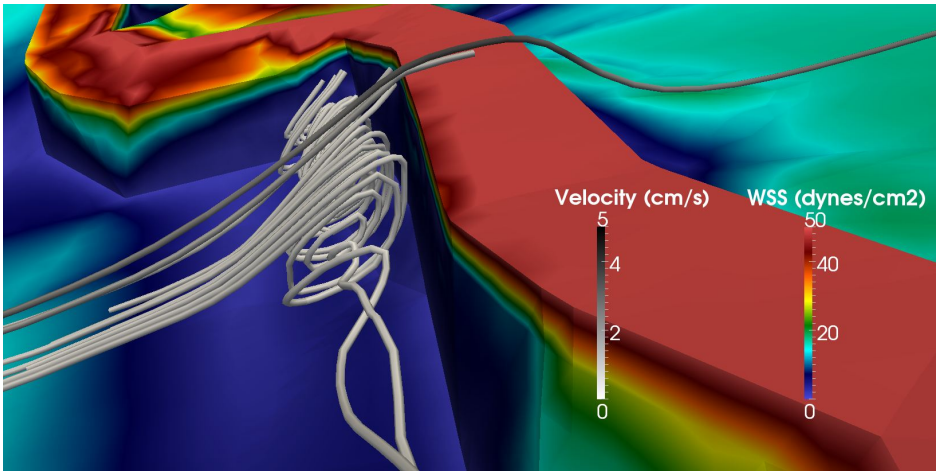


(a)

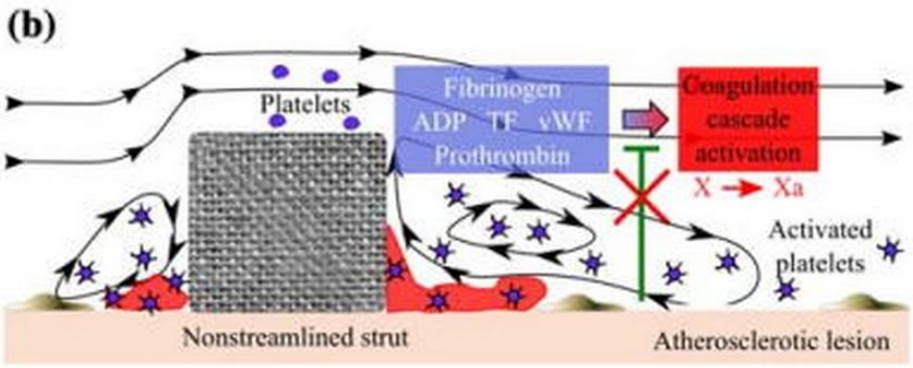


(b)

Figure 7.8: (a) Blood flow recirculation behind a strut. (b) A demonstration of platelets entrapped in the recirculation zone [7].

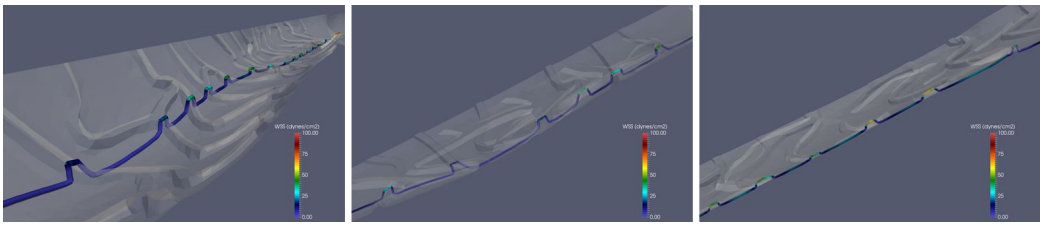

(a)

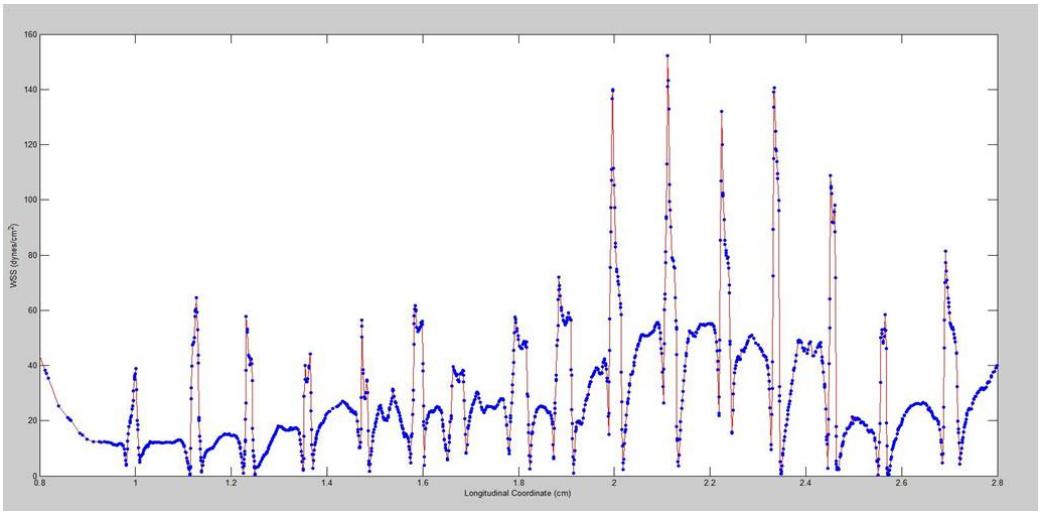


(b)

Figure 7.9: (a) A line of WSS data is extracted from the simulation results. (b) Plot of WSS magnitude on this line.

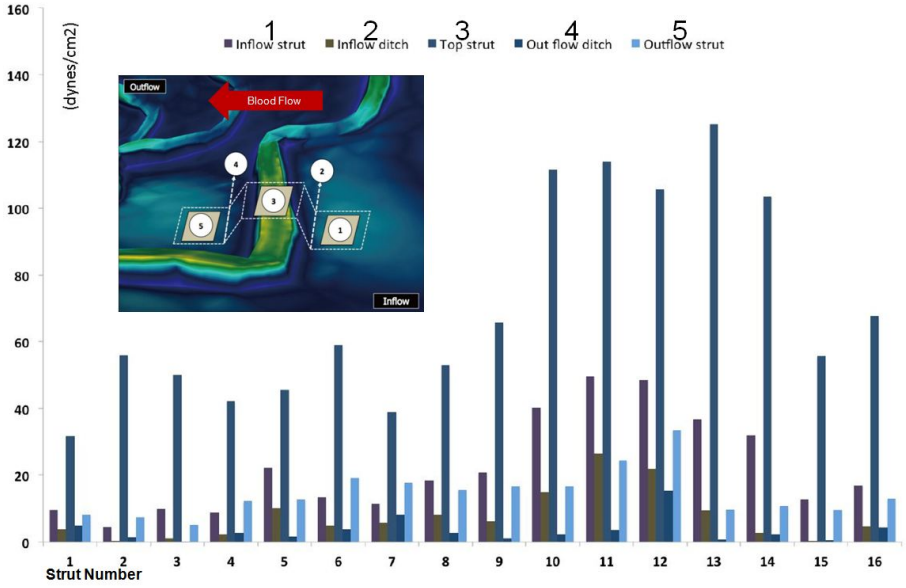


Figure 7.10: Bar chart of WSS on five locations of each ring strut.

### 7.3.3 Comparison between straight and curved Case 2 results

As we have run CFD simulation for both the curved Case 2 and the straight Case 2, with the same inflow function, we had the opportunity to compare the WSS in the two scenarios for the same stent and to investigate how the curvature affect hemodynamics of stented coronary artery. In Figure 7.11a, we present the local WSS around the 11th ring strut on the outer curvature, inner curvature, and with no curvature. Despite the fact that the simulation of the curved Case 2 was performed on a relatively coarse mesh, we were able to obtain the WSS at locations 150 $\mu m$ before the strut, on top of the strut, and 150 $\mu m$ after the strut (the locations are illustrated in Figure 7.10). inflow strut, 3. top strut, and 5. outflow strut). When there is no curvature in the geometry, WSS oscillation is in the expected range (before strut 49, on top of strut 108, and after strut 31 $dynes/cm^2$). On the outer curvature, the WSS has increased oscillation. However, the WSS magnitude is also significantly higher (before strut 95, on top of strut 264, and after strut 66 $dynes/cm^2$), which could reduce the danger induced by the oscillation as there is an inverse correction between WSS and plaque growth. On the inner

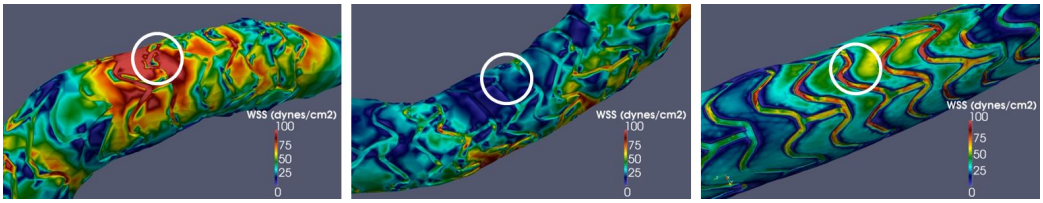


(a)

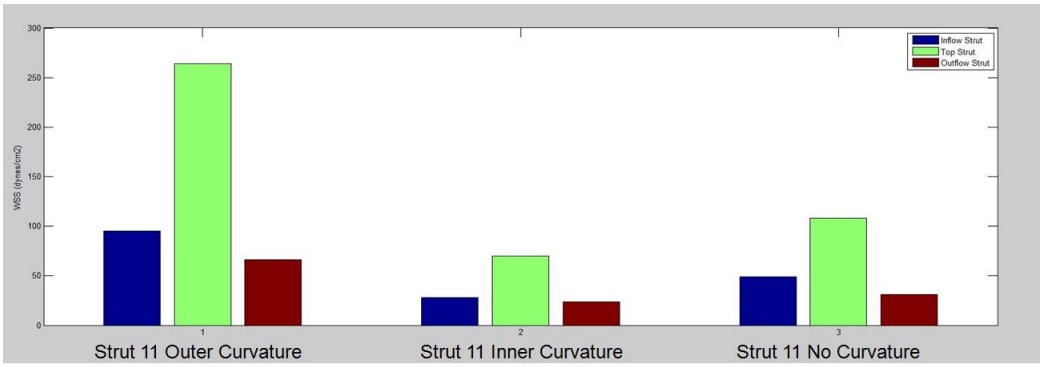


(b)

Figure 7.11: (a) WSS on the 11th ring. Left: outer curvature, Middle: inner curvature, Right: no curvature. (b) Bar chart of WSS before strut, on top of strut, and after strut of the 11th ring.

curvature, WSS is very low (before strut 28, on top of strut 70, and after strut 24 $dynes/cm^2$). The WSS on the inner curvature before and after the strut of the 11th ring both remain under 30 $dynes/cm^2$. Combined with oscillation caused by the stent, this low WSS could be linked to faster vessel wall thickening in the inner curvature or even to plaque progression [51].

# Chapter 8

# Extension to metallic stent reconstruction

In previous chapters, we presented our patient-specific reconstruction of the bioresorbable vascular stent (BVS). The methodology was developed for BVS since BVS is the new breakthrough of the stenting technology and has huge potential in true vessel restoration. A good methodology should have a wide range of application. Could we apply the reconstruction methodology to another type of stent? In this chapter, we answer this question by showing how we can extend the reconstruction methodology to the drug-eluting metallic stent, which is the second most advanced type of stent in the evolution of coronary stenting technology.

Unlike the fully Bioresorbable vascular stent, the medal structure will remain permanently in the vessel after its drug coating is released into the vessel wall. The drug eluting metallic stent is fully approved in the US and is currently the most widely implanted type of stent. However, there are less CFD simulations and structural simulations using high quality patient-specific metallic stent geometry. We herein extend the stent reconstruction methodology to the Abbott XIENCE drug-eluting metallic stent, which is approved by US Food and Drug Administration in 2011 and is one of the most advance metallic stent. This metallic stent reconstruction methodology is achieved by the fusion of the automatic metallic stent strut detection algorithm by A. Wang et al. [52], and the modified version of our stent geometry reconstruction, along with some manual correction and repair.

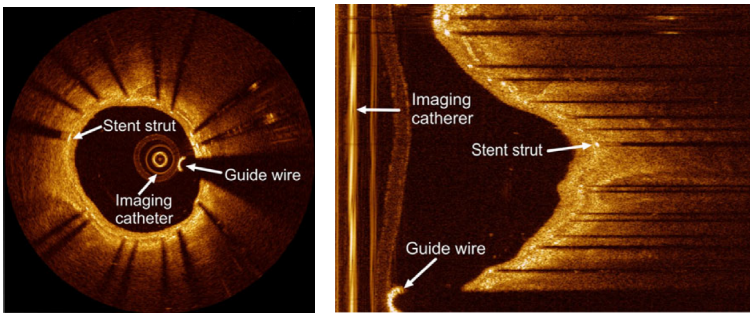


(a) (b)

Figure 8.1: (a) An OCT slice in polar coordinate system. (b) The OCT slice in Cartesian coordinate system.

## 8.1 Automatic detection of metallic stent strut from OCT images

In fact, the metallic stent struts are easier to detect than BVS struts. In OCT images, the metallic struts reflect most of the light, while normal vessel tissue scatters attenuate the light. Therefore, in each OCT image, the metallic strut appears as a bright point and leaves a long black tail behind. OCT is usually presented in Cartesian coordinates, and the black tails of the strut appear as rays radiating from the catheter center (see Figure 8.1a). If we convert the OCT into polar coordinates with its center at the catheter center (see Figure 8.1b), the black tails become horizontal to each other, convenient for automatic detection.

After the OCT in the polar coordinate system is obtained, it is then horizontally scanned line by line. The intensity value profile of each line is plotted. Figure 8.2 shows two examples of the intensity profile. In general, one cannot state that the struts always have the highest intensity values in an entire OCT pullback run. For that reason, a global intensity threshold for the strut is not applicable. Instead, we analyze the slope of the intensity profile. By detecting the maximum intensity and the distance between peak point and the first pixel of the potential shadow area, the slope is calculated. A steep negative slope reflects the drastic difference in intensity value between a bright metallic strut and its black shadow tail. When there is a peak of intensity value with a slope steeper than $-80$ followed by a tail of at least 30 continuous low intensity pixels, the location of the intensity peak is recorded

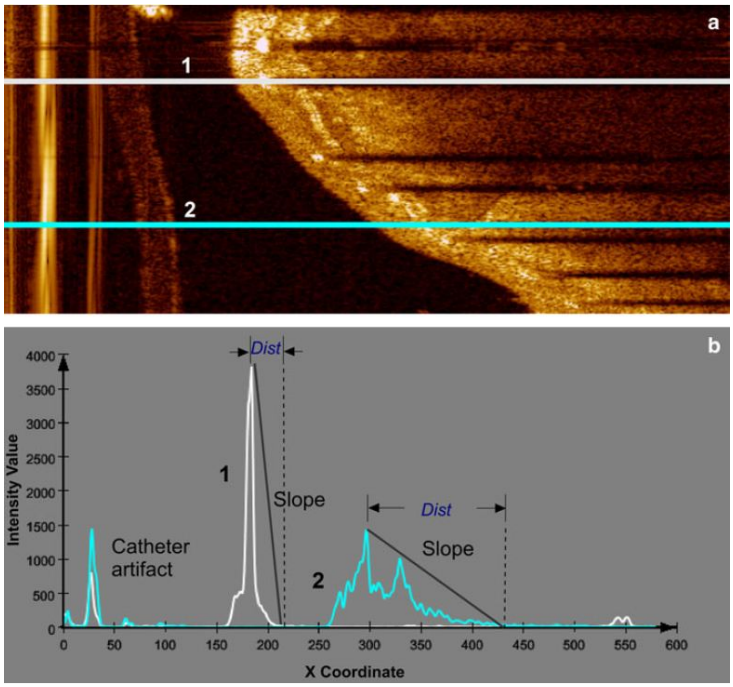


Figure 8.2: The intensity profiles of two scan-lines. The white scan line has a peak followed by a steep slope and a long tail of low intensity pixel, thus the its peak is recognized as a strut point.

as a strut point. An example of a set of detected strut points is shown in Figure 8.2. To validate the accuracy of the detection method, Wang et al. applied automatic detection to 10 OCT pull back sets and compared the results with the results obtained by a human observer. The accuracy is determined by 1) sensitivity, which is defined by Wang et al. as the ratio between the number of struts correctly detected by the algorithm and the number of struts found by the human observer, and 2) false positive ratio, which is defined as the ratio between the number of false positives in the automatically detected results and the total number of struts found by the observer. The average sensitivity and false positive ratio for the 10 pull back sets is 94% and 4% respectively [52].

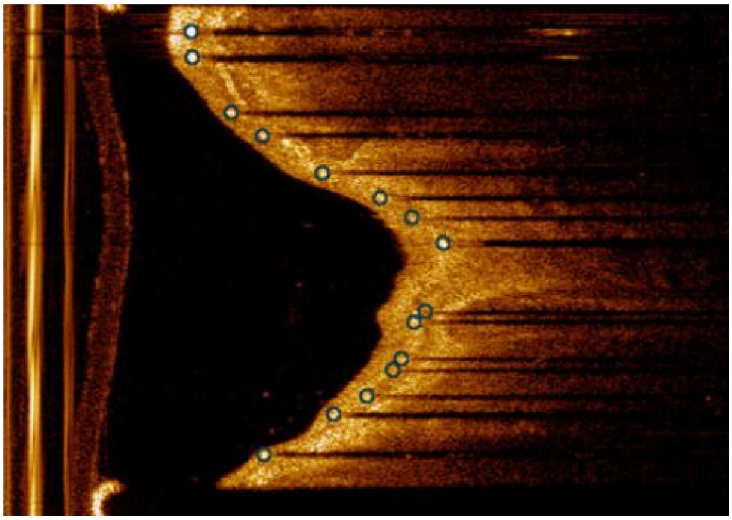

Figure 8.3: The detection results of metallic strut points from OCT in Cartesian coordinate system.

## 8.2 Metallic stent reconstruction on the detected strut point cloud

The detection algorithm is performed on all OCT slices. Similar to the BVS reconstruction, the metallic stent pattern can be recognized from the 3D strut point cloud, as shown in Figure 8.4. We also refer to the structure that goes around the stent as ring and the vertical structure as beam. The rings resemble the sinusoidal waves as in BVS, but the beams have small square wiggles on them (see Figure 8.4a). The 3D point cloud shows the small wiggles on the beams (see Figure 8.4b).

For the rest of the reconstruction algorithm to work, the 3D strut point cloud has to be categorized into rings and beams. Similar to the BVS reconstruction, we first project the 3D strut point cloud to 2D using the projection method. Then, the operator will draw the ring lines and beam lines to interpret the 2D strut point cloud. Then, the points will be categorized into rings and beams according to their distances to the lines drawn by the operator.

The stent reconstruction method is modified to give the correct skeleton for the metallic stent. Previously in BVS stent reconstruction, the ring strut points are sorted according to the angular coordinate $r$, and the beam struts point to the vertical coordinates $z$. The metallic stent has a more complicated

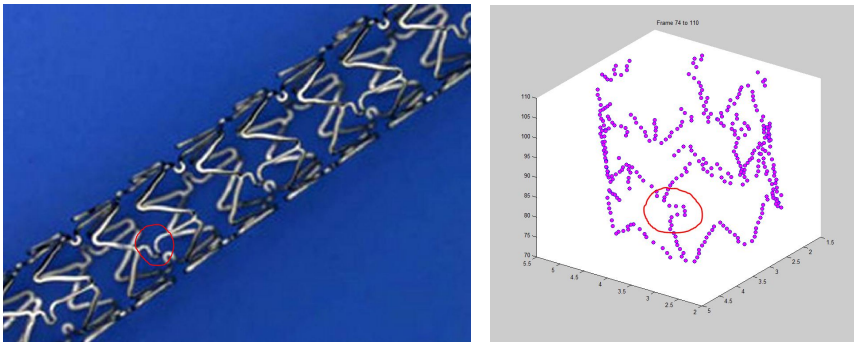

(a) (b)

Figure 8.4: (a) Abbott XIENCE drug-eluting metallic stent; a beam with a wiggle is circled. (b) 3D point cloud of of Abbott XIENCE, the points on a beam is circled.

ring and beam structure, so a more robust sorting method has be created to produce correct stent skeleton. Instead of using $r$ and $z$ coordinates, we sort the strut points based on their relative order on the ring and beam lines created by the drawer. To illustrate the difference in sorting, we take a particular set of beams points as an example:

Figure 8.5a shows a set of beam points in 2D, which has been separated out from the rest of the 2D point cloud. If we sort the set of points by their $z$ coordinates, similar to the way we sort beam points for BVS, we would obtain an incorrect order (see Figure 8.5b) that does not agree with the design of the stent. A solution for this problem is to use the beam drawing from the operator (Figure 8.5c). This thick beam line was created to categorize the points it covers as the points of the corresponding beam. We can extract a cubic spline $S_{draw}$ from the hand-drawn line with the help of software such as Plot Digitizer (`http://plotdigitizer.sourceforge.net/`) or Engauge Digitizer (`http://digitizer.sourceforge.net/`). This spline $S_{draw}$, shown in Figure 8.5d, is in 2D space and is not the 3D spline for the stent wire-frame (the 3D spline construction for the stent wire-frame was described in Section 6.2). We only use $S_{draw}$ to sort the beam points. The strut points should be close to the spline $S_{draw}$. For each strut point $P_i$ on this beam or another ring and beam, we find its nearest point $P_{S_i}$ from the spline curve and record the corresponding parameter $t_i$ of $P_{S_i}$. Then the strut points $P_i$ are sorted by $t_i$, resulting in an order that reflects the actual

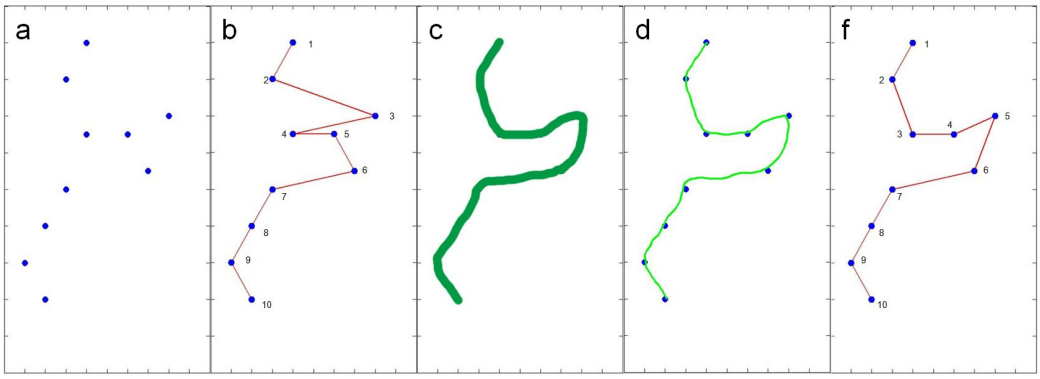


Figure 8.5: (a) A set of beam points. (b) Incorrect sorting by $Z$ coordiantes. (c) The beam line drawing from operator. (d) 2D spline extracted from the the beam line drawing. (e) Beam points are sorted correctly using the spline.

design of the Abbott XIENCE stent (see Figure 8.5e).

The stent volume is then added to the wire-frame in the same fashion as the BVS reconstruction. We only need to change the dimension of the cross-section profile to the metallic strut dimension, which is 81 $\mu m$ by 81 $\mu m$. The reconstructed stent geometry is presented in Figure 8.6. The XIENCE struts appear to be significantly thinner than the BVS stent.

This is the first time that patient-specific metallic stent was reconstructed from OCT images. Previous simulations of metallic stents only utilize the original stent design or virtual stent deployment. The stent geometry provides us much information about stent disposition in the vessel. Shall we use the metallic stent geometry to conduct its CFD simulations? The answer is maybe, leaning more toward to a no. Thanks to technological advancement, current metallic stents such as the Abbott XIENCE, have a very thin strut. Therefore, it is unnecessary to perform CFD simulations, since the extreme thin stent has small impact on the fluid dynamics of the blood flow. However, the patient-specific metallic stent geometries have huge potentials. They could be used for structural simulation and drug assimilation simulation, both highly anticipated to help study metallic stents.

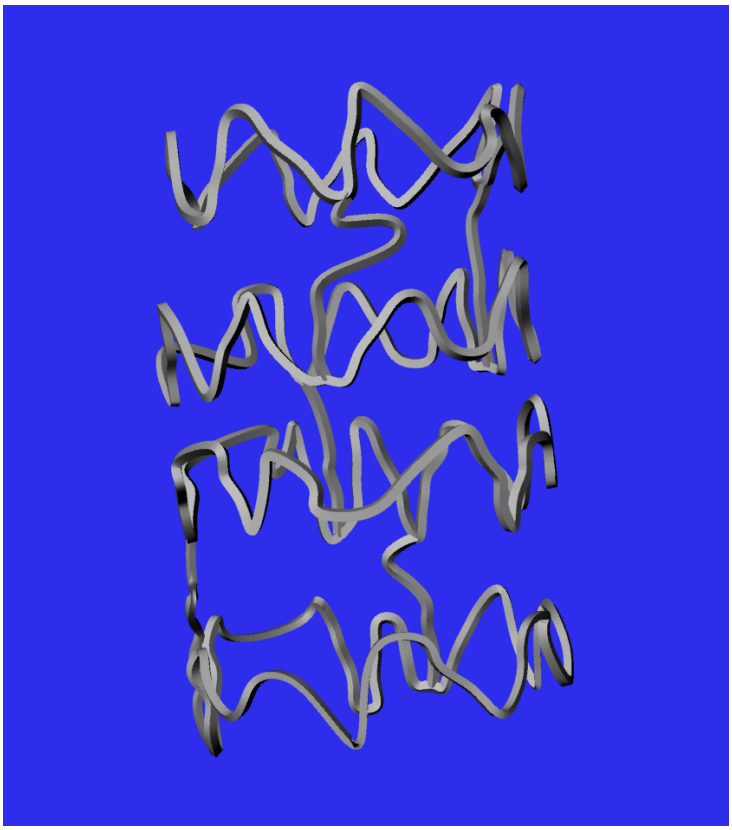

Figure 8.6: Reconstructed Abbott XIENCE metallic stent.

# Chapter 9

# Conclusion and limitations

## 9.1 Conclusion

In this thesis, we have demonstrated that patient-specific reconstructions of vascular stents are possible. With a reconstructed patient-specific stent, we can obtain the geometry of the stented vessel of the living patient and use the geometry as the domain for CFD simulations. We have also shown that the curvature of the stented vessel can be extracted from angiographic images and then applied to the stented vessel geometry in order to bring the simulations even closer to reality. Such highly patient-specific CFD simulations are helpful to study the hemodynamic of stented coronary arteries. Both velocity streamlines and WSS can be visualized down to the strut level. The geometry reconstruction and simulations have been applied to the ABSORB BVS made by Abbott, a leading company in BVS. Simulation results show that the thick BVS struts cause high WSS on the struts' endoluminal surfaces and low WSS between struts. Recirculation behind the BVS has been speculated, and our simulations validate their existence. Such recirculation, along with WSS fluctuations, could possibly expedite thrombosis, which can lead to devastating restenosis.

The reconstruction and simulation method is a series of programs linked together. When made automatic, the method enables us to perform a larger quantity of patient-specific simulations, which could lead to statistically stronger clinical conclusions. With modification, the reconstruction algorithm can also produce a patient-specific metallic stent.

The negative factors we have thus found in the simulation results shall

not blemish the value of BVS, but rather help with its further development into a mature medical device that ultimately saves more lives from coronary heart disease. We hope that our efforts and struggles can one day improve stenting technology and help save more lives from coronary heart disease.

## 9.2 Limitations

There are three limitations in the reconstruction process. The first limitation is the interpretation of the 2D point cloud described in Section 5.2. An operator has to draw the ring and beam lines to interpret the stent pattern that she or he perceives from the 2D point cloud. If the light source moves too much in the lumen during the OCT pullback run, the resulting 2D point cloud could be difficult to interpret. Then the drawing process becomes rather subjective to the operator, and often re-draws are required if the wire-frame reconstructed from the drawing is unacceptable. The second limitation lies in the application of curvature to the stent and lumen described in Section 6.2: The OCT slices are placed perpendicular to the catheter spline. A pair of landmarks are created to ensure that the first OCT slice falls onto the correct location on the catheter, and thereafter the remaining OCT slices follow the initial OCT slice to their correct locations. The planter orientation of the initial OCT slice is randomly chosen. This means that even though the rest of the OCT slices have a consistent planter orientation on the catheter, this orientation is determined solely by the randomly chosen orientation of the initial OCT slice and is not patient-specific. The third limitation is the geometry repair process: to be used as the CFD domain, the reconstructed geometry of the stented lumen has to undergo a series of repair steps. As described in Section 6.4, certain steps in the repair process have to be performed manually. Extensive manual interaction such as manual repair, however, does not support our vision of creating a highly automated reconstruction process. The problems in the STL arise mostly during the subtraction of the stent from the lumen. In the next chapter, we introduce a possible solution to reduce the time spent on geometry repair: we could skip the subtraction of stent entirely, and instead use the stent as part of the CFD domain with extremely high viscosity. When the above three limitations are lifted, the reconstruction and simulation process will become much more efficient and accurate.

# Chapter 10

# Future directions

## 10.1 Finding the ultimately missed struts

The Automatic BVS strut detection program detect struts from OCT images at above 80% accuracy. The accuracy can be significantly improved if incomplete strut edges can be detected.

The detection program is equipped with a feature that allows users to patch the results manually by adding the missed strut points on the 2D strut point cloud. After each automatic detection of each OCT frame, the program presents the detected coordinates of strut points with the OCT in the background for user verification. If there is any missed strut, the user can easily add the missed strut to the final detection by simply moving the cursor to the missed strut and clicking the center of it. A local image of the missed strut is also saved. Each OCT put back run can provide 10 to 20 such images of missed struts, a few of which are shown in Figure 4.7. The observation indicates that a major reason for a strut to be missed is its incomplete edge since 75% of missed struts have incomplete edges. This is largely due to the catheter shadow, which unfortunately is inevitable.

The current detection algorithm searches for a small closed region formed by connected pixels. The incomplete strut edge will leave an open region that cannot to recognized. However, over time, a large data bank of missed strut images will have been saved for us to conduct future analyses. The rate of accuracy could be improved up to 95% if we can created a method to detect incomplete edges.

## 10.2 Saved 2D stent pattern

The only step expected to be manually performed in the reconstruction process is the drawing of a 2D pattern. Therefore, the overall time of the reconstruction and simulation shall be largely reduced if this step becomes easier to perform or is completely eliminated.

After the point cloud is projected from 3D to 2D space, it usually presents a clear pattern. The user interprets the pattern by drawing separate lines to cover each ring and beam on the 2D point cloud. Each 3D point cloud is opened in 3 sessions, providing three interpretive drawings like the one shown in Figure 6. As more cases are processed, a large pool of such drawings will be saved. Those drawings are like "fingerprints" of a stent: all of the drawings share similar features, yet each of them is unique.

The 3D point cloud is now opened to 2D by the projection method described in section 4.3. The 2D point cloud can present a better pattern if the 3D point cloud is opened along the vessel centerline or the catheter path. It is also foreseeable that a machine-learning algorithm can be created to interpret a new 2D point cloud automatically by using the large pool of existing drawings.

## 10.3 Bypass the geometry repair

The CFD domain is obtained by subtracting the stent STL geometry from the lumen STL geometry. This operation causes several types of errors in the CFD domain. The CFD domain has to undergo a series of repair steps in order that it can be discretized into tetrahedron elements from the simulations. The repair procedure is described in Section 6.4. This process can be tedious and is a "bottleneck" in our reconstruction/simulation procedure. Here, we provide a method that could possibly help us bypass the geometry repair: we mesh the lumen without the subtraction of the stent but prescribe very high viscosity, of at least 40 $g/(cm \cdot s)$ (1000 times that of the viscosity of water), to the region occupied by the stent. Therefore, even though the stent region is included in the CFD, its high viscosity causes it to act like a solid structure. One challenge in this approach is using the stent geometry to accurately classify the correct elements of the lumen as elements of the stent.

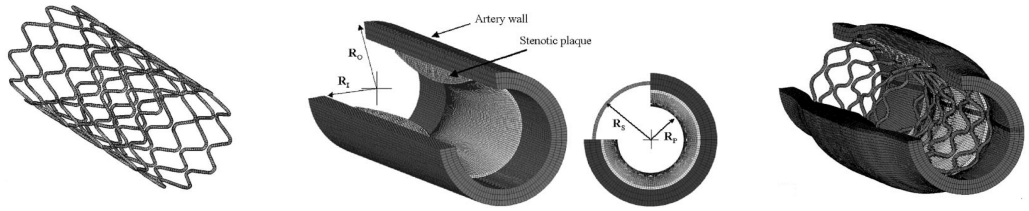


(a) (b) (c)

Figure 10.1: (a) Finite-element meshes of the fully expanded stent design. (b) Arbitrary atherosclerotic coronary vessel geometry; artery outer radius, $R_0 = 2\ mm$, normal lumen inner radius, $R_I = 1.5\ mm$, lumen radius with plaque, $R_P = 1\,mm$, stent radius, $RS = 1.75\,mm$. (c) Simulated deformation of the artery, plaque and stent [12].

## 10.4 Stress simulation with the existing geometry

Before this work, stent stress simulation could only be performed using the stent design from stent makers. All three components of the geometry (stent, lumen, and plaque) are idealized. We take the work of C. Lally et al. as an example: to estimate the amount of stress the stent exerts on the vessel wall, both the lumen and plaque have to be created arbitrarily [12]. The stent geometry is the original stent design, which does not reflect deformation after deployment (see Figure 10.1). With our reconstruction method, we can obtain patient-specific stent and lumen geometry. The older imaging technology IVUS, with its ability to penetrate vessel tissues, allows tomographic assessment of the lumen area, plaque size, distribution, and composition. If the IVUS image of the same image is also available, patient-specific plaque geometry can also be created. Therefore, it is possible to simulate the stent stress on the vessel wall using entirely patient-specific geometry. Such simulation requires OCT, IVUS and angiography images from the same patient, taken at the end of stenting procedure. The coordination of three different imaging segmentations and the matching of the curvature and the geometries of the three components could be challenging. We believe with effort, this task could be accomplished in the near future.

## 10.5 More automatic, efficient, accurate reconstruction and simulation pipeline

In the last two and half years, a complete procedure has been successfully developed starting from stent detection in OCT to curvature extraction from angiography, to discretization of the geometry, and finally, to CFD, visualization and post-processing. This is a large collaboration among a group of capable researchers with a diverse set of skills.

This reconstruction and simulation procedure delivers results that give valuable patient-specific information regarding the blood flow, especially the intricate details surrounding the stent struts. However, our goal is to undertake hundreds of patients in a period of one to two years, since a large number of patient-specific cases can create statistically meaningful conclusions.

A large number of patients requires a more efficient pipeline. The major components in the current procedure include strut detection, stent wire-frame reconstruction, stent volume reconstruction, lumen reconstruction, extraction of curvature, geometry preparation, meshing, and CFD, and they are thoroughly discussed in this thesis. The components are written in different programming languages and they work separately, one after another. Their connection should be smooth. Our objective is to integrate all steps into one comprehensive software, which takes medical imaging data and produces geometry and simulation results without much human interaction. Such software will also produce structural simulation, since the materials - stent and lumen geometry - are already created during the process. Not only should the procedure yield reliable results, it also has to be highly automatic and reasonably efficient.

# Bibliography


[1] Yang, B., Gogas, B., Esposito, G., Hung, O., Arzrumly, E. R., Piccinelli, M., King, S., Giddens, D., Veneziani, A., and Samady, H., 2015. "Novel in-human four dimensional wall shear stress calculation of a coronary bioresorbable scaffold using optical coherence tomography images and blood flow simulations". *Journal of the American College of Cardiology,* **65**(10_S).

[2] What is coronary heart disease by national heart, lung, and blood institute. `http://www.nhlbi.nih.gov/health/health-topics/topics/cad`. Accessed: May 2015.

[3] Gogas, B. D., McDaniel, M., Samady, H., and King, S. B., 2014. "Novel drug-eluting stents for coronary revascularization". *Trends in cardiovascular medicine,* **24**(7), pp. 305–313.

[4] Gogas, B. D., 2014. "Bioresorbable scaffolds for percutaneous coronary interventions". *Global cardiology science & practice,* **2014**(4), p. 409.

[5] Bourantas, C., Fotiadis, D. I., Kourtis, I., Michalis, L. K., and Plissiti, M., 2003. "Three-dimensional coronary artery reconstruction using fusion of intravascular ultrasound and biplane angiography". In International Congress Series, Vol. 1256, Elsevier, pp. 1133–1138.

[6] Sanmartín, M., Goicolea, J., García, C., García, J., Crespo, A., Rodríguez, J., and Goicolea, J. M., 2006. "Influence of shear stress on in-stent restenosis: in vivo study using 3d reconstruction and computational fluid dynamics". *Revista Española de Cardiología (English Edition),* **59**(1), pp. 20–27.

[7] Jiménez, J. M., and Davies, P. F., 2009. "Hemodynamically driven stent strut design". *Annals of biomedical engineering,* **37**(8), pp. 1483–1494.

[8] Papafaklis, M. I., Bourantas, C. V., Farooq, V., Diletti, R., Muramatsu, T., Zhang, Y., Fotiadis, D. I., Onuma, Y., Garcia, H. M. G., Michalis, L. K., et al., 2013. "In vivo assessment of the three-dimensional haemodynamic micro-environment following drug-eluting bioresorbable vascular scaffold implantation in a human coronary artery: fusion of frequency domain optical coherence tomography and angiography". *EuroIntervention: journal of EuroPCR in collaboration with the Working Group on Interventional Cardiology of the European Society of Cardiology,* **9**(7), pp. 890–890.

[9] Bourantas, C. V., Papafaklis, M. I., Kotsia, A., Farooq, V., Muramatsu, T., Gomez-Lara, J., Zhang, Y.-J., Iqbal, J., Kalatzis, F. G., Naka, K. K., et al., 2014. "Effect of the endothelial shear stress patterns on neointimal proliferation following drug-eluting bioresorbable vascular scaffold implantation: an optical coherence tomography study". *JACC: Cardiovascular Interventions,* **7**(3), pp. 315–324.

[10] Ellwein, L. M., Otake, H., Gundert, T. J., Koo, B.-K., Shinke, T., Honda, Y., Shite, J., and LaDisa Jr, J. F., 2011. "Optical coherence tomography for patient-specific 3d artery reconstruction and evaluation of wall shear stress in a left circumflex coronary artery". *Cardiovascular Engineering and Technology,* **2**(3), pp. 212–227.

[11] Gogas, B. D., King, S. B., Timmins, L. H., Passerini, T., Piccinelli, M., Veneziani, A., Kim, S., Molony, D. S., Giddens, D. P., Serruys, P. W., et al., 2013. "Biomechanical assessment of fully bioresorbable devices". *JACC: Cardiovascular Interventions,* **6**(7), pp. 760–761.

[12] Lally, C., Dolan, F., and Prendergast, P., 2005. "Cardiovascular stent design and vessel stresses: a finite element analysis". *Journal of biomechanics,* **38**(8), pp. 1574–1581.

[13] Heart disease facts.

[14] Khaw, K.-T., 1997. "Epidemiology of coronary heart disease". *Women and heart disease*, p. 7.

[15] Cardiovascular diseases. `http://www.who.int/mediacentre/factsheets/fs317/en/`. Accessed: May 2015.

[16] State and county quickfacts, atlanta (city), georgia (state). `http://quickfacts.census.gov/qfd/states/13/1304000.html`. Accessed: July 2015.

[17] Enos, W. F., Holmes, R. H., and Beyer, J., 1953. "Coronary disease among united states soldiers killed in action in korea: preliminary report". *Journal of the American Medical Association,* **152**(12), pp. 1090–1093.

[18] McNamara, J. J., Molot, M. A., Stremple, J. F., and Cutting, R. T., 1971. "Coronary artery disease in combat casualties in vietnam". *Jama,* **216**(7), pp. 1185–1187.

[19] Levy, D., 2012. "Combating the epidemic of heart disease". *Jama,* **308**(24), pp. 2624–2625.

[20] Serruys, P. W., de Jaegere, P., Kiemeneij, F., Macaya, C., Rutsch, W., Heyndrickx, G., Emanuelsson, H., Marco, J., Legrand, V., Materne, P., et al., 1994. "A comparison of balloon-expandable-stent implantation with balloon angioplasty in patients with coronary artery disease". *New England Journal of Medicine,* **331**(8), pp. 489–495.

[21] Farooq, V., Gogas, B. D., and Serruys, P. W., 2011. "Restenosis delineating the numerous causes of drug-eluting stent restenosis". *Circulation: Cardiovascular Interventions,* **4**(2), pp. 195–205.

[22] Brugaletta, S., Heo, J. H., Garcia-Garcia, H. M., Farooq, V., van Geuns, R. J., de Bruyne, B., Dudek, D., Smits, P. C., Koolen, J., McClean, D., et al., 2012. "Endothelial-dependent vasomotion in a coronary segment treated by absorb everolimus-eluting bioresorbable vascular scaffold system is related to plaque composition at the time of bioresorption of the polymer: indirect finding of vascular reparative therapy?". *European heart journal,* **33**(11), pp. 1325–1333.

[23] Hahn, C., and Schwartz, M. A., 2009. "Mechanotransduction in vascular physiology and atherogenesis". *Nature reviews Molecular cell biology,* **10**(1), pp. 53–62.

[24] Farooq, V., Serruys, P. W., Heo, J. H., Gogas, B. D., Onuma, Y., Perkins, L. E., Diletti, R., Radu, M. D., Räber, L., Bourantas, C. V.,

et al., 2013. "Intracoronary optical coherence tomography and histology of overlapping everolimus-eluting bioresorbable vascular scaffolds in a porcine coronary artery model: the potential implications for clinical practice". *JACC: Cardiovascular Interventions,* **6**(5), pp. 523–532.

[25] Bezerra, H. G., Costa, M. A., Guagliumi, G., Rollins, A. M., and Simon, D. I., 2009. "Intracoronary optical coherence tomography: a comprehensive review: clinical and research applications". *JACC: Cardiovascular Interventions,* **2**(11), pp. 1035–1046.

[26] Bezerra, H. G., Attizzani, G. F., Sirbu, V., Musumeci, G., Lortkipanidze, N., Fujino, Y., Wang, W., Nakamura, S., Erglis, A., Guagliumi, G., et al., 2013. "Optical coherence tomography versus intravascular ultrasound to evaluate coronary artery disease and percutaneous coronary intervention". *JACC: Cardiovascular Interventions,* **6**(3), pp. 228–236.

[27] Sheehy, A., Gutiérrez-Chico, J. L., Diletti, R., Oberhauser, J. P., Glauser, T., Harrington, J., Kossuth, M. B., Rapoza, R. J., Onuma, Y., Serruys, P. W., et al., 2012. "In vivo characterisation of bioresorbable vascular scaffold strut interfaces using optical coherence tomography with gaussian line spread function analysis". *EuroIntervention,* **7**(10), pp. 1227–1235.

[28] Gonzalo, N., Serruys, P. W., Piazza, N., and Regar, E., 2009. "Optical coherence tomography (oct) in secondary revascularisation: stent and graft assessment". *EuroIntervention,* **5**(Suppl D), pp. D93–D100.

[29] Bourantas, C. V., Kourtis, I. C., Plissiti, M. E., Fotiadis, D. I., Katsouras, C. S., Papafaklis, M. I., and Michalis, L. K., 2005. "A method for 3d reconstruction of coronary arteries using biplane angiography and intravascular ultrasound images". *Computerized Medical Imaging and Graphics,* **29**(8), pp. 597–606.

[30] Saber, E., Murat Tekalp, A., and Bozdagi, G., 1997. "Fusion of color and edge information for improved segmentation and edge linking". *Image and Vision Computing,* **15**(10), pp. 769–780.

[31] Wahle, A., Prause, G. P., DeJong, S. C., and Sonka, M., 1999. "Geometrically correct 3-d reconstruction of intravascular ultrasound images

by fusion with biplane angiography-methods and validation". *Medical Imaging, IEEE Transactions on,* **18**(8), pp. 686–699.

[32] Ku, D. N., Giddens, D. P., Zarins, C. K., and Glagov, S., 1985. "Pulsatile flow and atherosclerosis in the human carotid bifurcation. positive correlation between plaque location and low oscillating shear stress.". *Arteriosclerosis, thrombosis, and vascular biology,* **5**(3), pp. 293–302.

[33] Morlacchi, S., and Migliavacca, F., 2013. "Modeling stented coronary arteries: where we are, where to go". *Annals of biomedical engineering,* **41**(7), pp. 1428–1444.

[34] McDaniel, M. C., and Samady, H., 2011. "The sheer stress of straightening the curves: Biomechanics of bioabsorbable stents". *JACC: Cardiovascular Interventions,* **4**(7), pp. 800–802.

[35] Tu, S., Holm, N. R., Koning, G., Huang, Z., and Reiber, J. H., 2011. "Fusion of 3d qca and ivus/oct". *The international journal of cardiovascular imaging,* **27**(2), pp. 197–207.

[36] Koskinas, K. C., Chatzizisis, Y. S., Antoniadis, A. P., and Giannoglou, G. D., 2012. "Role of endothelial shear stress in stent restenosis and thrombosis: pathophysiologic mechanisms and implications for clinical translation". *Journal of the American College of Cardiology,* **59**(15), pp. 1337–1349.

[37] Formaggia, L., Quarteroni, A., and Veneziani, A., 2010. *Cardiovascular Mathematics: Modeling and simulation of the circulatory system*, Vol. 1. Springer Science & Business Media.

[38] Wang, A., Nakatani, S., Eggermont, J., Onuma, Y., Garcia-Garcia, H. M., Serruys, P. W., Reiber, J. H., and Dijkstra, J., 2014. "Automatic detection of bioresorbable vascular scaffold struts in intravascular optical coherence tomography pullback runs". *Biomedical optics express,* **5**(10), pp. 3589–3602.

[39] Xu, C., Schmitt, J. M., Akasaka, T., Kubo, T., and Huang, K., 2011. "Automatic detection of stent struts with thick neointimal growth in intravascular optical coherence tomography image sequences". *Physics in medicine and biology,* **56**(20), p. 6665.

[40] Mathworks documentation imerode. `http://www.mathworks.com/help/images/ref/imerode.html`. Accessed: March 2015.

[41] Mathworks documentation rgb2gray. `http://www.mathworks.com/help/matlab/ref/rgb2gray.html`. Accessed: March 2015.

[42] Mathworks documentation gamma correction. `http://www.mathworks.com/help/vision/ref/gammacorrection.html`. Accessed: March 2015.

[43] Otsu, N., 1975. "A threshold selection method from gray-level histograms". *Automatica,* **11**(285-296), pp. 23–27.

[44] Mathworks documentation linkage. `http://www.mathworks.com/help/stats/linkage.html`. Accessed: March 2015.

[45] Lee, E. T., 1989. "Choosing nodes in parametric curve interpolation". *Computer-Aided Design,* **21**(6), pp. 363–370.

[46] Athanasiou, L. S., Bourantas, C. V., Rigas, G., Sakellarios, A. I., Exarchos, T. P., Siogkas, P. K., Ricciardi, A., Naka, K. K., Papafaklis, M. I., Michalis, L. K., et al., 2014. "Methodology for fully automated segmentation and plaque characterization in intracoronary optical coherence tomography images". *Journal of biomedical optics,* **19**(2), pp. 026009–026009.

[47] Moraes, M. C., Cardenas, D. A. C., Furuie, S. S., et al., 2013. "Automatic lumen segmentation in ivoct images using binary morphological reconstruction". *Biomedical engineering online,* **12**(78), pp. 1–17.

[48] Slager, C. J., Wentzel, J. J., Schuurbiers, J. C., Oomen, J. A., Kloet, J., Krams, R., Von Birgelen, C., Van Der Giessen, W. J., Serruys, P. W., and De Feyter, P. J., 2000. "True 3-dimensional reconstruction of coronary arteries in patients by fusion of angiography and ivus (angus) and its quantitative validation". *Circulation,* **102**(5), pp. 511–516.

[49] Arnold, D. N., Brezzi, F., and Fortin, M., 1984. "A stable finite element for the stokes equations". *Calcolo,* **21**(4), pp. 337–344.

[50] Diamond, S., Eskin, S., and McIntire, L., 1989. "Fluid flow stimulates tissue plasminogen activator secretion by cultured human endothelial cells". *Science,* **243**(4897), p. 1483.

[51] Krams, R., Wentzel, J., Oomen, J., Vinke, R., Schuurbiers, J., De Feyter, P., Serruys, P., and Slager, C., 1997. "Evaluation of endothelial shear stress and 3d geometry as factors determining the development of atherosclerosis and remodeling in human coronary arteries in vivo combining 3d reconstruction from angiography and ivus (angus) with computational fluid dynamics". *Arteriosclerosis, thrombosis, and vascular biology,* **17**(10), pp. 2061–2065.

[52] Wang, A., Eggermont, J., Dekker, N., Garcia-Garcia, H. M., Pawar, R., Reiber, J. H., and Dijkstra, J., 2013. "Automatic stent strut detection in intravascular optical coherence tomographic pullback runs". *The international journal of cardiovascular imaging,* **29**(1), pp. 29–38.